Democratic and Popular Republic of Algeria

Ministry of Higher Education and Scientific Research

University Mohamed Khider of Biskra

Faculty of Exact Sciences and Science of Nature and Life

Department of Material Sciences

Thesis

Presented to obtain the degree of

Doctorate

Option: Physics of Thin Films.

Entitled:

Synthesis of SnO_2 semiconductor nanostructures doped with alkaline earth elements: Structural and optical study for photo-catalytic application

Presented by:

Ms. SAOULA Imene

Publicly defended on: / / 2024

In front of the Jury committee composed of:

M^{r}. A. CHALA	Professor	University of Khenchela	President
M^{me}. C. SIAD	Professor	University of Biskra	Supervisor
M^{r}. A. OUAHAB	Professor	University of Biskra	Co- Supervisor
M^{me}. L. AISSANI	Professor	University of Khenchela	Examiner
M^{r}. S. RAHMANE	Professor	University of Biskra	Examiner

Academic year 2024-2025

Acknowledgment

In the name of Allah, the most glorious and merciful, who granted me the strength to work diligently and the confidence to complete this work.

*I am delighted to express my heartfelt gratitude to my supervisor, Professor **Siad Chahinez** and Thesis co-director **Ouahab Abdelouahab** for their endurance, patience and encouragement. It has been a privilege to have their support and help. I hope the result will be as they wish and want.*

*I would like to thank all my teachers, for their support. Many thanks especially for **Mr. Chala Abdelouahad**, Head of Khenchela University- Algeria **Mr. Saâd Rahmane**, professor at Biskra University- Algeria, **Mr. Nouari Saheb**, professor at King Fahd University of Petroleum and Minerals - Kingdom of Saudi Arabia, **Mr. Mohamed Bououdina**, professor at Prince Sultan University- Kingdom of Saudi Arabia, **Ms. Zahia Bencharef**, MCB at Biskra University- Algeria **Ms. Aicha Khater**, MCA at Biskra University- Algeria, and **Nassiba Allag**, doctor at El Oued University- Algeria.*

*I also extend my thanks to my best friend and colleague **Zineb Amraoui**, my colleagues **Nourelhouda Bounedjar**, and **Nourelhouda Mokrani** for their friendship which has been a source of inspiration throughout the course of my thesis.*

Dedication

I dedicate this modest work to:
My mother and father for their affections and loves,
My dear sisters and brothers,
All my teachers and friends,
All those who I love from near and far.

Imene Saoula

Table of Contents

Chapter I: Bibliographic study of SnO_2 and their applications

Chapter II: Elaboration and characterisation of SnO_2 thin films

Chapter III: Experimental and comparison study of pure and doped SnO_2 thin films

Chapter IV: DFT and comparison study of pure and doped SnO_2 thin films

Chapter V: Methylene blue dye photodegradation using pure and doped SnO_2 thin films

General introduction

General introduction

Transparent conductive oxides (TCOs) present a specific group of materials that have unique physical properties compared to other materials, they can combine many properties at the same time, such as; a high electrical conductivity and optical transparency in the visible range, mobility, bandgap, and a low refractive index [1], among the most important TCOs are ZnO [2], TiO_2 [3], Sb_2O_3 [4], In_2O_3 [5], and SnO_2 [6,7]. Tin dioxide in general is an n-type semiconductor [8] and has many specific properties that can distinguish it compared to the other TCOs, from them: high electrical conductivity, transparency in the visible region, reflectivity in the infra-red region, and wide band gap (ranges between 3.5 and 3.8 eV) [9,10], made it the most uses it in many applications, some of them: gas sensors [11], solar cells [12], transparent electrodes [13], photocatalytic application…..etc.

Several effects can be applied on pure tin dioxide to improve its physical properties more and more, among them: effect of doping, and from the dopants that are used: Co, Al, Gd, Ti, Ca, Sr, and Ba [14-19], in this work the last three elements will be used as a dopant which are part of alkaline earth family.

SnO_2 thin films can deposited using numerous techniques include: chemical vapor deposition (CVD) [20], sol gel spin coating [21] sol gel dip coating [22], pulsed laser deposition (PLD) [23], and spray pyrolysis (SPT) [24, 25]. Among the different deposition processes that we mentioned, spray pyrolysis is the most suitable one for preparing tin dioxide thin films, because of its simplicity and low cost [26-30], homogeneity of the deposited films, and deposition in oxygen-rich air instead of vacuum, which is more suitable for the preparation of thin film oxides, it also has the advantage of good control for the doping rate.

The aim of this work is to prepare pure and Ca, Sr, and Ba-doped SnO_2 thin films at varying concentrations starting from 2 wt % and ending at 8 wt % with step equal 2 and also to see the effect of high ionic radii of them (r (Ca^{2+}) = 1.12 °A, r (Sr^{2+}) = 1.32 °A, r (Ba^{2+}) = 1.35 °A) compared to tin ion (r (Sn^{4+}) = 0.71 °A) on the structural, morphological, optical, and electrical properties of SnO_2 films. Then a theorical study by density functional theory (DFT) will be done which is the same experimental study (doping effect), where the Cambridge Serial Total Energy Package (CASTEP) code will be used, and this just for low and high concentration to see how similar theoretical results are to experimental ones.

This thesis is separates into five chapters ordered as follows:

The first chapter consists a bibliography study of transparent conductive oxides (TCOs) and thin films in general, then we specific the review or bibliographic study for the different characteristics and properties of SnO_2, followed by a mention of some applications for which tin dioxide thin film is used, after that we point out some important points related to the photocatalytic application, at the end of this chapter we mention the reason of chosen SnO_2 in this study and the purpose of this work.

The second chapter contains a description of the deposition procedure and its devices which is pneumatic spray pyrolysis technique, also we give details about samples' preparation steps and conditions. Finally, we refer to different characterisation methods which are: X-ray diffractometer (XRD), scanning electron microscopy & energy dispersive X-ray spectroscopy (SEM & EDX), UV- vis spectrophotometer, and four-point probe to determine structural, morphological, optical, and electrical properties respectively.

The third chapter is a comparative between structural properties (texture coefficient, lattice parameters & volume cell, crystallite size microstrain, and dislocation density), surface morphologies, optical properties (transmittance, band gap & Urbach energy values), and electrical properties (sheet resistance and electrical conductivity) of pure and Ca, Sr, and Ba-doped SnO_2 thin films.

In the chapter four we present the main theoretical results obtained after we do an optimization of Cut-off energy and K-points for 1x1x1 SnO_2 cell, where we do a comparative study between high (1x1x2 supercell "8.33 at %") and low (2x2x1 supercell " 4.16 at %") atomic concentration of pure and Ca, Sr, and Ba -doped SnO_2 (we note it M-doped SnO_2), this comparison includes structural properties (lattice parameters and volume cell), band structure and determination of band gap value, and optical properties (absorption coefficient).

The last chapter is about the photocatalytic application, only the samples with low (2 wt%) and high (8 wt%) concentrations will be used for each of the three series prepared to compare its efficiency (degradation rate) with the pure SnO_2.

References:

[1] G. T. Chavan, Y. Kim, M. Q. Khokhar, S. Q. Hussain, E.C. Cho, J. Yi 2, Z. Ahmad, P. Rosaiah, C. W. Jeon, A Brief Review of Transparent Conducting Oxides (TCO): The Influence of Different Deposition Techniques on the Efficiency of Solar Cells, Nanomaterials. 13 (2023), 1226, http:// doi.org/10.3390/nano13071226.

[2] M. Gartner, H. Stroescu, D. Mitrea, M. Nicolescu, Various Applications of ZnO Thin Films Obtained by Chemical Routes in the Last Decade, Molecules. 28 (2023), 4674, https://doi.org/10.3390/molecules28124674.

[3] O. B. khetta, A. Attaf, A. Derbali, H. Saidi, A. Bouhdjer, M. S. Aida, Y. B. khetta, R. Messemeche, R. Nouadji, S. Rahmane, N. E. Djehiche, Precursor concentration effect on the physical properties of transparent titania (Anatase-TiO_2) thin films grown by ultrasonic spray process for optoelectronics application, Optical Materials. 132 (2022), 112790, https://doi.org/10.1016/j.optmat.2022.112790.

[4] A.S. Hassanien, I.M. El Radaf, Effect of fluorine doping on the structural, optical, and electrical properties of spray deposited Sb_2O_3 thin films, Mater. Sci. Semicond. Process. 160 (2023), 107405, https://doi.org/10.1016/j.mssp.2023.107405.

[5] A. Khan, E. Rahman, R. Nongjai, K. Asokan, Role of deposition temperature and Sn content on structural, optical & electrical properties of In_2O_3 thin films, Curr. Appl. Phys. 38 (2022) 49–58, https://doi.org/10.1016/j.cap.2022.03.004.

[6] I. Saoula, C. Siad, A. Ouahab, N. Allag, A. Chala, S. Rahmane, S. Marmi, N. Saheb, Synthesis and properties of alkaline earth elements (Ca, Sr, and Ba) doped SnO_2 thin films, Optical Materials. 145 (2023), 114372, https://doi.org/10.1016/j.optmat.2023.114372.

[7] P. Sivakumar, H.S. Akkera, T.R.K. Reddy, Y. Bitla, V. Ganesh, P.M. Kumar, G. S. Reddy, M. Poloju, Effect of Ti doping on structural, optical and electrical properties of SnO_2 transparent conducting thin films deposited by sol-gel spin coating, Opt. Mater. 113 (2021), 110845, https://doi.org/10.1016/j. optmat.2021.110845.

[8] D. Filatova, M. Rumyantseva, Additives in Nanocrystalline Tin Dioxide: Recent Progress in the Characterization of Materials for Gas Sensor Applications, Materials. 16 (2023), 6733, https://doi.org/10.3390/ma16206733.

[9] E.C. Nwanna, P.E. Imoisili, T.C. Jen, Synthesis and characterization of SnO_2 thin films using metalorganic precursors, J. King Saud Univ. Sci. 34 (2022), 102123,

https://doi.org/10.1016/j.jksus.2022.102123.

[10] A.A. Dakhel, Study of structural, optical and magnetic properties of hydrogenated Ni and (Ga, Zn) co-doped SnO_2 nanocomposites, Mater. Chem. Phys. 252 (2020), 123163, https://doi.org/10.1016/j.matchemphys.2020.123163.

[11] A. Thomas, L. Thirumalaisamy, S. Madanagurusamy, K. Sivaperuman, Incompatibility of Pure SnO_2 Thin Films for Room-Temperature Gas Sensing Application, ACS Omega. 8 (2023), 32848-32854, https://doi.org/10.1021/acsomega.3c04038.

[12] P. Lisnic, L. Hrostea, L. Leontie, M. Girtan, Fluorine-Doped SnO_2 Thin Films in Solar Cell Applications. Morphological, Optical and Electrical Properties, Arch. Metall. Mater. 68 (2023), 483-490, https://doi.org/10.24425/amm.2023.142426.

[13] R. Ramarajan, N. Purushothamreddy, R.K. Dileep, M. Kovendhan, G. Veerappan, K. Thangaraju, D.P. Joseph, Large-area spray deposited Ta-doped SnO_2 thin film electrode for DSSC application, Sol. Energy. 211 (2020), 547–559, https://doi.org/ 10.1016/j.solener.2020.09.042.

[14] M. L. Ayachi, M. Difallah, B. Benhaoua, Nonlinear optical properties of cobalt doped SnO_2 thin films, Optic. 272 (2023), 170296, https://doi.org/10.1016/j.ijleo.2022.170296.

[15] Y.J. Wu, Y.S. Liu, C.I. Hsieh, P.M. Lee, Y.S. Wei, C.H. Liao, C.Y. Liu, Study of p-type AlN-doped SnO_2 thin films and its transparent devices, Applied Surface Science. 328 (2015), 262-268, http://dx.doi.org/doi:10.1016/j.apsusc.2014.12.028.

[16] A. Adjimi, M. S. Aida, N. Attaf, Y. S Ocak, Gadolinium doping effect on SnO_2 thin films optical and electrical properties, Materials Research Express. 22 (2019), 16-20, https://doi.org/10.1088/2053-1591/ab2a8c.

[17] C. F. Liu, C. H. Kuo, T. H. Chen, Y. S. Huang, Optoelectronic Properties of Ti-doped SnO_2 Thin Films Processed under Different Annealing Temperatures, Coatings. 10 (2020), 394, http://doi.org/10.3390/coatings10040394.

[18] S. Asaithambi, P. Sakthivel, M. Karuppaiah, Y. Hayakawa, A. Loganathan, G. Ravi, Improved photocatalytic performance of nanostructured SnO_2 via addition of alkaline earth metals (Ba^{2+}, Ca^{2+} and Mg^{2+}) under visible light irradiation, Appl. Phys. 126 (2020), 1–12, https://doi.org/10.1007/s00339-020-3441-8.

[19] K. Ravikumar, S. Agilan, M. Raja, L. Raja, B. Gokul, R. Ganesh, N. Muthukumarasamy, Design and fabrication of Al/Sr: SnO_2/p-Si Schottky barrier diode based on strontium-doped

SnO_2 thin film, Mater. Res. Express. 6 (2019), 026413, https://doi.org/10.1088/2053-1591/aaed89.

[20] K. Juraic, D. Gracin, M. Culo, Ž. Rapljenovic, J. R. Plaisier, A. Hodzic, Z. Siketic, L. Pavic, M. Bohac, Origin of Mangetotransport Properties in APCVD Deposited Tin Oxide Thin Films, Materials. 13 (2020), 5182, https://doi.org/10.3390/ma13225182.

[21] S. T. Bahade, A. S. Lanje, S. J. Sharma, Synthesis of SnO_2 Thin Film by Sol-gel Spin Coating technique for Optical and Ethanol Gas Sensing Application, Themed Section: Science and Technology. 3 (2017), 567-575, http://doi.org/10.1016/j.physb.2017.09.112.

[22] K. Selma, B. Salima, B. Seddik, R. Djamil, H. Lazhar, Investigation of UV photosensor properties of Al-doped SnO_2 thin films deposited by sol-gel dip-coating method, Journal of Semiconductors. 44 (2023), 032801, https://doi.org/10.1088/1674-4926/44/3/ 032801.

[23] R. Kajal, A. Kandasami, B. Kataria, P. Solanki, D. Mohan, Structural, optical, and dielectric characteristics of pulsed laser deposited SnO_2-TiO_2 composite thin films, Physica Scripta. 98 (2023), 085935, http://doi.org/10.1088/1402-4896/ace569.

[24] B. Maharnavar, A. Pardeshi, M. Patil, P. Pingale, M. Padvi, M. Bagal, Effect of thermal treatment of the SnO_2 thin film prepared by spray pyrolysis method, AIP Conference Proceedings. 2716 (2023), 020002, https://doi.org/10.1063/5.0130929.

[25] N. Katariya, B. Singh, A. Saxena, V. Ganesan, Effect of Carrier Gas on Spray Pyrolysis Deposited SnO_2 Thin Films, Macromolecular Symposia. 407 (2023), 2100473, https://doi.org/10.1002/masy.202100473.

[26] A. Abdelkrim, S. Rahmane, O. Abdelouahab, N. Abdelmalek, G. Brahim, Effect of solution concentration on the structural, optical and electrical properties of SnO_2 thin films prepared by spray pyrolysis, Optik. 127 (2016), 2653–2658, https://doi. org/10.1016/j.ijleo.2015.11.232.

[27] C. Khelifi, A. Attaf, Influence of Ti doping on SnO_2 thin films properties prepared by ultrasonic spray technique, Surface. Interface. 18 (2020), 100449, https://doi. org/10.1016/j.surfin.2020.100449.

[28] R. Mariappan, V. Ponnuswamy, P. Suresh, R. Suresh, M. Ragavendar, C. Cankar, Deposition and characterization of pure and Cd doped SnO_2 thin films by the nebulizer spray pyrolysis (NSP) technique, Mater. Sci. Semicond. Process. 16 (2013), 825–832, https://doi.org/10.1016/j.mssp.2013.01.006.

[29] J. M. Fernandes, G. Suresh, R. Muniramaiah, G. Maharana, A. Geetha, M. Kovendhan, C. Venkateswaran, D.P. Joseph, Effect of anionic bromine doping on the structural, optical and electrical properties of spray-pyrolyzed SnO_2 thin films, Mater. Sci. Eng. B. 282 (2022), 115756, https://doi.org/10.1016/j. mseb.2022.115756.

[30] C. Khelifi, A. Attaf, H. Saidi, A. Yahia, M. Dahnoun, Investigation of F doped SnO_2 thin films properties deposited via ultrasonic spray technique for several applications, Surface. Interface. 15 (2019),244–249, https://doi.org/10.1016/j. surfin.2019.04.001.

Chapter I:

Bibliographic study of SnO_2 and their applications

In this chapter, a bibliographic study on Transparent Conductive Oxides (TCOs) will be presented. Additionally, we will discuss thin films and various methods that can be employed for their deposition. The subsequent sections will delve into a bibliographic exploration of tin dioxide, highlighting its diverse properties, including optical, electrical, and magnetic characteristics. The applications of SnO_2 will also be touched upon. Furthermore, the chapter will provide a concise explanation of the application of photocatalysis, the rationale behind selecting SnO_2, and the overarching purpose of our work in the following paragraphs.

I. 1.Transparent conductive oxide

I. 1.1. Definition

A best transparent conductive oxide is known by its high transparency in the visible region and high electrical conductivity, and this is achieved whenever the conditions of preparing thin film are controlled very well (time of deposition, temperature….) which leads to reducing the structural defects. According to the energy band theory, three electrical states are possible: conductor, insulator, and semiconductor (Figure I.1). In the conductor, the conduction band (CB) and the valence band (VB) overlap, thus allowing the free flow of electrons, the semiconductor has, for its part, a forbidden band that separates VB and CB commonly called gap and noted by optical energy, the electrons cannot take the energies located in this bandaged. They need to acquire energy to move into the CB. For a gap greater than 4 eV, we speak of insulation because even at room temperature, CB is empty [1]. So, the TCOs can be classified as n-type degenerate semiconductors, moreover, In recent years, a few p-doped TCOs have been studied [2-4].

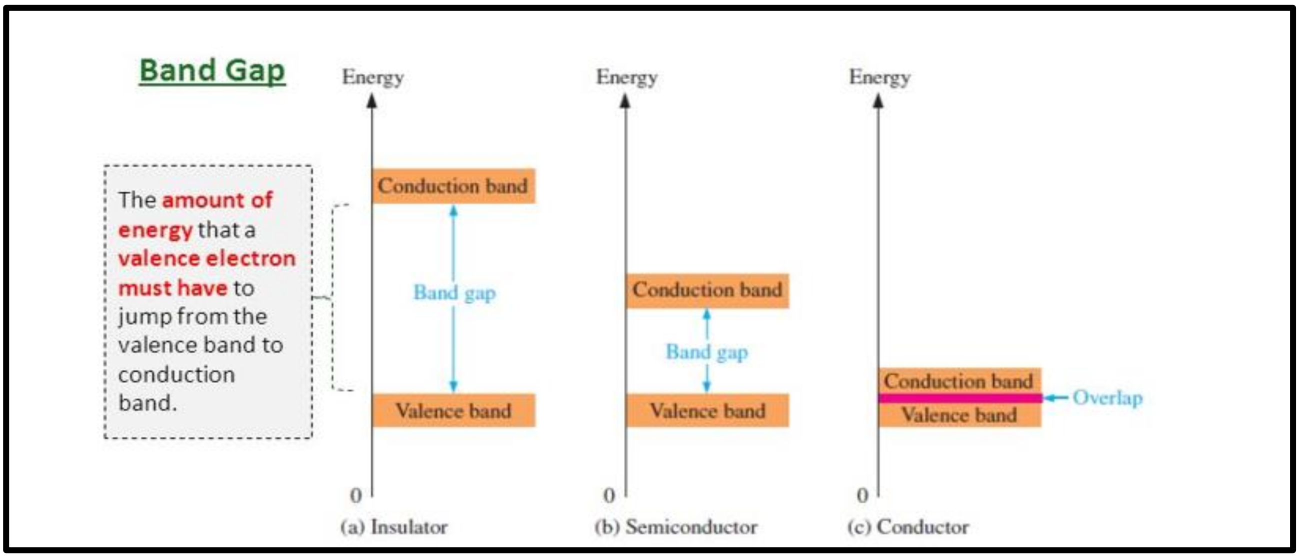

Figure I.1 : Energy diagrams for the three types of materials [1].

There are many factors for choosing the TCO among them the figure of merit Φ or Q which was built by Haacke in 1976, this factor is a correlation between optical properties and electrical properties which is given by the following relationship [1,5] :

$$\Phi = \frac{T^{10}}{R_{sh}} \qquad (I.1)$$

$$Q = \frac{\sigma}{\alpha} = \frac{1}{Rsh\,.\,\ln\,(R+T)} \qquad (I.2)$$

where T (%) is the total transmittance in the visible region, R (%) the total reflectivity, α $(cm)^{-1}$ the absorption coefficient, σ $(\Omega.cm)^{-1}$ the electrical conductivity, and R_{sh} $(\Omega/\square)$ is the sheet resistance. From the most attractive TCOs are : SnO_2 [6], ZnO [7], and TiO_2 [8],….etc.

I. 1-2- Transparent conductive oxides (OTC) properties

- **Electrical properties**

The electrical properties of transparent conductive oxides are very sensitive to oxygen sub-stoichiometry as well as to the nature and concentration of impurities introduced into the material by doping, in most cases, we get n-type TCO if dopants used are generally of higher valence than that of the substituted atoms, which leads to providing free electrons and are considered to be centres donors, so the electrical conductivity increase [9].

- **Optical properties:**

The optical properties of materials are governed by three essential phenomena which are transmission (T), reflection (R), and absorption (A), but for the TCOs the transmission is the most important optical property that determines their quality, is defined as the ratio of the intensity of light transmitted 'I_T' through a material divided to the intensity of light incident on its surface 'I_0':

$$T = I_T/I0 \qquad (I.3) \qquad \text{and} \qquad T\,(\%) = 100.T \qquad (I.4)$$

A typical representation of the transmission spectrum of a TCO is presented in Figure I.2,

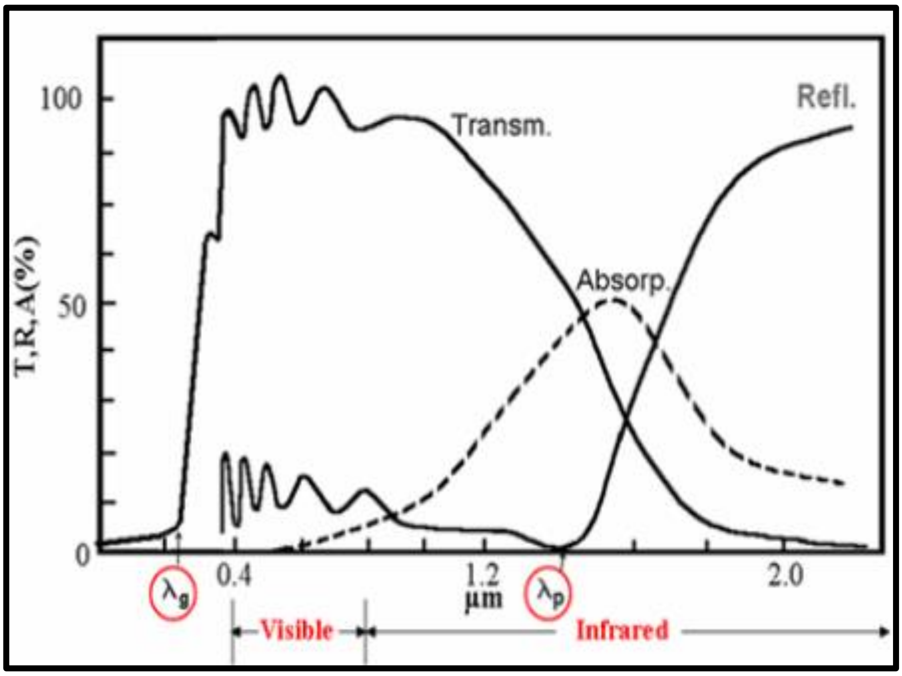

Figure I.2: Transmission, reflection and absorption factors of a conductive transparent oxide [10].

As can be seen in the figure, the transmission of a TCO is limited by two wavelengths (λ_g and λ_p), so we have three cases:

- $\lambda < \lambda_g$: this is the ultraviolet domain of wavelengths, the energy of photons that is greater than or equal to that of the gap is absorbed and the electrons are transferred from the valence band into the conduction band. It is the band-to-band transitions that dominate in this case.
- $\lambda_g < \lambda < \lambda_p$: the conductive oxide is transparent throughout this range which encompasses visible and near-infrared wavelengths. The transparent conductive oxide acts as a conductive anti-reflective layer.
- $\lambda \geq \lambda_p$: in the near-infrared (above 1200 nm), the TCO does not transmit more light. In this interval, TCO exhibits strong absorption.

I. 2.Thin films

I. 2.1. Definition

Thin film of a material is that which has one dimension negligible in front of the other two dimensions which is called by the thickness and we expresses it with Angstrom (°A), it means that their thickness changes according to the application to be used in it without exceeding the angstrom or sometimes nanometres, among these applications we mention: solar cell integrated transparent antenna application [11], flexible thermoelectric application [12], and prospects of metallic delafossites [13]. This small distance between the two boundary surfaces (almost two-dimensional) entails a disturbance of the majority of the physical properties.

Generally, thin films are used to coat a surface (substrate) and improve its physical properties. It is quite obvious that the lower of the thickness, the greater the two-dimensional- effect, on the contrary, when the thickness of the thin film exceeds a certain limit, the thickness effect will becomes not negligible and the material will restore the known properties of solids [14]

I. 2.2. Thin film's preparation methods

The thin films deposition methods can be classified into two sections which are PVD (physical vapor deposition) and CVD (chemical vapor deposition).

The physical methods are the application of a physical action, which is a force of extraction or bombardment of an energetic beam of electrons, photons, or ions which is applied on the target material (substrate surface) with the bombardment energy being greater than the binding energy of the target atoms, deposition of the thin film, is being by the phenomenon of condensation. The chemical methods are chemical reactions between volatile elements near to the substrate surface, which is hot so that its temperature stimulates the chemical reaction and does not exceed its melting temperature, there is also the liquid phase deposition methods. The different thin film deposition techniques are shown in the following schema (Figure I.3).

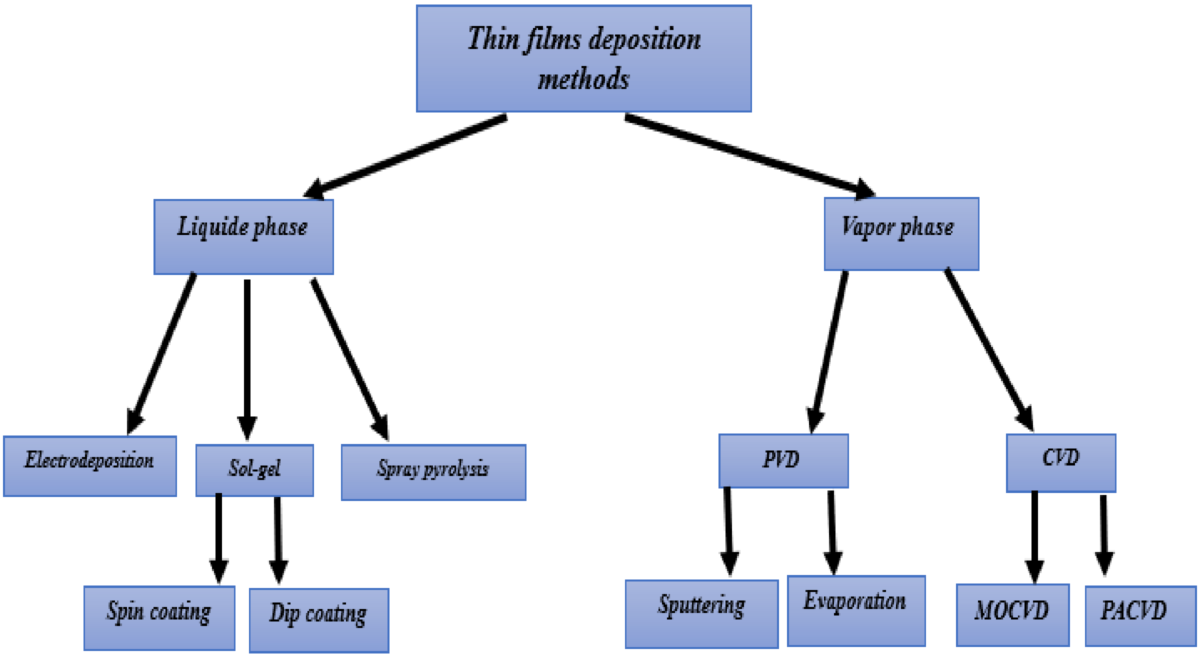

FigureI.3: Classification of different thin film deposition methods.

In the previous schema only the most important methods of deposition were mentioned, but there are several other methods classified in the vapor phase, among them (PVD: **PLD** "**P**ulsed **L**aser **D**eposition", ionic: **IBAD** "**I**on **B**eam **A**ssisted **D**eposition", Each method has advantages and disadvantages. Therefore, the most common method to be frequently used is spray pyrolysis because of its simplicity, reproducible results, the ability to coat on large area substrates, and also it is suitable for the deposition of oxides because it does not need empty (plasma).

I. 3.Tin dioxide (SnO_2)

I. 3. 1. Definition

Transparent conductive oxides are considered thin films and can be used in many applications depending on the oxide used, the most important of which is tin dioxide (SnO_2), as it is in the form of a thin layer that has a high optical transmittance greater than 90% and high electrical conductivity [15], and wide band-gap (3.6 eV) [16], it also has many other advantages, such as economical, chemically stable, innocuous, mechanical stable [17].Table I.1 represents a general physical properties of the SnO_2.

Table I.1: Physical properties of SnO_2 [18].

Property	Value
Molar Mass (g/mol)	150.70
Specific density (g/cm^3)	6.915
Melting point (°C)	1630
Boiling point (°C)	2330

I. 3.2. Crystallin structure

Tin dioxide has a rutile structure (Figure I.4). The unit cell is generally (tetragonal) quadratic (a = b = 0.475 nm and c = 0.318 nm) and contains six atoms: two tin atoms and four oxygen atoms, each tin atom is in the centre of a nearly regular octahedron formed by six oxygen atoms, while each oxygen atom is surrounded by three tin atoms located at the vertices of an isosceles triangle. Oxygen is in position 4f (space group P42 / mmm) given by (u; u; 0), (1-u; 1-u; 0), (1/2 + u; 1/2-u; 1/2) and (1/2-u; 1/2 + u; 1/2) with u = 0.31. Tin is located: (1/2; 1/2; 1/2) and (0; 0; 0). The ionic radii of the Sn^{4+}cation and the O^{2-}anion are respectively 0.71 °A and 1.40 °A [19].

However, SnO_2 has been observed that under fairly high pressures, it can crystallize in an orthorhombic structure [20].

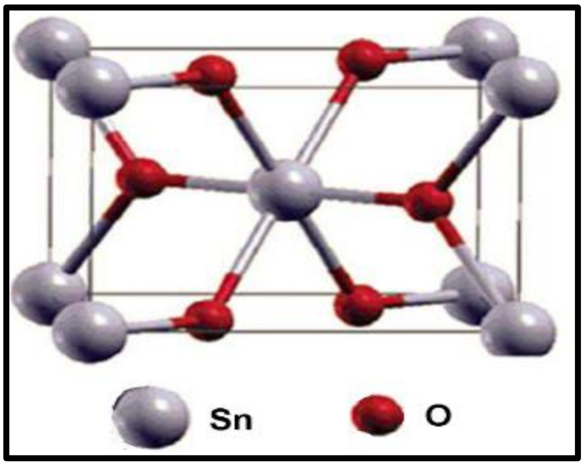

Figure I.4: Unit cell of SnO_2 crystal structure [21].

I. 3.3. Optical properties

Tin dioxide has an important reflection of infrared rays and high absorption in the ultraviolet range however its transmittance is more than 80% in the visible region [22], so the undoped SnO_2 has high transmittance in the visible region because of the few crystal defects, but when it doped with some different elements, free electrons are formed and a transition level energy created in the bandgap so it narrows as representing in Table I.2 . Figure I.5 shows the decrease in the optical transmittance of SnO_2 thin film when it is doped with different concentrations of "Sr", while the undoped has the highest value.

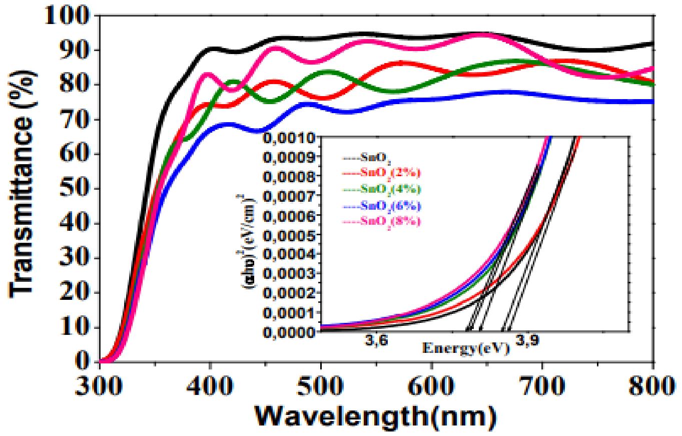

Figure I.5: Optical transmittance spectrum of SnO_2 thin films prepared at different Sr doping concentration [23].

Table I.2: Optical bandgap of thin films of pure and Sr-doped SnO_2 [23].

Samples	SnO_2	SnO_2/2%	SnO_2/4%	SnO_2/6%	SnO_2/8%
Optical band gap (eV)	3.86	3.84	3.80	3.78	3.76

I. 3. 4. Electrical properties

The characteristic electrical properties of SnO_2 are the resistivity of the films, the density of charge carriers, and their mobility. Several techniques can be used to measure the electrical properties such as: four-point method, and Hall effect.

Pure, monocrystalline SnO_2 tin dioxide is a semiconductor material with a large band gap energy ranging from 3.6 to 4.0 eV [24]. This intrinsic semiconductor is practically insulating (stoichiometric SnO_2) but once doped it becomes a relatively good conductor (non-stoichiometric) this case is called intrinsic doping it is the oxygen vacancies that generate electrons in the conduction band.

An oxygen vacancy is formed when an oxygen atom is removed from a normal site. It can be created under the impact of temperature. The oxygen vacancies exist in three different charge states: V_o^0, V_o^+, and V_o^{+2} in the oxide [25], also doping is achieved by introducing atoms from different columns generally III (like In), II (like Zn) [18] or V (like Sb) which has approximately the same ionic radii as the tin ions Sn^{4+}(0.071nm); (0.084 nm for In^{3+} [16],0.088 nm for Zn^{2+} [26], and 0.064 nm for Sb^{5+}[27]), also there are other elements it can be used to dope it like alkaline earth [28].

Shallow donor levels for V_o^+ and V_o^{+2} have been identified at 0.03 and 0.15 eV below the conduction band minimum (CBM), respectively. All these cases are close to the CBM so they will not cause a loss of transparency, but will enhance the conductivity by introducing carrier electrons into the conduction band. This occurs even at room temperature and gives undoped layers fairly low resistivity: $\rho\ (SnO_2) \approx 10^{-2}\ (\Omega.cm)$.

The introduction of valence element from five column "V" dopant results in the addition one free electron in the lattice. The resistivity of this n-type semiconductor thus created decreases when the concentration of carriers (electrons) increases.

It is very interesting to say that the electrical properties of monocrystalline and polycrystalline tin oxide are different (that is mean the conductivity mechanisms are different). The deposited SnO_2 layers have a poly-crystalline structure that has a more complex conduction mechanism.

I. 3.5. Magnetic properties of SnO_2 thin films

Dilute magnetic semiconductors with a high temperature are important in spintronics applications. Several studies have been devoted to studying transparent conducting oxides (TCOs) [29], in contrast , there are few studies about the magnetic properties of doped SnO_2, for example, Ni doped SnO_2 thin films on sapphire substrates grown by PLD [30], magnetic and optical behaviours of SnO_{2-X} thin films with oxygen vacancies prepared by atomic layer deposition [31], another study presents the structural and magnetic properties of Fe/SnO_2/Fe thin films [32], swift heavy ion irradiation induced modifications in structural, microstructural, electrical and magnetic properties of Mn-doped SnO_2 thin films have also been studied [33].

I. 3.6. Different phases of tin oxide

Tin oxide films are amorphous when it deposited at temperatures below 350 °C. It is only at this temperature that the crystallization of these films begins. The thin films of tin oxide produced by the various deposition techniques are generally non-stoichiometric, and they present metastable phases such as SnO and Sn_3O_4. The SnO phase appears at the deposition temperature of 400 °C and disappears at the temperature of 500 °C. This phase decomposes into SnO_2 and Sn at an annealing temperature of 450 °C. This shows that an annealing of the films at 500 °C is necessary to have a good SnO_2 stoichiometry, so the most important tin oxides is SnO and SnO_2 which are formed by oxidation between each other. All these explanations are shown in Figure I.6:

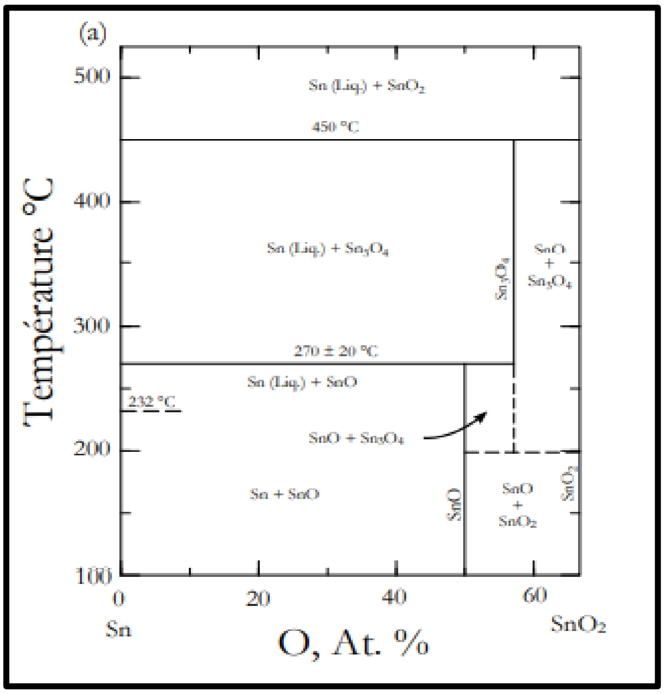

Figure I.6: Sn-O phase diagrams for temperatures up to 500 °C [34].

I. 3.7. Applications of SnO_2 thin films

The special electrical and optical properties of SnO_2 which makes it unique in comparison with other TCOs and its n-type semiconductor character allow for a large number of applications in various types of fields, the most important of which are gas sensors, in the photovoltaic fields, and catalytic applications …... etc. In the following paragraphs, we will mention some applications of tin dioxide:

- **Lithium Batteries**

Lithium is one of the most important elements used in the batteries because of its high energy density and its energy storage capacities, as these batteries contain power-generating compartments called cells, each cell contains a cathode (negative electrode) is made of typically from a chemical compound which is lithium and carbon (graphite)(LiC_6), and an anode (positive electrode) which is made of lithium-cobalt oxide ($LiCoO_2$) or from lithium iron phosphate ($LiFePO_4$) in latest batteries, and a chemical known as electrolyte change according to the type of battery placed between the two electrodes.

To limit the use of carbon because it is harmful to the environment and human health, moreover to increase the energy capacities of batteries, research is focused on combining lithium with numbers of elements such as tin dioxide (SnO_2) in the form of anode [35], these associations can be made in the form of a mixed compound or in form of multilayers.

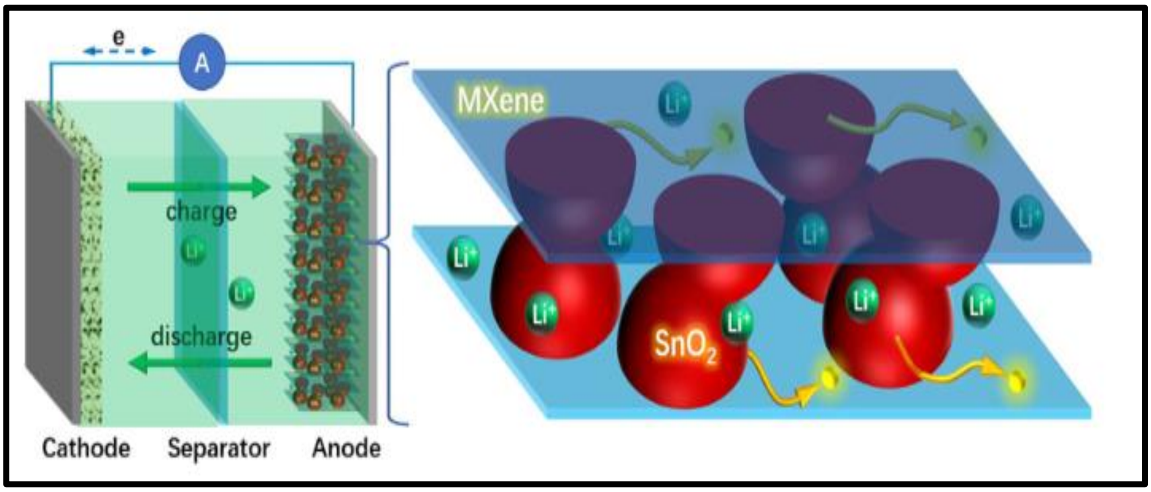

Figure I.7: Lithium battery associated with SnO_2 [35].

- **Solar cells**

The metal oxides are used to separate the electrons and the holes formed under the effect of irradiation in the solar cell, these oxides play the role of a conductor of electrons towards the electrodes. To be able to use in this type of application, the layers must have a very high optical transmission associated with the strongest possible electrical conductivity (here we talked about the function of TCOs in solar cells in general), but when we specify, the most important TCOs used in solar cells are ZnO [36], TiO_2 [37], tin oxide, and fluorine doped tin oxide (FTO) [38]. From the most developed third generation solar cells there are dye-sensitized solar cells (DSSCs) which is one of the photovoltaic applications that use TiO_2 as one of its components, the principle of their work is as follows:

The first step is the absorption of a photon by the sensitizer D, leading to the excited sensitizer D^* which injects an electron into the conduction band of the semiconductor, leaving the sensitizer in the oxidized state D^+. The injected electron flows through the semiconductor network to arrive at the back contact and then through the external load to the counter electrode to reduce the oxidized form (I^-) of the redox mediator which in turn regenerates the sensitizer this completes the circuit, all these steps are summarized in the following four equations [39]:

$$D_{(adsorbed)} + h\upsilon \rightarrow D^*_{(adsorbed)} \quad (1)$$

$$D^*_{(adsorbed)} \rightarrow D^+_{(adsorbed)} + e^-_{(injected)} \quad (2)$$

$$I_3^- + 2e^-_{(cathode)} \rightarrow 3I^-_{(cathode)} \quad (3)$$

$$D^+_{(adsorbed)} + \frac{3}{2}\, I^- \rightarrow D_{(adsorbed)} + \frac{1}{3}\; I_3^- \quad (4)$$

The structure of DSSC is showing in Figure I.8:

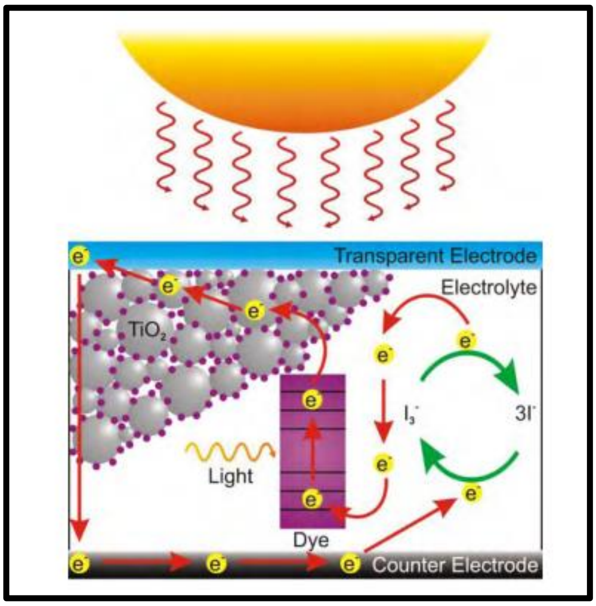

Figure I.8: Structure of a dye-sensitized solar cell (DSSC) [40].

to improve the efficiency of DSSC we can use FTO as an electrode, from the scientific research we observe that the fairly linear increase of the efficiency of the DSSC as a function of the haze factor of FTO as seen in Figure I.9. We observe that the efficiency of the DSSC increased from 8.18% to 10.1% upon increasing the haze factor of the FTO electrode from 2% to 17%. [21].

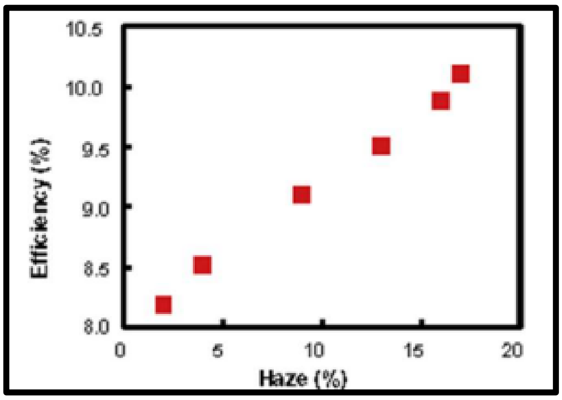

Figure I.9: The conversion efficiency of DSSC fabricated on textured FTO electrodes plotted against the haze factor of the FTO electrode [21].

- **Gas Sensors**

We can call them gas sensors or chemical capture, a chemical sensor is a device that transforms chemical information such as the concentration of a sample to be analyzed into a usable quantity (electrical signal), this gas sensor is composed of two main parts: the first part consists of a sensitive element which allows the recognition of the gas with which it interacts and the second part of a transducer which transforms the interaction between the gas and the sensitive thin film into an electrical signal, several large families of gas sensors are identified according to the type of measurements carried out. We can cite it to: electrochemical sensors, surface acoustic wave sensors, fibre optic sensors, field effect transistor sensors, or semiconductor sensors [41].

The last one which is the semiconductor sensor is the most important type, its working principle is based on the variation in conductivity of a surface semiconductor thin film ("chemo resistive, semiconductor, and sensor") in the presence of gas, for example, for a chemo resistive sensor whose resistance changes in response to changes in the nearby chemical environment, sensitivity can vary from 1 ppb to 5 ppm [42], to be with high quality, it must contain the following conditions:

- ✓ Good target gas sensitivity
- ✓ Little sensitivity to interferents (humidity, non-targeted chemical species, etc.....)
- ✓ Good stability of its properties (over time, depending on the temperature, the chemical species present, etc.....).

Among the most important metal oxides used in semiconductor sensors is tin oxide (SnO_{2-x}, where $0.19 < x < 0.34$) [43], it detects the target gas by the following mechanism shown in Figure I.10.

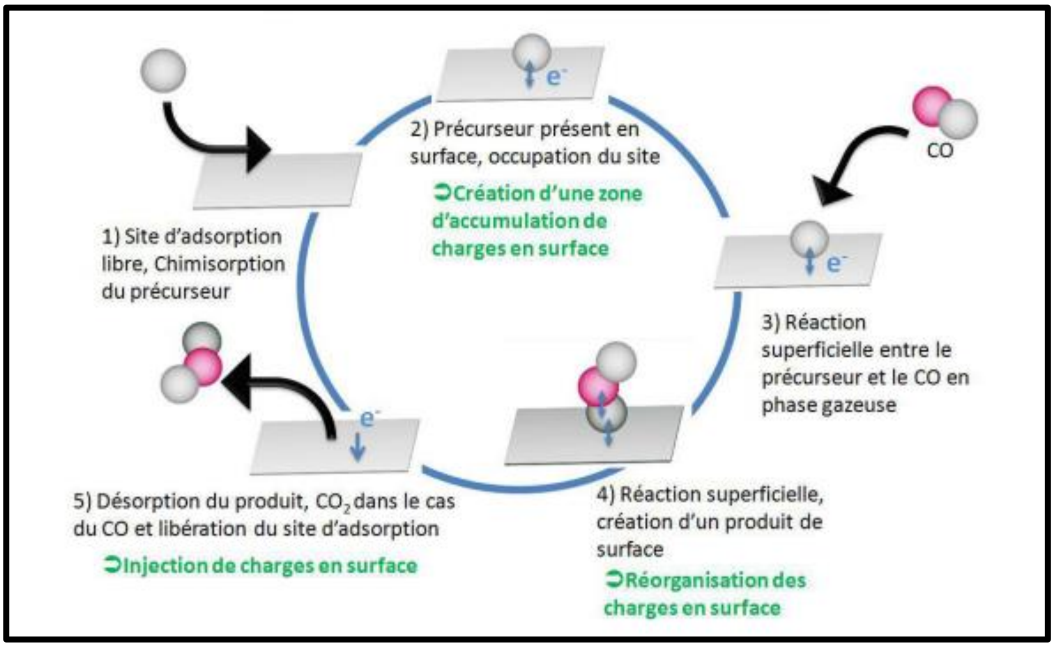

Figure I.10: principle of the reaction of CO with a surface of SnO_2 [43].

When SnO_2 is exposed to gases other than oxygen present in the air, it can make a chemical reaction with the pre-adsorbed oxygen species. The reactions taking place are essentially oxidation-reduction reactions. For example, for a reducing gas like carbon monoxide, the following chemical interaction illustrates this process:

$$\mathrm{CO_{gas}} + \mathrm{O^{-}(surface)} = \mathrm{CO_{2\,gas}} + \mathrm{e^{-}(surface)}$$

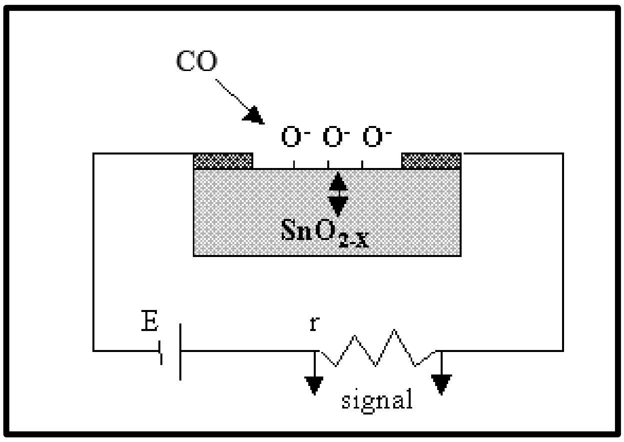

Figure I.11: Example of CO detector based in SnO_2 thin film [44].

- **Electrodes**

Tin oxide can be used as multi-layered composite electrodes of high power $Li_4Ti_5O_{12}$ (LTO) and high capacity SnO_2 for smart lithium-ion storage as shown in Figure I.12.

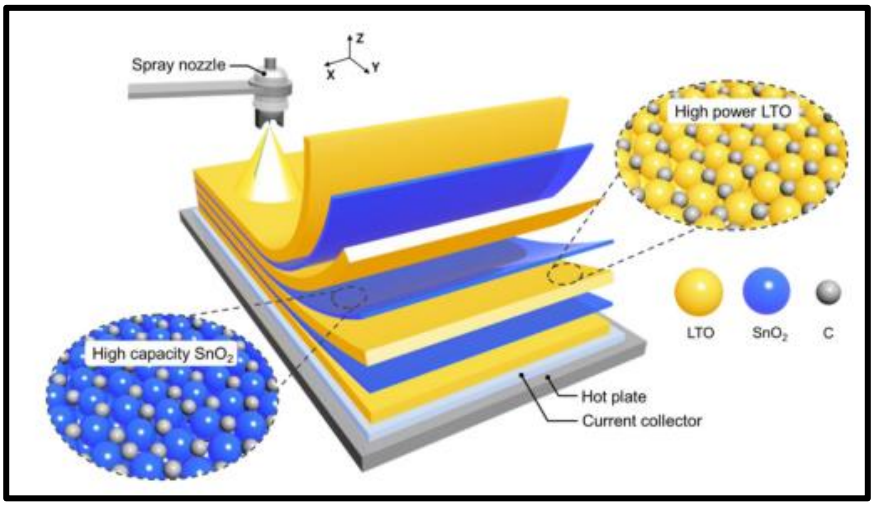

Figure I.12: Graphical illustration of the layer-by-layer spray printing of high power LTO and high capacity SnO_2 into a multi-layered hetero electrode. The left-hand and right-hand schematics depict the idealized particle arrangement of SnO_2 and LTO within the multi-layer [45].

Also we can found SnO_2 aerogel electrodes protects from corrosion for oxygen reduction in proton exchange membrane fuel cells (PEMFC) [46].

- **Surface coatings**

Tin oxide generally used as coating when it is doped with indium or Florine in many applications, such as:

- ✓ Low-Emissivity glass: (low-E glass) is employed to reflect the heat transmitted by infrared radiation with a long wavelength (approximately 10µm). When glass is coated with fluorine doped tin oxide (FTO), it becomes glass with high visible transmission and high infrared reflectivity. Therefore, the thickness of the layers has an essential role since a higher thickness leads to a higher infrared reflectivity but a lower visible transmission. In general, the FTO layer is 300-400 nm thick [47]. The following figure is an illustration of the low-E glass.

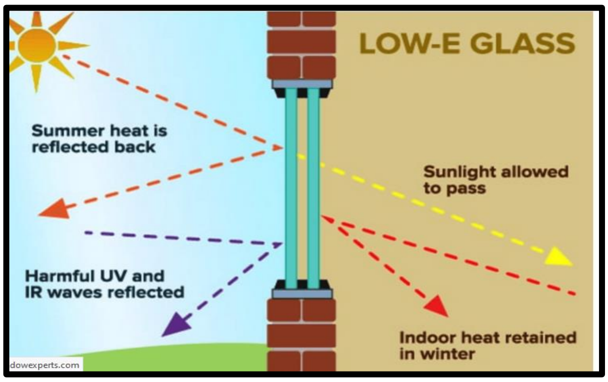

Figure I.13: schematic diagram of low-E glass.

- ✓ Heated mirrors (HMF): Chen Jie and Ge Xin-shi present their work on an application of HMF with thin layers of ITO [48], this type of mirrors is used in bathrooms.
- ✓ ITO is also used in the automotive world as a heating coating for exterior mirrors by the Joule effect [14].

I. 4.Photocatalytic process

In recent years, it have been many problems in the environment we want to eliminate it such as: air pollution, organic pollutants in the water......, photocatalysts are one of the most important methods to solve these problems, this word has two parts; "photo" is related to the light source which is usually the sun (UV part) , and "catalyse" which has a relation with the type of semi-conductor (or the fluid) responsible for the catalytic process, the discovery of this process was in

1972 through the scientific research of Fujishima and Holland [49], they showed that water could be decomposed into oxygen and hydrogen under UV irradiation, without application of an external voltage, in the presence of a semiconductor (TiO_2).

Photocatalysts has many applications, not only purifying water from organic pollutants, including them: the transformation of solar energy into chemical energy, the degradation of pollutants or even the manufacture of self-cleaning surfaces [50], hydrogen production [51]. There are two main types of catalysis depending on the nature of the catalyst:

- **Homogeneous:** the reactants and catalyst are combined into a single phase (generally liquid).
- **Heterogeneous:** the reactants and the catalyst are in two distinct phases, here the catalyst is often in solid form (metal oxide semiconductor) while reactants are in gaseous (like air) or liquid (like water) form. Therefore, the chemical reaction takes place on the surface of the catalyst, which means that the reactants must first be adsorbed on its surface for the reaction to take place.

Heterogeneous catalysis is a particular type of photocatalysis in which the source of energy, necessary for the activation of the reactions, is none other than light and not heat, Therefore, the most important semiconductors used are TiO_2, ZnO, WO_3, SnO_2, α-Fe_2O_3, CdS, ZnS …..etc [52], depending on the chosen catalyst, the energy required to activate the catalyst will be different, as shown in the Table I.3.

Table I.3: Comparison of semiconductors for photocatalytic activation [53].

Semiconductor	Band gap energy (eV)	Wavelength λ (nm)
TiO_2	3.2	390
ZnO	3.2	390
WO_3	2.8	443
SnO_2	3.7	336
α-Fe_2O_3	2.2	565
CdS	2.5	497
ZnS	3.7	336

I. 4.1. Work principle of heterogeneous photocatalysis

Heterogeneous photocatalysis consists in irradiating by the sun or by a UV lamp. The semiconductor is excited by radiation, the energy of which is greater than or equal to the energy of its band gap, which allows an electron from the valence band to be injected into the conduction band according to this relation:

$$\text{semiconductor} + h\nu \rightarrow e^- + h^+$$

In Figure I.14 we can represent the working principle of heterogeneous photocatalysis.

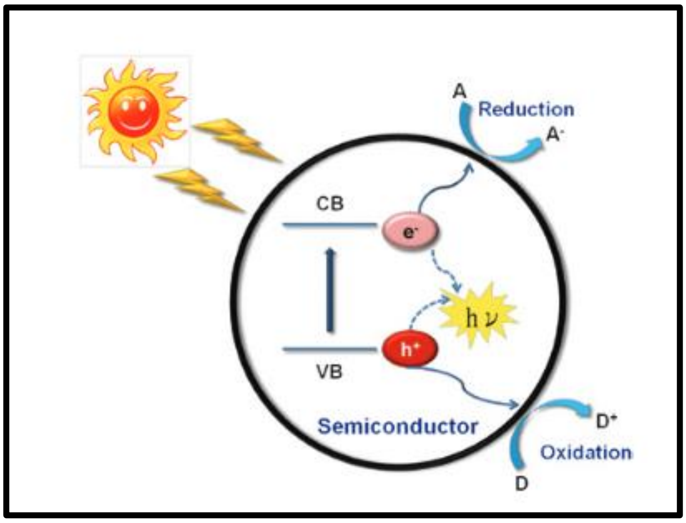

Figure I.14: Processes in photo catalytic reaction [54].

The photogenerated electrons and holes in the semiconductor have respectively reducing and oxidizing powers, which allow them to react with the species adsorbed on the surface of the photocatalyst. Only a part of these couples will be used in this process for the degradation of pollutants; the others will be recombined between them, so it does not produce any effect in depollution.

- ✓ The holes of the valance band of the semiconductor can oxidize donor molecules and react with water molecules to generate hydroxyl radicals (the hydroxyl radicals have strong oxidizing power responsible for the degradation of pollutants). This mechanism is explained in the following equations [52]:

$$H_2O + h^+_{VB} \rightarrow OH^{\cdot} + H^+ \qquad (1)$$

$$\text{polluting(Dyes)} + h^+_{VB} \rightarrow \text{polluting(Dyes)}^+ \qquad (2)$$

$$\text{polluting(Dyes)} + OH^{\cdot} \rightarrow CO_2 + H_2O \qquad (3)$$

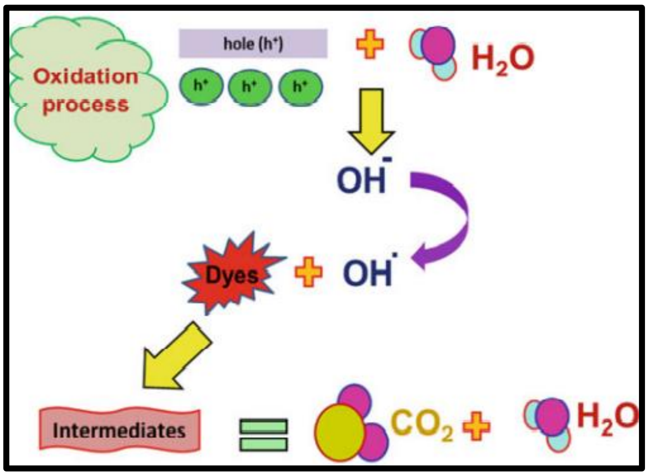

Figure I.15: Schematic representation of oxidation mechanism [55].

- ✓ The electrons of the conduction band react with the dissolved oxygen species to form superoxide ions. This mechanism is explained in the following equations [52]:

$$O_{2(adsorbed)} + e^-_{CB} \rightarrow O_2^{\cdot -}{}_{(adsorbed)} \qquad (1)$$

$$O_2^{\cdot -}{}_{(adsorbed)} + H^+ \rightarrow HO_2^{\cdot} \qquad (2)$$

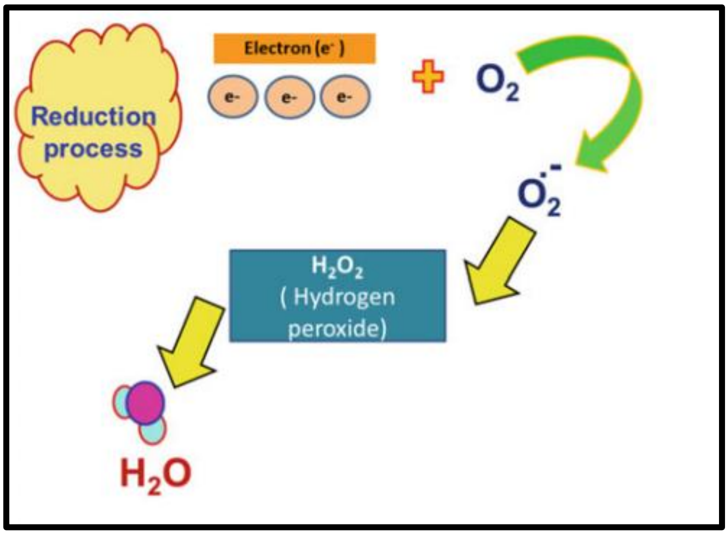

Figure I.16: Schematic representation of reduction mechanism [55].

I. 4.2. Advantages of photocatalysis

Photocatalysis has many advantages compared to the usual technologies, among which we can mention [23,55]:

- ❖ It works at atmospheric temperature and pressure.
- ❖ Effective at low concentrations of pollutants.
- ❖ Non-toxic, active in different physical forms.

- The photocatalytic process can be used in the destruction of a variety of hazardous compounds in different wastewater streams.
- Photocatalysis leads to the formation of harmless products, unlike conventional treatment measures which transfer pollutants from one phase to another.
- Photocatalysis offers a good replacement for the energy-intensive conventional treatment methods (adsorption on activated carbon, ultrafiltration, reverse osmosis, coagulation by chemical agents, and ion exchange on synthetic adsorbent resins) with the capacity for using renewable and pollution-free solar energy.

I. 4. 3. Limitations of photocatalysis

We can find few limitations compared to the advantages of this technology, which are [23]:

- The narrow band gap of semiconductor leads to the absorption of a small part of the solar spectrum.
- Recombination of photogenerated charges can decrease the efficiency of the process.
- Sometimes it requires energy consumption (UV irradiation), which limits the effectiveness of this technology in the visible region.

Among the proposed solutions to improve the efficiency of photocatalysis is the doping of the used semiconductor or we use heterostructure photocatalysts (semiconductor/semiconductor).

I. 4.4. Use of tin dioxide in photocatalysts

SnO_2 semi-conductor can be used in photocatalysis heterogeneous because it has excellent physical properties, so it can be used alone in the case of the oxidation of carbon monoxide this reaction follows the Mars-van Krevelen mechanism: the CO adsorbed on the surface of SnO_2 is oxidized by an oxygen atom coming from the lattice of SnO_2. SnO_2 is then re-oxidized by oxygen gas. This mechanism is made possible due to the possible double oxidation state of tin (Sn (IV) and Sn (II)). To improve the effectiveness of SnO_2 photocatalyst we can dope it with different elements such as antimony or vanadium [46], through research of Layciane A. Soares and al, SnO_2 doped with rhodium has a noticeable effect on carbon supported platinum catalysts for ethanol electro oxidation [56].. Also, we can improve its efficiency when we mix other oxides with tin oxide, so the oldest and most patented catalysts are catalysts based on the mixed vanadium oxide and tin oxide for the oxidation of aromatic compounds in the synthesis of organic acids and acid anhydrides [1], moreover, Rinky Sha and Sushmee Badhulika found that the graphene oxide (GO)

– Tin oxide (SnO_2) composite has an ultra-high performance catalyst for methanol electro-oxidation [57].

Coupling TiO_2 with another semiconductor with a suitable band edge position can effectively reduce the recombination by vectorial transfer of photogenerated electrons and holes. For example, SnO_2/TiO_2 system has recently attracted much attention due to enhanced charge separation and thus improved photocatalytic activity, both TiO_2 and SnO_2 are n-type semiconductors with band gap energies greater than 3.0 eV and exhibit a strong absorption threshold in the UV region. The conduction band edge of TiO_2 and SnO_2 are located at E_{CB} (TiO_2) = −0.5 V and E_{CB} (SnO_2) = 0 V at pH 7, respectively. The valence band edge of SnO_2 [E_{VB} (SnO2) = 3.67 V] is much positive than that of anatase TiO_2 [E_{VB} (TiO2) = 2.87 V]. Figure I.17 shows the charge transfer process in heterostructure SnO_2/TiO_2 photocatalysts. Upon band gap excitation, hole-electron pairs are generated in each semiconductor. Due to lower conduction band edge of SnO_2, electron will be injected into SnO_2, while the hole will move in the opposite direction of the electron and accumulate on the TiO_2 particles, thereby making charge separation more efficient. Therefore, the interfacial charge transfer process can explain the higher photocatalytic activity of SnO_2/TiO_2 composites [58].

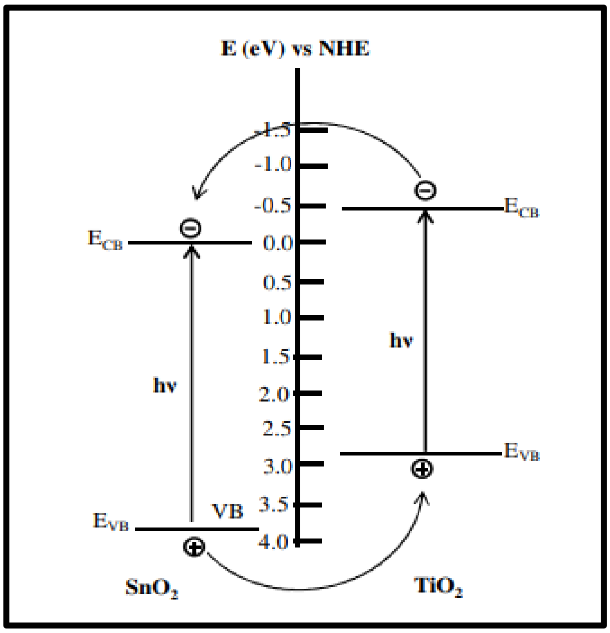

Figure I.17: Schematic representation of charge transfer process in heterostructure SnO_2/TiO_2 photocatalysts [58]

I. 5. Choice of SnO_2

The selection of SnO_2 in our work is not an accident; its transparency and semiconducting qualities have led us to expect an added value in performance.

This material has already proven itself in sensors, thermal coatings, and in all of the applications we mentioned at the beginning of this chapter, undoped SnO_2 as an antireflection layer can increase the transmission of incident photons and favour the increase of the short-circuit current in the technology of optical window and anti-reflective layer, it can also doped in order to increase its effectiveness in this application (since fluorine-doped tin oxide is a degenerate n-type semiconductor, the (SnO_2:F) N^{++}/(Si) N^{+} barrier can, by adding to that of the $N^{+}P$ junction, contribute to the increase in open circuit voltage) [59], and also it has increasing attention in the field of catalysis because of its chemical stability [23] which is one of the important characteristics of photocatalyst process.

I. 6. Purpose of this work

The purpose of this work is to deposit thin films of transparent conductive oxide (SnO_2) using spray pyrolysis technique, then we dope it with three alkaline earth elements which are: Ca, Sr, and Ba. These three elements have different ionic radii and higher than the ionic radii of Sn^{4+} (they are shown in Table I.4). And then we will characterize the effect of the addition of these three elements on structural, morphological, optical, and electrical properties of the prepared samples.

Table I.4: Atomic radius, ionic radius, and band gap energy of different chemical elements [26, 60,61, 62].

Chemical element	**Ionic radii (°A)**
Sn^{4+}	0.71
Ca^{2+}	1.12
Sr^{2+}	1.32
Ba^{2+}	1.35

References

[1] K. Mourad, “Elaboration et étude des couches minces d’oxyde d’étain”, University Constantine 1-Algeria, 2018.

[2] A. Catellani, A. Calzolari, Codoping and Interstitial Deactivation in the Control of Amphoteric Li Dopant in ZnO for the Realization of p-Type TCOs, Materials. 10 (2017), 332, http://doi.org/10.3390/ma10040332.

[3] L. Hu, R. H. Wei, X. W. Tang, W. J. Lu, X. B. Zhu, Y. P. Sun, Design strategy for p-type transparent conducting oxides Design strategy for p-type transparent conducting oxides, J. Appl. Phys. 128 (2020), 140902, http://doi.org/10.1063/5.0023656.

[4] L. Hu, R. Wei, J. Yan, D. Wang, X. Tang, X. Luo, W. Song, J. Dai, X. Zhu, C. Zhang, Y. Sun, $La_{2/3}Sr_{1/3}VO_3$ Thin Films : A New p-Type Transparent Conducting Oxide with Very High Figure of Merit, J. Adv. Electron. Mater. 4 (2018), 1700476, http://doi.org/10.1002/aelm.201700476.

[5] M. F. Hossain, M. A. H. Shah, M. A. Islam, M. S. Hossain, Transparent conducting SnO_2 thin films synthesized by nebulized spray pyrolysis technique: Impact of Sb doping on the different physical properties, Mater. Sci. Semicond. Process. 121 (2021), 105346, http://doi.org/10.1016/j.mssp.2020.105346.

[6] A. Abdel-Galil, M. S.A. Hussien, I.S. Yahia, Low cost preparation technique for conductive and transparent Sb doped SnO_2 nanocrystalline thin films for solar cell applications, Superlattices and Microstruct. 147 (2020), 106697, http://doi.org/10.1016/j.spmi.2020.106697.

[7] W. Allag, H. Guessas, M. Hemissi, M. Boudissa, Study of Erbium Doping Effect on Structural , Morphological and Optical Properties of Dip Coated ZnO Under Alkaline Conditions, Optik. 219 (2020), 165287, http://doi.org/10.1016/j.ijleo.2020.165287.

[8] H. Attouche, S. Rahmane, S. Hettal, N. Kouidri, Precursor nature and molarities effect on the optical, structural, morphological, and electrical properties of TiO_2 thin films deposited by spray pyrolysis, Optic. 203 (2020), 163985, http://doi.org/10.1016/j.ijleo.2019.163985.

[9] H. Nadjette, “Elaboration et caractérisation des couches minces d’oxyde d’indium dopées à l’étain et au brome obtenue par spray pyrolyse ultrasonique”, University of Biskra-Algeria, 2021.

[10] A. Abdlekrim, “Optimisation des conditions d’élaboration des couches minces d’oxyde d’étain SnO_2 par spray”, University of Biskra-Algeria, 2016.

[11] O.R. Alobaidi, P. Chelvanathan, B. Bais, K. Sopian, M.A. Alghoul, M. Akhtaruzzaman, N. Amin, Vacuum annealed Ga:ZnO (GZO) thin films for solar cell integrated transparent antenna application, Mater. Lett. 304 (2021), 130551, http://doi.org/10.1016/j.matlet.2021.130551.

[12] X. L. Huang, D.W. Ao, T. B. Chen, Y. X. Chen, F. Li, S. Chen, G. X. Liang, X. H. Zhang, Z. H. Zheng, P.Fan, High-performance copper selenide thermoelectric thin films for flexible thermoelectric application, Mater. Today Energy. 21 (2021), 100743, http://doi.org/10.1016/j.mtener.2021.100743.

[13] T. Harada, Thin-film growth and application prospects of metallic delafossites, Mater. Today Adv. 11 (2021), 100146, http://doi.org/10.1.16/j.matdv.2021.100146.

[14] S. Yahiaoui, “L’effet de la molarité des différentes sources d’étain sur les propriétés des couches minces d’oxyde d’étain SnO_2 élaborées par Spray Ultrasonique”, University of Biskra-ALgeria, 2014.

[15] P. Sivakumar , H. Sharma Akkera, T. R. Kumar Reddy, Y. Bitla, V. Ganesh, P. M. Kumar , G. S. Reddy, M. Poloju, Effect of Ti doping on structural , optical and electrical properties of SnO_2 transparent conducting thin films deposited by sol-gel spin coating, Opt. Mater. 113 (2021), 110845, http://doi.org/10.1016/j.optmat.2021.110845.

[16] B. Teldja, B. Noureddine, B. Azzeddine, T. Meriem, Effect of indium doping on the UV photoluminescence emission , structural , electrical and optical properties of spin-coating deposited SnO_2 thin films, *Int.* J. Light Electron Op*t. 209* (2020), 164586, http://doi.org/10.1016/j.ijleo.2020.164586.

[17] X. Zhang, X. Liu, H. Ning, W. Yuan, Y. Deng, X. Zhang, S. Wang, J. Wang, R. Yao, J. Peng, Characterization studies of the structure and properties of Zr-doped SnO_2 thin films by spin-coating technique, Superlattices and Microstruct. 123 (2018), 330-337, htttp://doi.org/10.1016/j.spmi.2018.09.016.

[18] F .Ynineb, “Contribution à l’élaboration de couches minces d’Oxydes Transparents Conducteurs (TCO),” University of Constantine-Algeria, 2010.

[19] Souad Laghrib, “Synthèse des films minces de : SnO_2, SnO_2: In par deux procédés physique et chimique et étude de leur caractérisation”, University of Setif- Algeria, 2010.

[20] K. Tawous, “Couches minces de SnO_2 nanocristallines obtenues par Sol-Gel et étude des conditions de leur cristallisation”, University of Setif– Algeria, 2007.

[21] S. Zhang, “Study of fluorine-doped tin oxide (FTO) thin films for photovoltaics applications”, University of Grenoble Alpes- Paris.

[22] A. Abdelkrim, S. Rahmane, O. Abdelouahab,N. Abdelmalek, Gasmi Brahim, Effect of solution concentration on the structural, optical and electrical properties of SnO_2 thin films prepared by spray pyrolysis, Optik. 127 (2016), 2653-2658, http://doi.org10.1016/j.ijleo.2015.11.232.

[23] H. Soumia, “Elaboration des nanostructures de semi-conducteur SnO_2 dopé au Strontium et étude de leurs propriétés structurales,optiques et photocatalytiques,” University of Constantine-Algeria, 2018.

[24] P. Sivakumar, H. Sharma Akkera, T. R. K. Reddy, G. S. Reddy, N. Kambhala, N. N. K. Reddy, Influence of Ga doping on structural, optical and electrical properties of transparent conducting SnO_2 thin films, Optik. 226 (2021), 16859, http://doi.org/10.1016/j.ijleo.2020.165859.

[25] A. Janotti, Oxygen vacancies in ZnO, Applied Physics Letters, 87 (2005), 122102, http://doi.org/10.1063/1.2053360.

[26] C. H. Kim, Y. S. Rim, D. L. Kim, H. J. Kim, Combined effect of the large ionic radius and low electronegativity of lanthanum additive on solution-processed zinc-tin-oxide thin-film transistors, Thin Solid Films. 536 (2013), 291-294, http://doi.org/10.1016/j.tsf.2013.04.018.

[27] R. Ramarajan, M. Kovendhan, K. Thangaraju, D. P. Joseph, R. R. Babu, V. Elumalai, Enhanced optical transparency and electrical conductivity of Ba and Sb co-doped SnO_2 thin films, Alloy. Compd.823 (2020), 153709, http://doi.org10.1016/j.jallcom.2020.153709.

[28] Q. Dong, S. Yin, M. Yoshida, X. Wu, B. Liu, A. Miura, T. Takei, N. Kumada, T. Sato, Alkaline earth metal doped tin oxide as a novel oxygen storage material, Mater. Res. Bull. 69 (2015), 116-119, http://doi.org/10.1016/j.materresbull.2014.11.018.

[29] L. Segueni, “Study and elaboration of Fe/Li-doped SnO_2 thin films” University of Constan Eloued-Algeria, 2018.

[30] M. Sharma, R. Naji Aljawfi, K. Kumari, K.H. Chae, S. Dalela, S. Gautam, P.A. Alvia, S. Kumar, Investigation of local geometrical structure , electronic state and magnetic

properties of PLD grown Ni doped SnO_2 thin films, J. Electron Spectros. Relat. Phenomena. 232 (2019), 21-28, http://doi.org/10.1016/j.elspec.2019.01.002.

[31] S. Liu, X. Qiao, Y. Wang, H. Xie, N. Zhang, D. Liu, Magnetic and optical behaviors of SnO_{2-x} thin fi lms with oxygen vacancies prepared by atomic layer deposition, Ceram. Int. 45 (2019), 4128-4132, http://doi.org/10.1016/j.ceramint.2018.11.040.

[32] F.F.H. Aragón, J.C.R. Aquino, J.D. Ardisson, J.A.H. Coaquir, Thermal annealing effects on the structural , magnetic and hyper fi ne properties of the Fe / SnO_2 / Fe thin film deposited by RF sputtering method, Mater. Sci. Semicond. Process. 93 (2019), 182-187, http://doi.org/10.1016/j.mssp.2019.01.004.

[33] S. Gupta, F. Singh, N.P. Lalla, B. Das, Swift heavy ion irradiation induced modifications in structural , microstructural , electrical and magnetic properties of Mn doped SnO_2 thin films, Nucl. Inst. Methods Phys. Res. B. 400 (2017), 37-57, http://doi.org/10.1016/j.nimb.2017.03.155.

[34] F. Hild, "Étude de la structure et des propriétés optiques de couches minces d ' oxydes d'étain dopés avec des terres rares (Ce , Tb , Yb)," University of Lorraine- Paris, 2017.

[35] L. Wang,Y. He, D. Liu, L. Liu, H. Chen, Q. Hu, X. Liu, A. Zhou, SnO_2 Quantum Dots Interspersed d-Ti_3C_2 Tx MXene Heterostructure with Enhanced Performance for Lithium Ion Battery, J. Electrochem. Soc. 167 (2020), 116522, http://doi.org/10.1149/1945-7111/aba705.

[36] A. Bediaa, F.Z. Bediaa, M. Aillerie, N. Maloufi, B. Benyoucef, Morphological and Optical Properties of ZnO Thin Films Prepared by Spray Pyrolysis on Glass Substrates at Various Temperatures for Integration in Solar Cell, Energy Procedia. 74 (2015), 529-538, http://doi.org/10.1016/j.egypro.2015.07.740.

[37] F. Zhao, Y. Yi, J. Lin, Z. Yi, F. Qin, Y. Zheng, L. Liu, F. Zheng, H. Li, P. Wu, The better photoelectric performance of thin-film TiO_2 / c-Si heterojunction solar cells based on surface plasmon resonance, Results Phys. 28 (2021), 104628, http://doi.org/10.1016/j.rinp.2021.104628.

[38] Hamid Latif, J. Liu, D. Mo, R. Wang, J. Zeng, P.F. Zhai, A. Sattar, Effect of Target Morphology on Morphological , Optical and Electrical Properties of FTO Thin Film Deposited by Pulsed Laser Deposition for $MAPbBr_3$ Perovskite Solar Cell, Surfaces Interfaces. 24 (2021), 101117, http://doi.org/10.1016/j.surfin.2021.101117.

[39] S. Noureen, “New Dithienylpyrrole-containing bipyridine ligands and corresponding Ruthenium complexes. Electronic properties and applications to photosensitization in Dye-Sensitized Solar Cells”, University of Lorraine- Paris, 2012.

[40] Thi Ly Le, “Preparation of Transition Metal Oxide Thin Films used as Solar Absorbers”, University of Toulouse-Paris, 2016.

[41] C. Tropis, “Analyse et Optimisation des performances d’un capteur de gaz à base de SnO2 nanoparticulaire : Application à la détection de CO et CO_2”, University of Toulouse- Paris, 2009.

[42] A. Abdelghani, “Capteur de gaz hyperfréquence à base de nanotubes de carbone imprimé par technologie jet d’encre”, University of Limoges-Paris, 2018.

[43] B. Ghaddab, “Développement d’un capteur de gaz à base de couche hybride dioxyde d’étain / nanotubes de carbone”, University of Franche-Paris, 2015.

[44] C. Pijolat, “Utilisation des oxydes métalliques comme matériaux semi-conducteurs pour la détection des gaz”, 1996.

[45] S. H. Lee, C. Huang, P. S. Gran, Multi-layered composite electrodes of high power $Li_4Ti_5O_{12}$ and high capacity SnO_2 for smart lithium ion storage, Energy Storage Mater. 38 (2021), 70-79, http://doi.org/10.1016/j.ensm.2021.02.010.

[46] G. Ozouf, “Electrodes à base d’aérogels de SnO_2, résistantes à la corrosion pour la réduction de l’oxygène dans les piles à combustible à membrane échangeuse de protons (PEMFC)”, University of PSL Research-Paris, 2018.

[47] B. Kheira, “Elaboration and characterization of SnO_2:In thin films deposited by spray pyrolysis technique”, University of Biskra-Algeria, 2020.

[48] C. Jie, G. Xin-shi, H. Xing-fang, Single-layer heat mirror films and an improved method for evaluation of its optical and radiative properties in infrared, Solar Energy Materials & Solar Cells. 55 (1998), 323-329, http://doi/0 9 2 7 - 0 2 4 8 (9 8)0 0 0 9 4 - 4.

[49] L. Holland, “Electrochemical photolysis of water at a semiconductor electrode”, Nature, 238 (1972), 37-38, http://doi.org/10.1109/1972-1111/als703.

[50] P. Birnal, “Films minces micro/nanostructur´es : synth`ese par ALD de composites associant opales inverses de TiO_2 et nanoparticules d’or pour des applications photocatalytiques”, University of Bourgogne-Paris, 2021.

[51] J. Rodriguez, “Production d’hydrogène par photocatalyse et conversion électrochimique dans une pile à combustible”, University of Grenoble-Paris, 2014.

[52] F. Barka-Bouaifel, “Détection d’interactions moléculaires par LSPR et Utilisation de surfaces semi-conductrices pour la dégradation photocatalytique de polluants organiques sous irradiation visible”, University of Béjaià,-Algeria, 2012.

[53] T. Triquet, “Procédé hybride couplant adsorption et photocatalyse pour le traitement de l’eau: élimination de la ciprofloxacine par des fibres de charbon actif fonctionnalisées avec du TiO_2”, University of Toulouse-Paris, 2021.

[54] W. Jiao, W. Shen, Z. Ur Rahman, D. Wang, Recent progress in red semiconductor photocatalysts for solar energy conversion and utilization, Nanotechnol Rev. 5 (2016), 135-145, http://doi.org/10.1515/ntrev-2015-0052.

[55] R. Saravanan, F. Gracia, A. Stephen, Basic Principles , Mechanism , and Challenges of Photocatalysis, Springer Ser. Polym. in: R. Saravanan, F. Gracia, A. Stephen (Eds), Nanocomposites for Visible Light-induced Photocatalysis, Springer, 2017, pp. 19-40.

[56] L. A. Soares, C. Morais, T. W. Napporn, K. B. Kokoh, P. Olivi, Beneficial effects of rhodium and tin oxide on carbon supported platinum catalysts for ethanol electrooxidation, Journal of Power Sources, 315 (2016), 47-55, http://doi.org/10.1016/j.jpowsour.2016.03.013.

[57] R. Sha, S. Badhulika, Facile synthesis of three-dimensional platinum nano fl owers on reduced graphene oxide – Tin oxide composite : An ultra-high performance catalyst for methanol electro-oxidation, J. Electroanal. Chem. 820 (2018) 9-7, http://doi.org.10.1016/j.jelechem.2018.04.057.

[58] M. T. Uddin, “Metal oxide heterostructures for efficient photocatalysts”, UNIVERSITY OF Darmstadt-Germany, 2013.

[59] R. Zair, “Etude et Realisation d’une Cellule Photovoltaique a Heterostructure avec Contact Serigraphie”, University of Boumerdes-Algeria, 2007.

[60] S. Roguai, A. Djelloul, Elaboration, characterization and applications of SnO_2, 2 % Gd-SnO_2 and 2 % Gd-9 % F-SnO_2 thin films for the photocatalytic degradation of MB by USP method, Inorg. Chem. Commun. 138 (2022), 109308, http://doi.org/10.1016/j.inoche.2022.109308.

[61] M. Sellami, N. Nguyen, A. Bekka, N. Bettahar, Synthèse et étude des propriétés

magnétiques avec M = Ca et Pb, Comptes Rendus Chim. 9 (2006), 1209-1214, http://doi.org/10.1016/j.crci.2006.02.001.

[62] P.C. Preethi, A. Harisankar, U.S. S. Mol, R. Raghunandan, Synthesis of oxydiacetate functionalized strontium coordination polymer through gel diffusion technique: A new dual luminescent chemosensor for the detection of Copper(II) ions and Cr(VI) oxyanions in aqueous medium, Polyhedron. 223 (2022), 115974, http://doi.org/10.1016/j.poly.2022.115974.

Chapter II:

Elaboration and characterisation of SnO_2 thin films

In this chapter, the deposition procedure will be outlined, encompassing a description of the spray pyrolysis technique and its corresponding device, as well as substrate preparation. Subsequently, the details of the procedures employed to prepare the solutions for depositing the samples will be provided. Additionally, the characterization techniques applied to analyse the thin films in this study will be presented. These techniques include X-ray diffraction (XRD), scanning electron microscopy (SEM), energy dispersive X-ray (EDX/EDS), UV-visible spectrophotometry, and four-point probe for detecting structural, morphological, chemical composition, optical, and electrical properties, respectively.

II.1. Deposition procedure

II.1.1. Spray pyrolysis technique

Spray pyrolysis is a relatively very simple technique and it uses inexpensive means, It allows to obtain thin or thick films, even multilayered films can be easily prepared with it, however it can used to deposit a wide choice of materials especially transparent conducting oxides (TCOs).This technique can be classify into several types based on the type of energy source for the precursor reaction , the most important of them are: ultrasonic spray technique (UST) which is based on an ultrasonic wave generator atomizes the solution, and pneumatic spray technique (PST) is depends to a relatively pressurized air flow carry the solution that contains precursors, each one of these techniques can be categorized into four different procedures depending on the temperature (Figure.II.1):

Process 1: the droplet reaches on the substrate; the solvent evaporates leaving a precipitate, which then decomposes, in the solid state.

Process 2: the solvent evaporates before the droplet reaches the surface to be coated and the precipitate hits the substrate, decomposing into the solid phase.

Process 3: the solvent evaporates, the precipitate melts and vaporizes (or sublimes). There is then diffusion of the vapours towards the substrate and production of a reaction in a heterogeneous phase during contact. This is the classic chemical vapor deposition process. We can notice that it is then possible to define, as in CVD, an evaporation zone and a reaction zone, the evaporation zone presenting, here, a more complex profile, since the solvent must be evaporated.

Process 4: at higher temperature, the chemical reaction no longer takes place in a heterogeneous phase, but in a homogeneous (gaseous) phase with the production of fine powder particles, which can be deposited on the substrate.

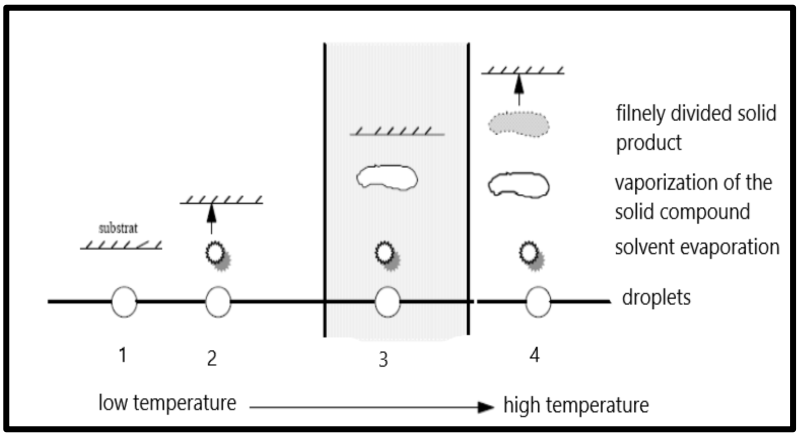

Figure.II.1. Diagram of decomposition of an aerosol as a function of temperature [1].

II.1.2. Description of the pneumatic spray technique (PST) deposition device:

The material used to deposit SnO_2 thin films is a homemade pneumatic spray pyrolysis technique. Figure.II.2 show a schematic diagram of this process.

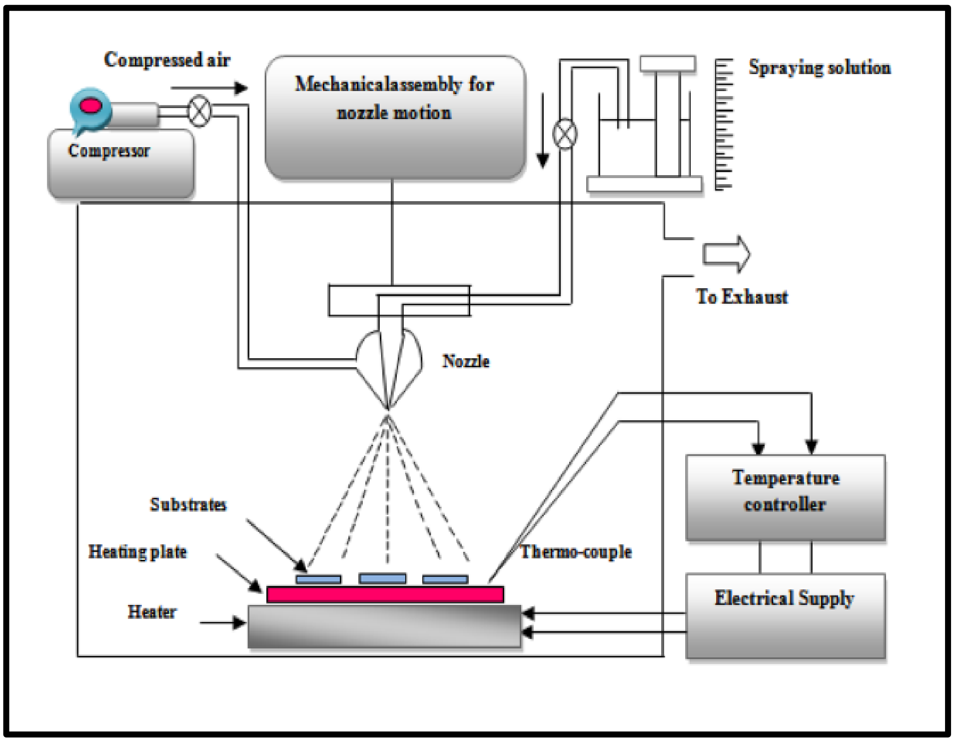

Figure.II.2. Schematic diagram of pneumatic spray pyrolysis technique [2].

II.1.3. Substrate preparation

- **Choice of substrate**

The glass was chosen as a deposition substrate because of the compatibility between its thermal expansion coefficient and of tin dioxide (α_{glass}=9.01*10^{-6} $^{\circ}C^{-1}$ [3], α_{SnO2}=14.16*10^{-6} $^{\circ}C^{-1}$

[4] at nearly 500 °C), which can lower the strain of substrate/film interfaces, for economic reasons, also it has high transparency in the visible region which adapts well to the optical characterization of SnO_2 thin film, the glass substrate is an insolent material which lead to detecting just the electrical conductivity of the thin film using four-point probe .

- **Cleaning of substrate**

The adhesion and quality of thin films, purity and surface condition are essential factors to control them before the deposition that is why we follow the following steps was done to clean the substrate:

- Rinsing with distilled water.
- Rinsing with acetone for a few minutes.
- Rinsing again with distilled water.
- Rinsing with ethanol.
- Cleaning in the distilled water bath for the last time.

Where it was dried with absorbent paper between each cleaning step and the other.

II.1.4. Chemical preparation of solutions and deposition of thin films

The tin dioxide (SnO_2) thin films were prepared from a tin chloride salt ($SnCl_2,2H_2O$) dissolved in methanol and distilled water in a volume ratio of 1/1 according to a molar concentration of the solution equal to 0.5 mol/l for tin chloride. A little hydrochloric acid (HCl) was added to the solutions is necessary to ensure maximum dissolution of $SnCl_2$ and a more homogenous solution. For the doping of the thin films dissolve quantities of ($CaCl_2$, $2H_2O$), ($SrCl_2$, $6H_2O$), and ($BaCl_2$, $2H_2O$) according to the desired condition of Ca, Sr, and Ba doping. The mass ratio percentage of Ca, Sr, and Ba to tin (Ca/Sn; Sr/Sn; Ba/Sn) is varied in the range of 0-8 wt %. The final solution was deposited by the spray pneumatic technique with a moving nozzle onto cleaned and heated glass substrates at a fixed temperature of 450 °C for 12 minutes to obtain a uniform and homogenous pure and doped SnO_2 films.

II.1.5. Different physico-chemical properties of the elements used

- **Tin (II) chloride dihydrate**

- ***Chemical Names:*** Stannous chloride; Stannous chloride dehydrate; Dihydrated stannous chloride; Tin dichloride dihydrate; Stannochlor
- ***Appearance:*** White crystalline solid
- ***Molecular Formula:*** $SnCl_2.2H_2O$

- ***Molecular Weight:*** 225.63 g/mol
- ***Density:*** 2.71 g/cm^3.
- ***Melting point:*** 38 °C
- ***Boiling point:*** 652 °C
- ***Reference [C.A.S]:*** 10025-69-1.

  - **Calcium chloride dihydrate**

- ***Chemical Names:*** Neutral calcium chloride; Calcium (II) chloride, Calcium dichloride.
- ***Appearance:*** White hygroscopic powder.
- ***Molecular Formula:*** $CaCl_2$, $2H_2O$.
- ***Molecular Weight:*** 147.02 g/mol.
- ***Density:*** 1.85 g/cm^3.
- ***Melting point:*** 175 °C
- ***Reference [C.A.S]:*** 10035-04-8.

  - **Strontium chloride hexahydrate**

- ***Chemical Name:*** Strontium (II) chloride.
- ***Appearance:*** White crystalline solid.
- ***Molecular Formula:*** $SrCl_2$, $6H_2O$.
- ***Molecular Weight:*** 266.62 g/mol.
- ***Density:*** 1.930 g/cm^3.
- ***Melting point:*** 61 °C
- ***Reference [C.A.S]:*** 10025-70-4.

  - **Barium chloride dihydrate**

- ***Chemical Name:*** Barium muriate, Muryate of barytes, Barium dichloride crystals, Natural barium chloride.
- ***Appearance:*** White solid.
- ***Molecular Formula:*** $BaCl_2$, $2H_2O$.
- ***Molecular Weight:*** 244.27 g/mol.
- ***Density:*** 3.0979 g/cm^3.
- ***Melting point:*** 960 °C
- ***Reference [C.A.S]:*** 10326-27-9.

    - **Methanol**

- ***Chemical Names:*** Methylol, Methyl alcohol, Wood alcohol, Carbinol, Wood naphtha.
- ***Molecular Formula:*** CH_4O.
- ***Appearance:*** Colourless liquid.

- ***Molecular Weight:*** 32.04 g/mol.
- ***Density:*** 0.792 g/cm^3.
- ***Melting point:*** -97.8 °C
- ***Reference [C.A.S]:*** 67-56-1.

  - **Ethanol**

- ***Chemical Names:*** Absolute alcohol, alcohol, Htdrooxyethane, Ethyle hydrate.
- ***Molecular Formula:*** C_2H_6O.
- ***Appearance:*** Colourless liquid.
- ***Molecular Weight:*** 46.07 g/mol.
- ***Density:*** 0.78945 g/cm^3.
- ***Melting point:*** -114.14 °C
- ***Reference [C.A.S]:*** 64-17-5.

II.2. Characterization methods for SnO_2 thin films

The identification of materials is generally done by determining their physical properties, which require characterization techniques, we give in the following an overview of the techniques used to characterize the structural, morphological, optical, and electrical properties of thin films, but before doing any characterization we need to evaluate the adhesion strength between the films and the substrates by washing the sample with distilled water or applying the stick tape test.

II.2.1. Structural properties

- **X- Ray Diffraction (XRD)**

A diffractometer is composed of an X-ray source monochromatic; a goniometric step ensuring the angular displacement of the sample and a detector associated with the measurement chain. When the monochromatic X-ray beam directed on a material part of the energy diffused, that is mean the radiation of the same wavelength as the incident radiation was emitted in directions different from those of the primary beam. These emitted radiations are the source of the information to be collected on the material. Figure. II.3. show the principle of the XRD technique

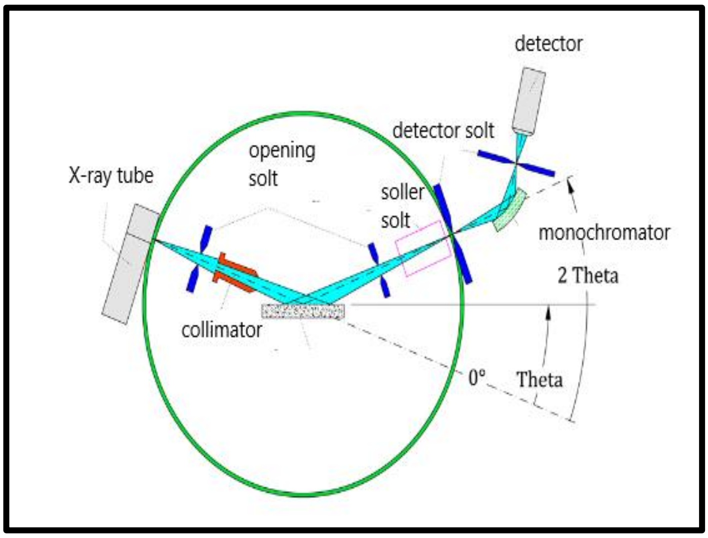

Figure. II. 3. Schematic diagram of the X-ray diffractometer [5].

The fundamental idea for X-ray diffraction was considered on Bragg’s law. Each atom acts as a source of scattering when a monochromatic X-rays interact with it in the crystal lattice, and this last one functions as a group of parallel reflecting planes. At specific angles, the intensity of the reflected rays reaches the maximum (this is what we call constructive interference). The Bragg's law presented by the following formula:

$$2\, d_{hkl} \sin\theta = n\, \lambda \qquad \text{(II.1)}$$

Where:

d_{hkl}: interplanar spacing.

θ: diffraction angle.

λ: wavelength of x-ray.

n: order of diffraction.

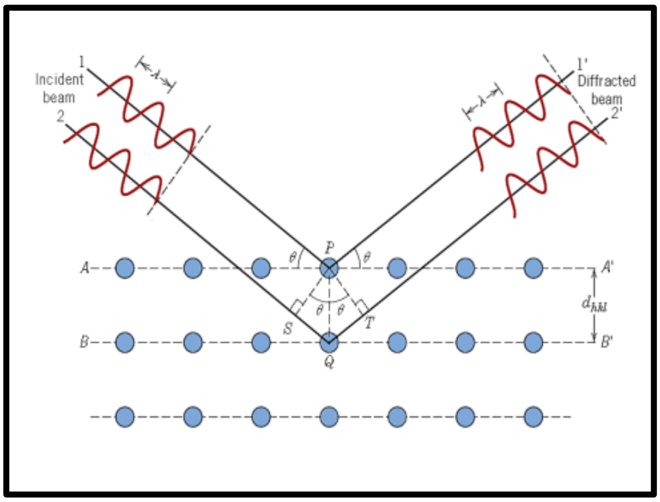

Figure.II.4. Schematic description of Bragg's law [6].

The analysis of our samples was carried out at the thin film laboratory and their applications in Biskra University, our device type Rigaku-Mini Flex 600 is composed of an X-ray source using a copper anticathode emitting an X-ray beam produced from a Cu $_{K\alpha}$ radiation source having a wavelength (λ = 0.154056 nm) in the angular range 20° to 80°.

From the XRD characterization, we can provide many structural properties such as texture coefficient (TC), lattice parameters (a, b, and c), crystallite size (D), dislocation density (δ), micro strain (ε).

The texture coefficient (TC) measures the relative degree of preferred orientation in the thin film among crystal planes, it given by the following expression [7]:

$$TC = [I_{(hkl)}/\ I_{(0\ hkl)}]/[N^{-1}\ \textstyle\sum_{N}(\ I_{(hkl)}/I_{(0\ hkl)})] \qquad (II.2)$$

Where:

$I_{\ (hkl)}$: is the measured intensity.

$I_{\ (0\ hkl)}$: is the standard intensity of the plane (hkl) according to the JCPDS data.

N: is the number of diffraction peaks.

The lattice parameters (a, b, and c)which gives the dimensions’ cell, it can be calculate for the tetragonal SnO_2 rutile structure by the equations below [8]:

$$\frac{1}{d^2} = \frac{(h^2+k^2)}{a^2} + \frac{l^2}{c^2} \qquad (II.3)$$

$$c/a = 0.672 \qquad (II.4)$$

Where: d_{hkl} is the interplanar distance and (h k l) is the Miller indices.

The crystallite size (D) at preferred peak estimated by Scherer's equation [9]:

$$D = K\,\lambda/\beta.\cos(\theta) \qquad (II.5)$$

Where:

K: is a constant equal 0.9 for the grains, which have a shape near to spheres.

λ: is the wavelength of the incident X-ray beam.

β: is the full width at half maximum (FWHM) of the preferred peak.

Θ: is the position of the diffraction peak considered.

The dislocation density (δ) is defined as the length of dislocations lines per unit of volume of the crystal can be evaluated as follows [10]:

$$\delta = 1/D^2 \qquad (II.6)$$

The micro (ε) strain values of the thin films were measured from the following equation [11]:

$$\varepsilon = \beta.\cos(\Theta)/4 \qquad (II.7)$$

Moreover, if there are many peaks preferred in XRD data we use Williamson-hall formula [12]:

$$\beta.\cos(\Theta)/\lambda = (0{,}9/D) + (4\varepsilon.\sin(\Theta)/\lambda) \qquad (II.8)$$

II.2.2. Morphological properties

- **Scanning electron microscope (SEM)**

The scanning electron microscope (SEM) is a specific type of electron microscope that can create 2D photos and shows the sample's morphology and topography features, which enables us to investigate our nanostructures' diameter, length, shape, and density. This technique is based on the interaction of an incident mono-kinetic electron beam with a high-energy (in order of KeV) with the material to be analysed (electron-matter interaction). The electron beam is produced at the top of the device using an electron gun placed in a column maintained under the void, the electrons are obtained by heating a filament. The primary electron beam thus formed follows a vertical path in the column of the microscope, through electromagnetic lenses and deflector coils the electron beam focused and directed down toward the sample (Figure.II.5).

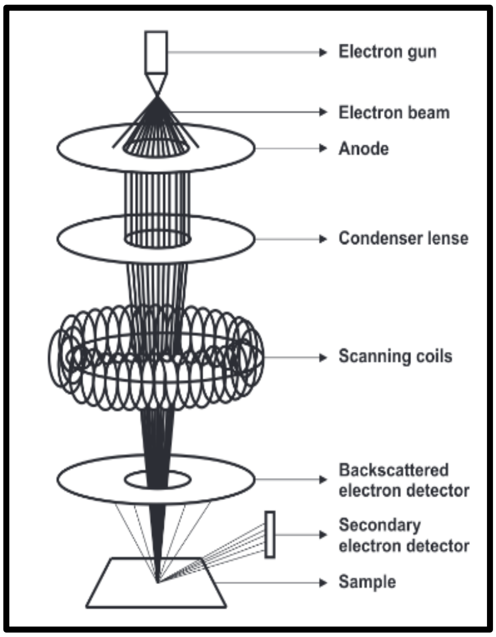

Figure. II.5. Scanning electron microscope (SEM) principle[13].

The interaction between the electrons and the sample causes the ejection of secondary electrons allows to have a very precise visualization of the topography and morphology of the surface, backscattered electrons which arise from elastic interactions between incident electrons and atomic nuclei [14], Auger electrons, and X-ray photons [15](Figure.II.6).

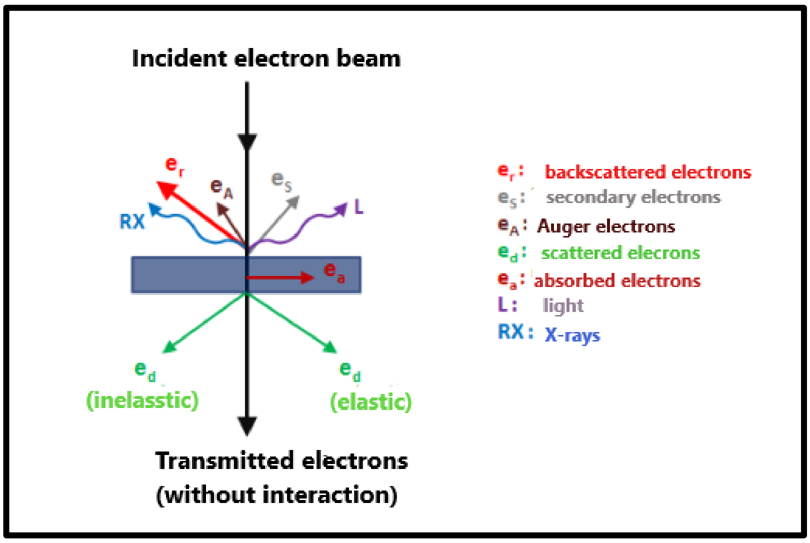

Figure.II.6. Schematic representation of the interaction between a beam of electrons and the surface of a sample [16].

- **Energy dispersive X-ray spectroscopy (EDS or EDX)**

The chemical composition of the deposited films (the chemical elements present in a sample) was estimated by microanalysis X which is called energy dispersive X-ray spectroscopy (EDS or EDX) it can provide elemental analysis on regions with a small diameter of the order of a nanometre, and its analysis accuracy is 1%.

The X photons emitted during the interaction of the electrons with the film, make it possible to fulfil the chemical analysis, moreover, the energy of the incident electrons is in the range of energy of the electrons occupying the levels of the atoms corresponding to K, L, and M lines. During the shock, some atoms lose an electron and move to an excited state. When a free electron comes to occupy a vacant place an X photon is emitted. The spectrometer composed of a semiconductor detector (a diode) makes it possible to collect the X photons and to measure the energy "hv" of each photon emitted, for example, a peak corresponding to the amount of energy possessed by X-rays emitted by an electron in the L-shell going to the K-shell is identified as a K-alpha peak, the peak corresponding to X-rays emitted by M-shell electrons going to the K-shell identified as K-beta peak (Figure.II.7). Through Einstein's relationship "ΔE=hv" ("ΔE" is the energy difference between the fundamental and excited atomic levels of the atom concerned), it is easy to recognize the atoms responsible for the emission. Once the spectrum has been acquired, the identification of the peaks is simple and assumes a prior energy calibration of the spectrometer, the quantification is carried out automatically.

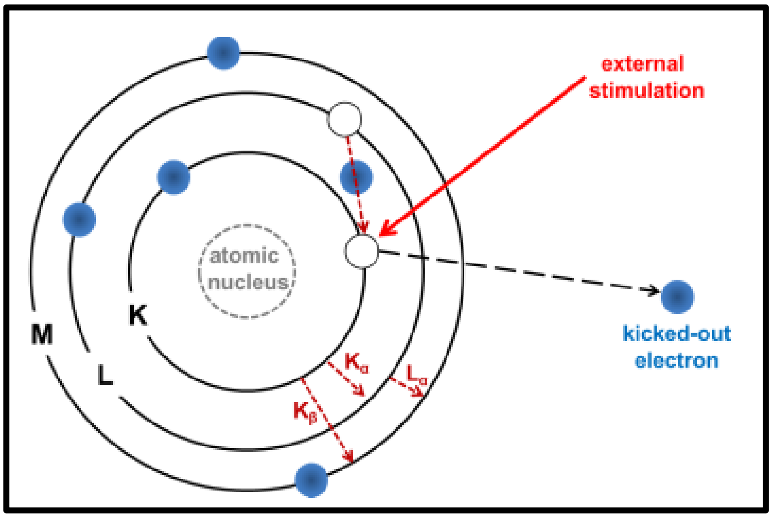

Figure.II.7. Scheme of an atom for explanation of the principle of EDX [17].

II.2.3. Optical properties

- **UV-visible spectrophotometer**

The quantitative measurement of transmission or reflection is done using UV-vis spectrophotometer. In our research, we used a double-beam recording UV-vis spectrophotometer model JASCO V-770 to measure just the transmittance, where its operating principle is shown in Figure II-8.

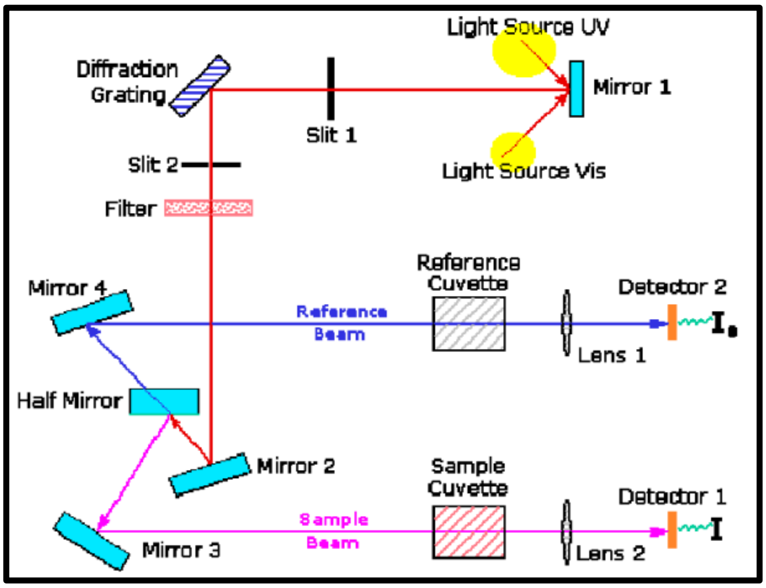

Figure II-8. Principle of operation of the UV-visible spectrophotometer[18].

Where we can measure the UV visible range curves representing the transmittance variance as a function of wavelength (Figure II-9), firstly, to obtain accurate optical transmittance curves, the thin films must be deposited onto transparent glass substrates, since it does not absorb light in the spectral range under study, then a substrate does not contain any film deposited is placed in the spectrophotometer reference beam to plot “T= f (λ)” spectres, after that, a computer connected to this device reproduces the spectres which representing the transmittance as a function of the wavelength of the incident beam.

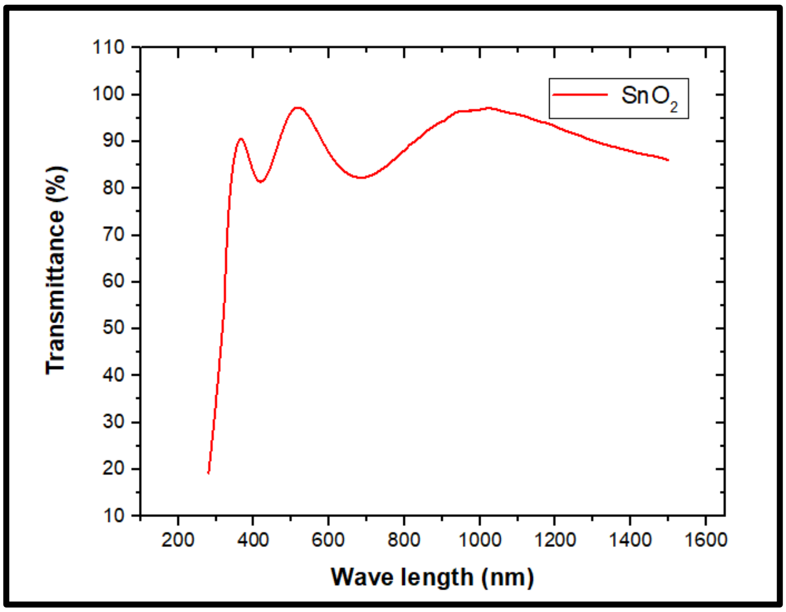

Figure II-9. Transmittance spectrum as a function of wavelength of pure SnO_2.

In addition, by using these curves, it is possible to estimate several values, including them: film thickness (d), absorption coefficient (α), band gap energy (E_g), Urbach energy (E_u), and refractive index (n). An explanation of how to calculate the most important of these quantities is provided in the following paragraphs:

- ✓ **Absorption coefficient (α):** the absorption coefficient presented using Bouguer-Lambert Beer law by neglecting the reflected light or often simply called; Beer-Lambert's law [19]:

$$T = e^{-\alpha d} = \left(\frac{I}{I_0}\right) \qquad (II.9)$$

And

$$T(\%) = \frac{I}{I_0}.100 \qquad (II.10)$$

Then the absorption coefficient is given by:

$$\alpha = \frac{1}{d}.\ln\left(\frac{100}{T(\%)}\right) \qquad (II.11)$$

Where:

T: the transmission part of the light.

I_0: the intensity of the incident beam.

I: the intensity of the transmitted beam.

d: the film thickness.

α: the absorption coefficient.

- ✓ **Band gap energy:** for crystalline materials, the energy separating the valence band from the conduction band is known as E_v and E_c. The difference between them (E_c-E_v) is called band gap energy (E_g), this value can be deduced by applying Tauc's model equation for direct band gap semiconductors [20]:

$$(\alpha\, h\nu)^2 = A(h\nu - E_g) \tag{II.12}$$

Where:

A: is constant.

E_g: the band gap energy.

hv: the photon energy.

We plot $(\alpha\ h\nu)^2$ for all wavelengths in the studied range in terms of photons energy (hv), then we extrapolate the linear part of $(\alpha\ h\nu)^2$ to the photon's energy axis (that is mean $(\alpha\ h\nu)^2=0$), after that, we get 'E_g' value.

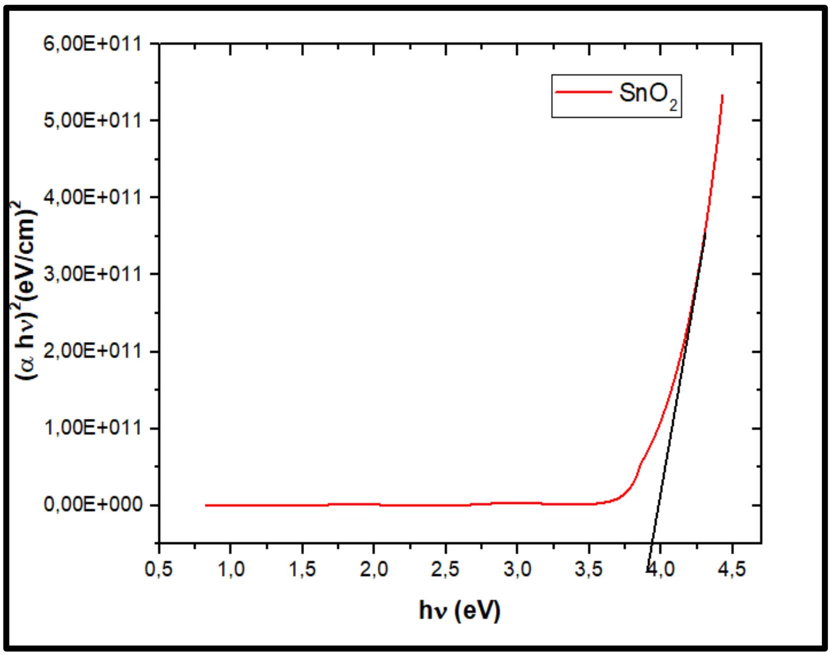

Figure II-10. Determination of band gap energy E_g of pure SnO_2.

- ✓ **Urbach energy:** when there are variations in interatomic distances, bond lengths, or angles in a material, appears what we called a "disorder or Urbach energy (E_u)", in this case, the edges of the valence band and the conduction band known as "E_v" and "E_c" may disappear, and we observe what we call band tails at bandgap boundaries (Figure II-11).

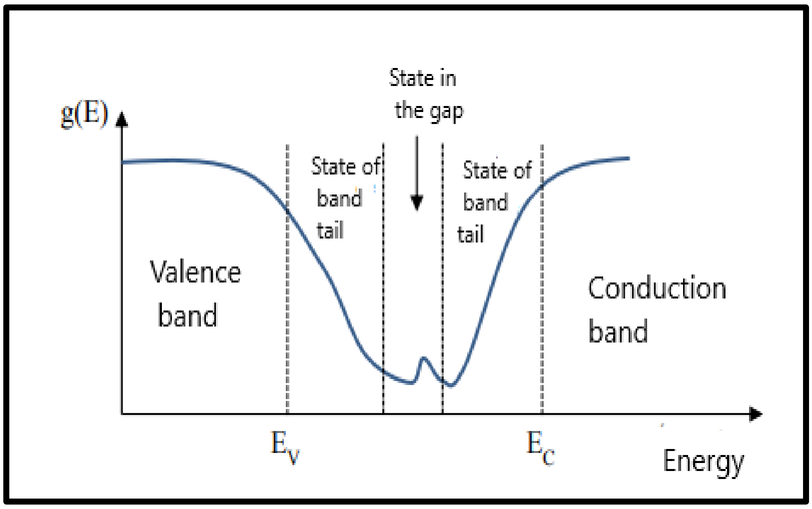

Figure II-11. Distribution function of the energy states in the bands: the tails bands [21].

'E_u' can be expressed through the following relation [22]:

$$\alpha(h\nu) = \alpha_0 \exp\left(\frac{h\nu}{E_u}\right) \quad \text{(II.13)}$$

And when we take the logarithm for the two extremes of the previous equation:

$$\ln(\alpha) = \ln(\alpha_0) + \left(\frac{h\nu}{E_u}\right) \quad \text{(II.14)}$$

From the slope ($1/E_u$) obtained from the straight-line fitting of the graph plotted between $\ln(\alpha/\alpha_0)$ on the y-axis and (hv) on the x-axis which gives the inverse of the Urbach energy we can estimate the value of E_u.

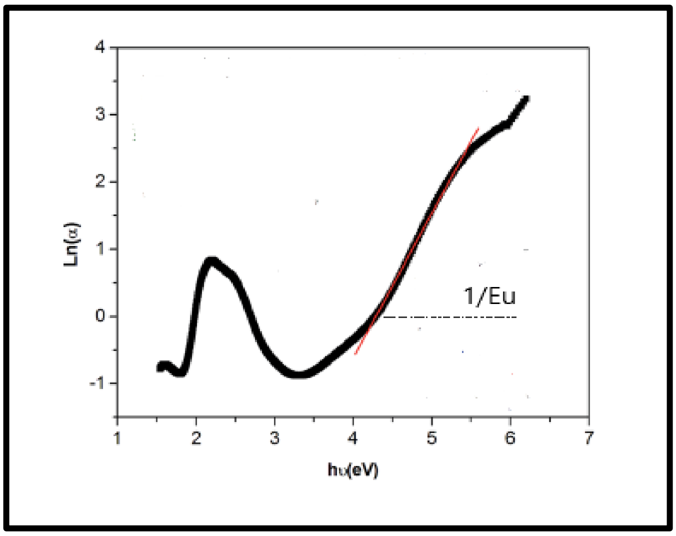

Figure II-12. Determination of Urbach energy [23].

II.2.4. Electrical properties

- **Four-point probe**

The four-point probe is a procedure used to evaluate the electrical resistivity of thick material or thin films. Two pairs of electrodes aligned, or arranged in a square are applied on the film which is deposited on an insulating substrate (generally Pyrex or glass for optical microscopes as in our case of SnO_2 thin films), the first pair creates the current **'I'**, while the second pair measures the voltage **'V'** (Figure II-13). When the probe spacing **'s'** is very greater than the thickness of the thin film **'d' (d << s)** the lateral dimensions can be considered infinite, in this case, the model can be considered as two-dimensional conduction and we use the following equation:

$$\frac{U}{I} = K\,\frac{\rho}{d} \qquad \text{(II.15)}$$

$$\rho = R_S.d \qquad \text{(II.16)} \qquad \text{and} \qquad R_S = \frac{1}{K}.\frac{U}{I} = K'.\frac{U}{I} \qquad \text{(II.17)}$$

Where:

ρ: is the electrical resistivity.

d: is the film thickness.

R_S: is the sheet resistance.

K': is a constant equal to $\frac{\pi}{\ln 2}$= 4.53 for the thin films.

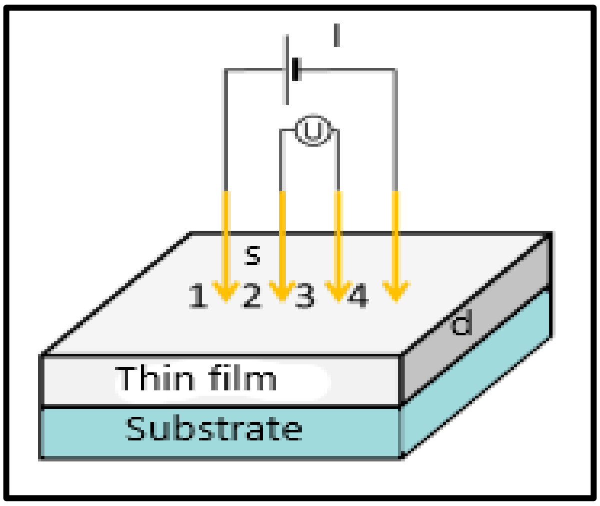

Figure II-13. Measurement of the resistivity of a thin film by the 4-point method [24].

References

[1] R. Saâd, "Elaboration et caracterisation de couches minces par spray pyrolyse et pulverisation magnetron", University of Biskra- Algeria, 2008.

[2] S. Dridi1, N. Bitri, S. Mahjoubi, F. Chaabouni, I. Ly, One-step spray of Cu_2 Ni Sn S_4 thin films as absorber materials for photovoltaic applications, J. Mater. Sci. Mater Electron. 31 (2020), 7193–7199, https://doi.org/10.1007/s10854-020-03291-0.

[3] A.X. Lu, Z.B. Ke, Z.H. Xiao, X.F. Zhang, X.Y. Li, Effect of heat-treatment condition on crystallization behavior and thermal expansion coefficient of Li_2O–ZnO–Al_2O_3–SiO_2–P_2O_5 glass–ceramics, J. Non. Cryst. Solids. 353 (2007), 2692–2697, https://doi.org/10.1016/j.jnoncrysol.2007.05.011.

[4] E. C. Ziemath, B. Z. Saggioro, J. S. Fossa, Physical properties of silicate glasses doped with SnO_2, J. Non. Cryst. Solids, 351 (2005) 3870–3878, https://doi.org/10.1016/j.jnoncrysol.2005.10.016.

[5] M. Aljerf, "Propriété Mécaniques des Verres Métalliques ; Mise en Forme et Applications", University of Grenoble-Paris, 2011.

[6] M. A. A. Masud, M. A. H. Chowdhury, "Analysing the effect of annealing temperature on the crystalline parameters of ZnO nanoparticles", University of Chittagong- Bangladesh, 2019.

[7] C. Khelifi, A. Attaf, H. Saidi, A. Yahia, M. Dahnoun, Investigation of F doped SnO_2 thin films properties deposited via ultrasonic spray technique for several applications, Surfaces and Interfaces. 15 (2019), 244–249, https://doi.org/10.1016/j.surfin.2019.04.001.

[8] A. Abdelkrim, S. Rahmane, O. Abdelouahab, N. Abdelmalek, G. Brahim, Effect of solution concentration on the structural, optical and electrical properties of SnO_2 thin films prepared by spray pyrolysis, Optik.127 (2016), 2653–2658, https://doi.org/10.1016/j.ijleo.2015.11.232.

[9] A. A. Galil, M. S.A. Hussien, I.S. Yahia, Low cost preparation technique for conductive and transparent Sb doped SnO_2 nanocrystalline thin films for solar cell applications, Superlattices Microstruct. 147 (2020), 106697, http://doi.org/ 10.1016/j.spmi.2020.106697.

[10] P. Sivakumar, H. Sharma Akkera, T. R. K. Reddy, Y. Bitla, V. Ganesh, P. M. Kumar, G. S. Reddy, M. Poloju, Effect of Ti doping on structural , optical and electrical properties of

SnO_2 transparent conducting thin films deposited by sol-gel spin coating, Opt. Mater. 113 (2021), 110845, http://doi.org/10.1016/j.optmat.2021.110845.

[11] P.V. Jithin, K. Sudheendran, K.J. Sankaran, J. Kurian, Influence of Fe-doping on the structural and photoluminescence properties and on the band-gap narrowing of SnO_2 nanoparticles, Opt. Mater. 120 (2021), 111367, http://doi.org/ 10.1016/j.optmat.2021.111367.

[12] Z. Bencharef, A. Chala, R. Messemeche, Y. Benkhetta, The physical properties of spinel cubic Co_3O_4 thin films prepared by a PSM, Main Gr. Chem. 21 (2022), 329-340, http://doi.org/ 10.3233/MGC-210090.

[13] S. Carrara, “Towards new efficient nanostructured hybrid materials for ECL applications”, University of Strasbourg-Paris, 2017.

[14] P. Birnal, “Films minces micro/nanostructures : synthèse par ALD de composites associant opales inverses de TiO_2 et nanoparticules d’or pour des applications photo catalytiques”, University of Bourgogne-Paris, 2021.

[15] H. Nadjette, “Elaboration et caractérisation des couches minces d’oxyde d’indium dopées à l’étain et au brome obtenue par spray pyrolyse ultrasonique”, University of Biskra-Algeria, 2021.

[16] S.A. Dargham, “Films piézoélectriques sans plomb par une approche sol gel et applications potentielles dans les MEMS,” University of Valenciennes- Libanaise, 2016.

[17] M. Lübke, “Nano-sized Transition Metal Oxide Negative Electrode Materials for Lithium-ion Batteries”, University College London-London, 2018.

[18] M. Radhia, “Elaboration and characterization of undoped and doped titanium dioxide thin layers by sol gel (spin coating) for photocatalytic applications”, University of Biskra-Algeria, 2020.

[19] A. Yangui, “ Etude des propriétés optiques et structurales des matériaux hybrides organiques-inorganiques à base de Plomb : émission de lumière blanche ”, University of Sfax-Tunisia, 2017.

[20] N. Kouidri, S. Rahmane, Effect of cobalt chloride concentration on structural, optical and electrical properties of Co_3O_4 thin films deposited by pneumatic spray, New Technol. Mater. 10 (2020), 56-62, http://doi.org/ 10.12816/0058152.

[21] F. Zoubian, “Couches minces d’oxynitrure de tantale déposées par pulvérisation réactive. Étude du système Ta-Ar-O_2-N_2 et caractérisation des films”, University of Blaise Pascal-Paris, 2013.

[22] A. Parida, D. Sahoo, D. Alagarasan, S. Vardhrajperumal, R. Ganesan, R. Naik, Impact on nonlinear/linear optical and structural parameters in quaternary $In_{15}Ag_{10}S_{15}Se_{60}$ thin films upon annealing at different temperatures, Ceram. Int. 48 (2022), 15380-15389, http://doi.org/10.1016/j.ceramint.2022.02.072.

[23] A. Ajmi, K. Karoui, K. Khirouni, A. B. Rhaiem, Optical and dielectric properties of Na Co PO_4 in the three phases α, β, and γ, R. Soc. Chem. 9 (2019), 14772, http://doi.org/101039/c9ra01558b.

[24] Y. Murat, “Nouvelles structures électroluminescentes organiques pour applications signalétiques et petits afficheurs”, University of Bordeaux-United State, 2017.

Chapter III:

Experimental and comparison study of pure and doped SnO_2 thin films

In this chapter, a comparative study between pure and Ca, Sr, and Ba-doped SnO_2 will be conducted. This analysis encompasses a comparison of various aspects, including structural parameters (lattice constants, volume cell, crystallite size, dislocation density, and microstrain), morphological features (surface morphology), optical characteristics (transmittance in the visible range, band gap, and Urbach energy), and electrical properties (electrical conductivity and sheet resistance) of the prepared samples.

III. 1. Structural properties

III. 1.1. XRD analysis

Figure III.1 reveals the X-ray patterns of pure and Ca, Sr, and Ba doped SnO_2 thin films with increasing weight ratios (0, 2, 4, 6, and 8 wt%). Seven peaks along (110), (101), (200), (211), (220), (310), and (301) planes are observed for Ca-SnO_2 and Ba-SnO_2, while for Sr-SnO_2 only three peaks which are: (110), (200), and (211) emerged, which confirms the polycrystalline nature of all films and the presence of tetragonal SnO_2 rutile structure according to (JCPDS card no. 41–1445). The (110) peak has the highest intensity for all samples, these results are in line with other research [1–6]. Ba-SnO_2 indicates patterns with higher intensities than other patterns. The 6 wt % of Ba doped SnO_2 reported the appearance of other peaks which are (200) and (211). In contrast, Sr-SnO_2 having the lowest intensities with the increase of (110) peak's intensity for low weight ratio (2 wt %) but in the higher weight ratio (8 wt%) it has poor crystallization. So, we can deduce that the incorporation of strontium with high weight ratios leads the deterioration of the crystallinity these results are in agreement with other studies [7]. Moreover, it is noticed that the intensity of (110) peak increase with the calcium's weight ratio.

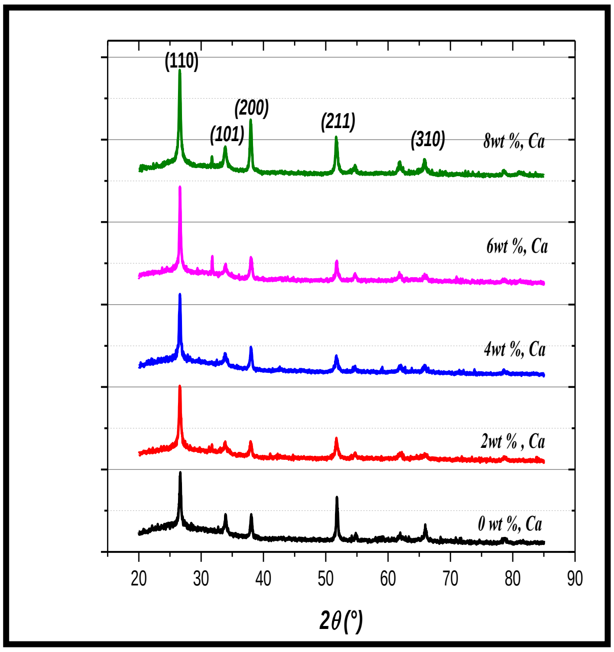

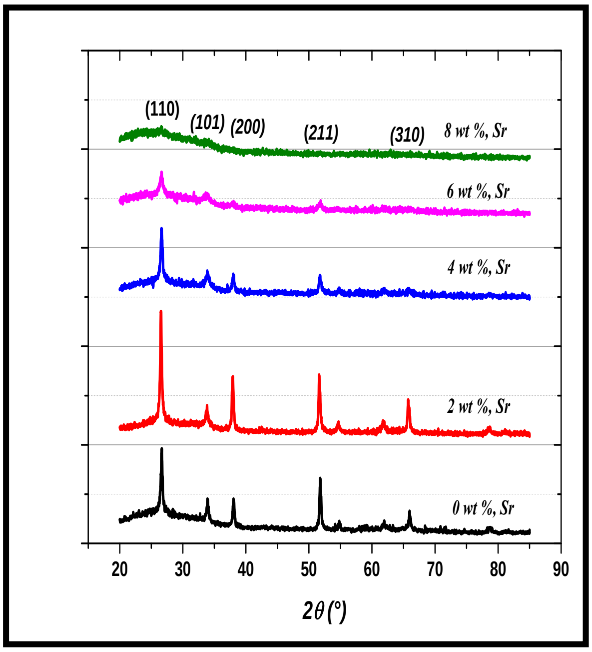

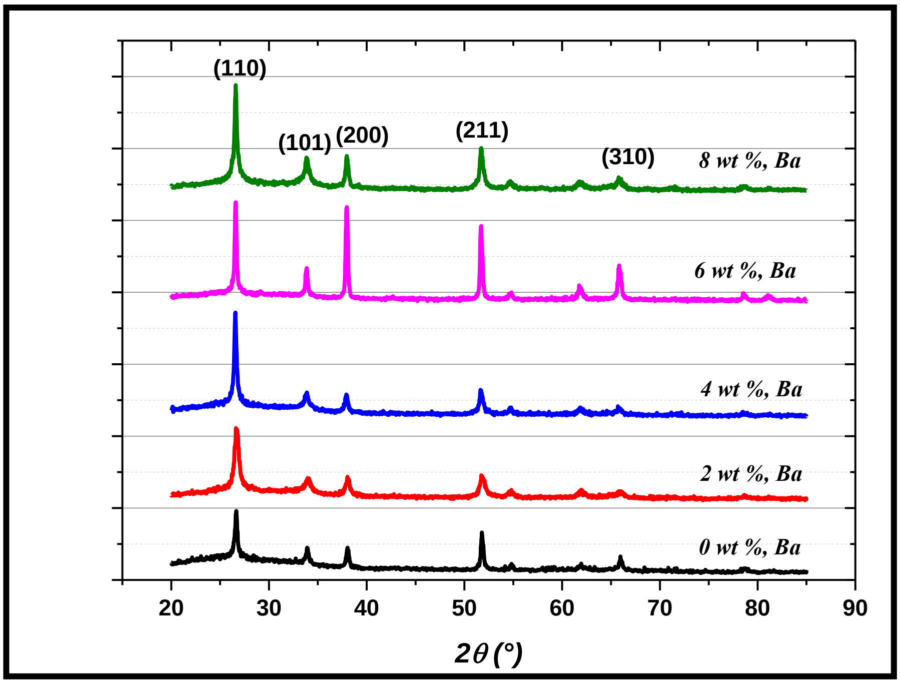

Figure.III.1. XRD patterns of pure and Ca, Sr, Ba-doped SnO_2 thin films.

III. 1.2. Texture coefficient (TC) and lattice parameters

In the following, the TC value for the (110) peak for all the samples was calculated from the X-ray data by applying the widely used formula [8]. We can note that if the value of TC (hkl) is lower than one it confirms the polycrystalline nature of our prepared films, whereas if it is equal to or higher than one this demonstrates that the crystals grow in this direction [9].

For 'Ca' doped SnO_2, we notice that it increases with the weight ratio increasing, this increase is directly proportional to the increase in the crystalline size 'D'. Sr doped SnO_2 decreased the TC value as shown in Figure III.2. Moreover, for Ba-SnO_2 films, the TC reaches the highest value in 4 wt % concentration.

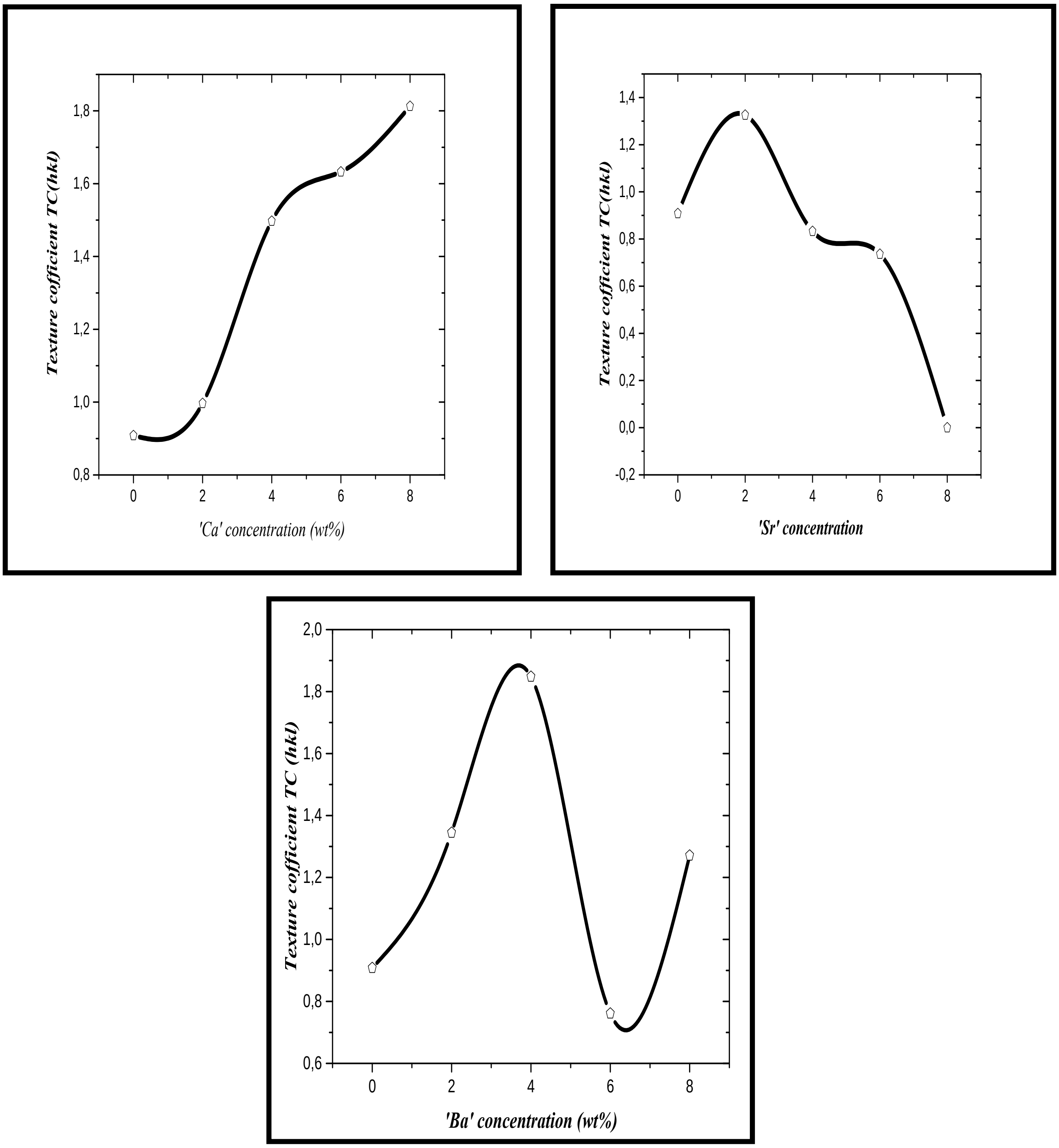

Figure.III.2. Variation of TC (110) of pure and Ca, Sr, Ba-doped SnO_2 thin films.

The variation of lattice parameters (*a*, *b*, and *c*), and cell volume '*v*' of undoped, and doped SnO_2 were represented in Table III.1, we observe that the lattice constants and cell volume increase with the increases of the dopant concentration (when we fix the dopant element) for all the dopant elements. From Figure III.3 we can observe that the cell volume decreases with the increase of the ionic radii at low doped concentrations (2 wt %) and it is always higher than the cell volume of pure SnO_2, for hight concentration (8 wt %) the cell volume increase with the increase of the ionic radii, this increase may be due to the high ionic radii of the dopant elements compared to the radii of Sn^{4+}, or it can be attributed to the oxygen vacancies, MD. Ariful Islam et al reported that the substitution of divalent/trivalent ions in the SnO_2 lattice increases the number of oxygen vacancies [10], this last leads to a tensile compression because of coulombic repulsion between tin ions [11].

Table III.1: Lattice constants '*a*', '*c*', and cell volume '*v*' of pure and doped SnO_2 films.

		Ca-SnO_2	**Sr-SnO_2**	**Ba-SnO_2**
0 wt %	***a* (°A)**	4.733	4.733	4.733
	***c* (°A)**	3.181	3.181	3.181
	***v* (°A)^3**	71.279	71.279	71.279
2 wt %	***a* (°A)**	4.738	4.737	4.736
	***c* (°A)**	3.184	3.183	3.182
	***v* (°A)^3**	71.492	71.437	71.392
4 wt %	***a* (°A)**	4.739	4.738	4.740
	***c* (°A)**	3.185	3.184	3.185
	***v* (°A)^3**	71.531	71.494	71.596
6 wt %	***a* (°A)**	4.740	4.750	4.750
	***c* (°A)**	3.185	3.192	3.192
	***v* (°A)^3**	71.582	72.064	72.029
8 wt %	***a* (°A)**	4.749	/	4.750
	***c* (°A)**	3.191	/	3.192
	***v* (°A)^3**	71.991	/	72.064

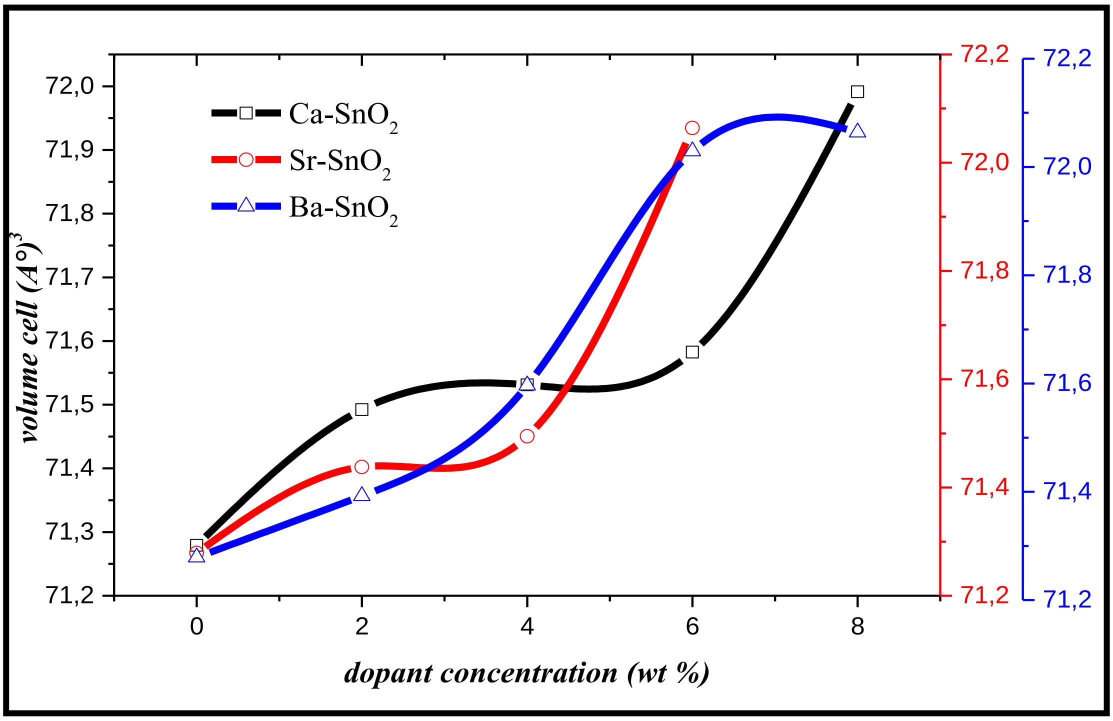

Figure.III.3. Cell volume variation of pure and Ca, Sr, Ba-doped SnO_2 thin films.

III. 1.3. Crystallite size (D), dislocation density (δ), and micro strain (ε)

The crystallite size of all the samples is calculated using the Debye-Scherrer formula [12,13]. Firstly, for Ca-doped SnO_2, it increases with the increase of calcium content and it is always higher than the 'D' of pure SnO_2, which indicates the improvement of the crystalline quality of SnO_2 films because of the narrow in grain boundaries [14].

Secondly, Sr-SnO_2 films show that the highest value of 'D' is at 2 wt % (24.257 nm), while in the rest two concentrations of strontium which are 4, and 6 wt % the films' crystallite size decreases and it showing the assimilation of defects [15].

Finally, For Ba-SnO_2 it is suggesting that the crystal size changes are variable, the maximum value is at 4 wt% (32.934 nm) similar to strontium-doped SnO_2, however, we find that the crystal size values fall to their lowest levels compared to pure tin dioxide thin films at high barium concentrations (6 wt %).

We can conclude that the crystallite size is rich to their maximum level at medium concentrations, furthermore, the microstrain and dislocation density are always inversely proportional to the crystal size, as Figure.III.4 shows.

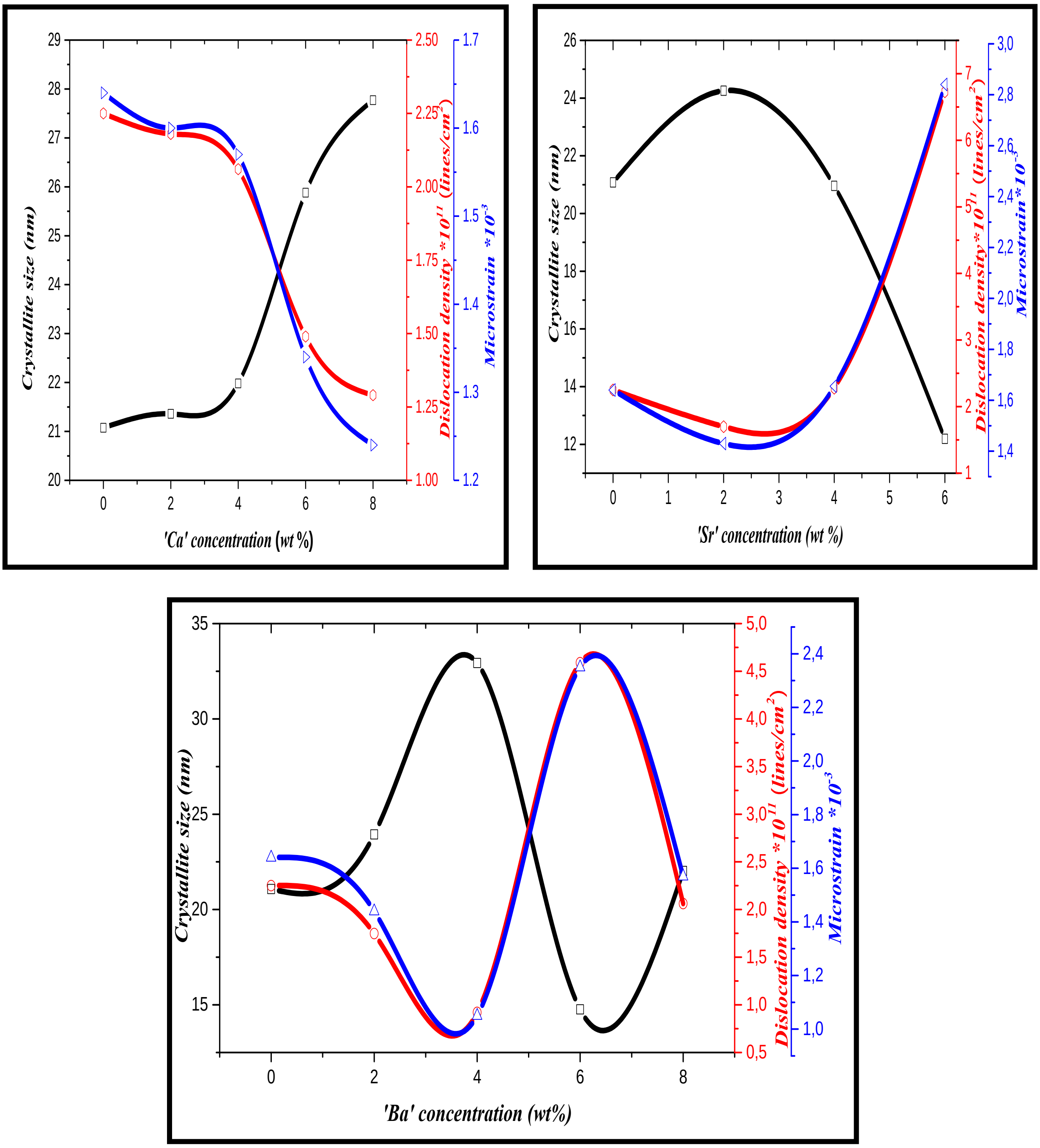

Figure.III.4. Crystallite size microstrain, and dislocation density of pure and doped SnO_2 thin films.

Table III.2: Crystallite size ‘D’, dislocation density ‘δ’, and microstrain ‘ε’ of pure and doped SnO_2 thin films.

		Ca-SnO_2	**Sr-SnO_2**	**Ba-SnO_2**
0 wt %	***D (nm)***	21.07	21.07	21.07
	$\delta*10^{11}$(lines/cm^2)	2.25	2.25	2.25
	$\varepsilon*10^{-3}$	1.64	1.64	1.64
2 wt %	***D (nm)***	21.36	24.25	23.94
	$\delta*10^{11}$(lines/cm^2)	2.18	1.69	1.74
	$\varepsilon*10^{-3}$	1.6	1.43	1.44
4 wt %	***D (nm)***	21.98	20.95	32.93
	$\delta*10^{11}$(lines/cm^2)	2.06	2.27	0.92
	$\varepsilon*10^{-3}$	1.57	1.65	1.05
6 wt %	***D (nm)***	25.88	12.19	14.76
	$\delta*10^{11}$(lines/cm^2)	1.49	6.72	4.58
	$\varepsilon*10^{-3}$	1.34	2.84	2.35
8 wt %	***D (nm)***	27.77	/	22.02
	$\delta*10^{11}$(lines/cm^2)	1.29	/	2.06
	$\varepsilon*10^{-3}$	1.24	/	1.57

III. 2. Morphological properties

The morphological study of the samples’ surface was made by scanning electron microscopy (SEM) type Prisma E SEM of PTAPC Biskra CRAPC and VEGA3 TESCAN of LPCMA in Biskra University using 5.000 kx SEM mag. The influence of each dopant on the morphology of SnO_2 films was discussed in the paragraphs that follow. Also, there is an EDS composition analysis of the prepared films to confirm the presence of dopants which are Ca, Sr, and Ba, where their weight quantity increases with the increase of dopant concentration this validates the experiment's correct path.

III. 2.1. Ca-doped SnO_2

Figure III.5 reveals images of scanning electron microscopy for Ca-doped SnO_2, it was seen that all the films had homogenous, dense, and continuous surfaces just 8 wt % of Ca-doped SnO_2 it was seen that its surface was not smooth, also the grains' shape was different in high and low concentrations of calcium; at low concentrations, we can see that there are small fibers or sticks (we can say also needles) [16], also at 2 wt % of Ca-doped SnO_2, we can notice the growth of dark and light islands, the size of these sticks increases with the increase of Ca content in tin dioxide until it reaches 6 wt %; at high concentration (8 wt%) the grains' chape changed like flowers [17,18] with a big size. So, upon increasing the concentration of Ca doping, the grains' size increase which corroborates the XRD findings, where the crystallite size 'D' increase with the increase of Ca doping.

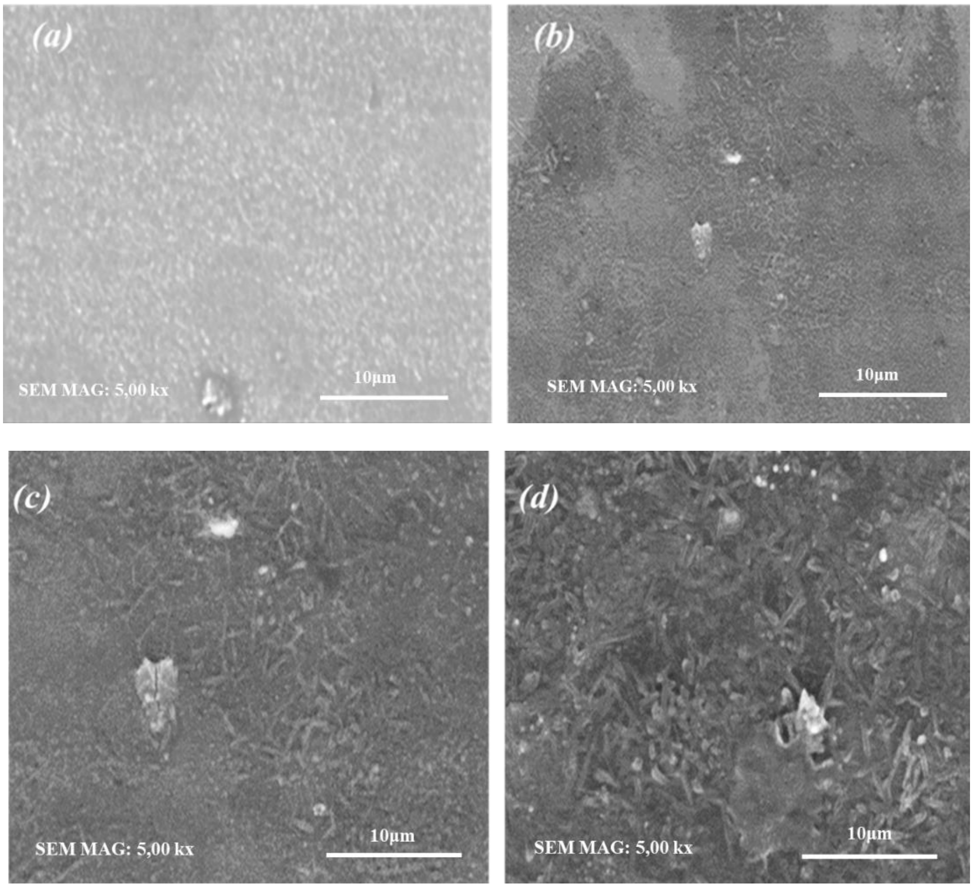

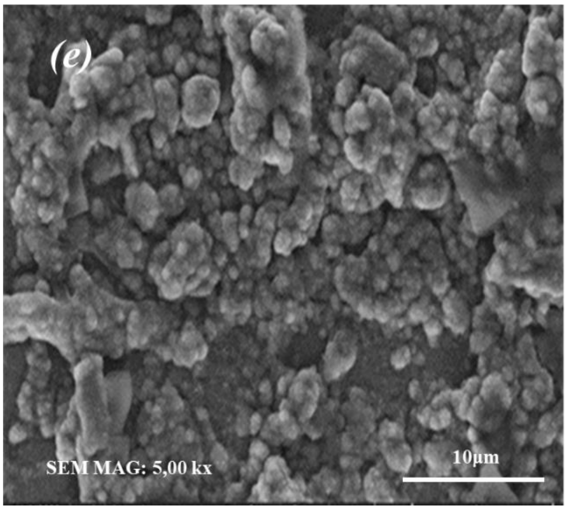

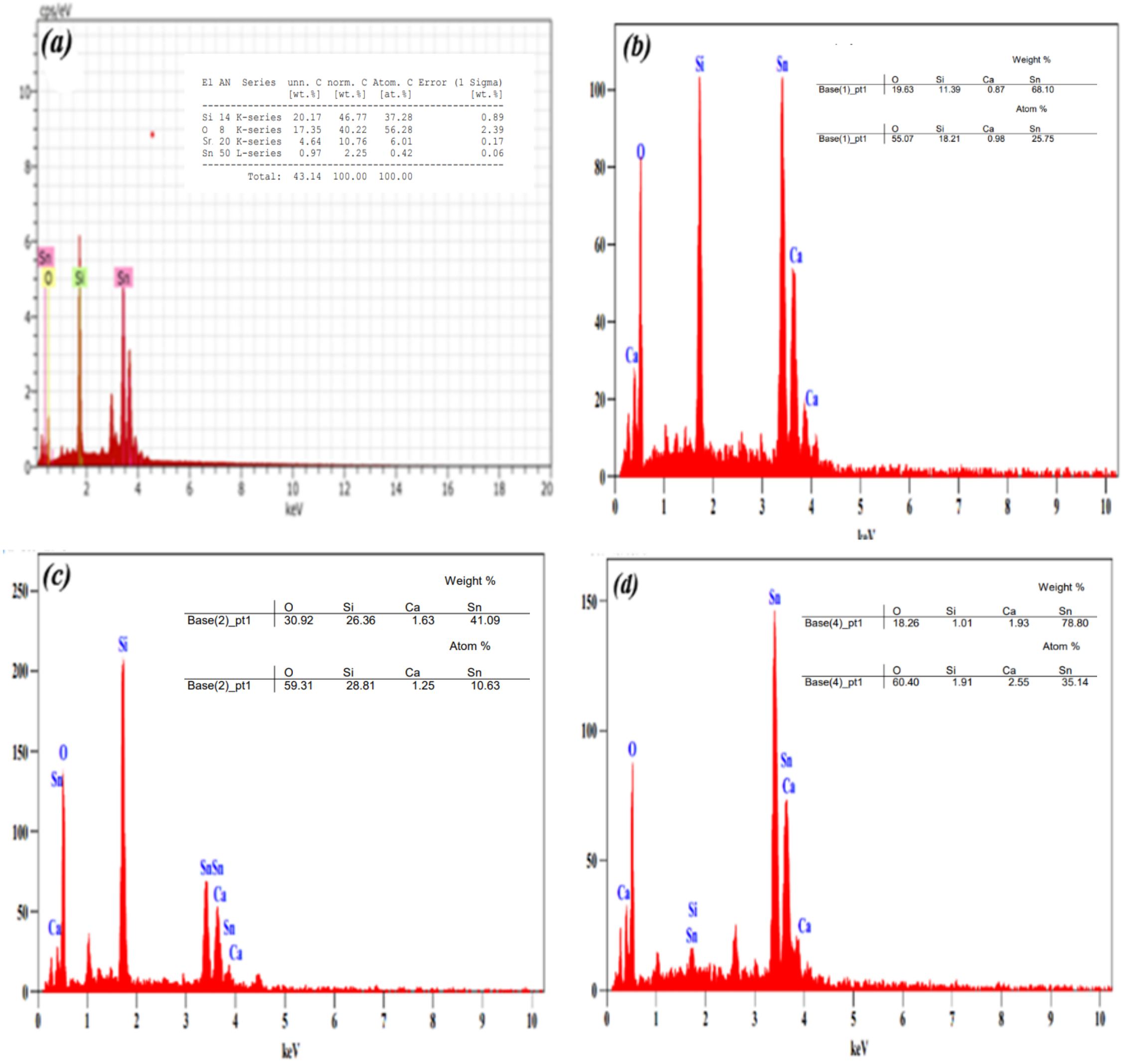

```
El AN  Series  unn. C norm. C Atom. C Error (1 Sigma)
               [wt.%]  [wt.%]  [at.%]           [wt.%]
-----------------------------------------------------
Si 14 K-series  20.17   46.77   37.28             0.89
O   8  K-series 17.35   40.22   56.28             2.39
Sr 20 K-series   4.64   10.76    6.01             0.17
Sn 50 L-series   0.97    2.25    0.42             0.06
-----------------------------------------------------
        Total:  43.14  100.00  100.00
```

Weight %

	O	Si	Ca	Sn
Base(1)_pt1	19.63	11.39	0.87	68.10

Atom %

	O	Si	Ca	Sn
Base(1)_pt1	55.07	18.21	0.98	25.75

Weight %

	O	Si	Ca	Sn
Base(2)_pt1	30.92	26.36	1.63	41.09

Atom %

	O	Si	Ca	Sn
Base(2)_pt1	59.31	28.81	1.25	10.63

Weight %

	O	Si	Ca	Sn
Base(4)_pt1	18.26	1.01	1.93	78.80

Atom %

	O	Si	Ca	Sn
Base(4)_pt1	60.40	1.91	2.55	35.14

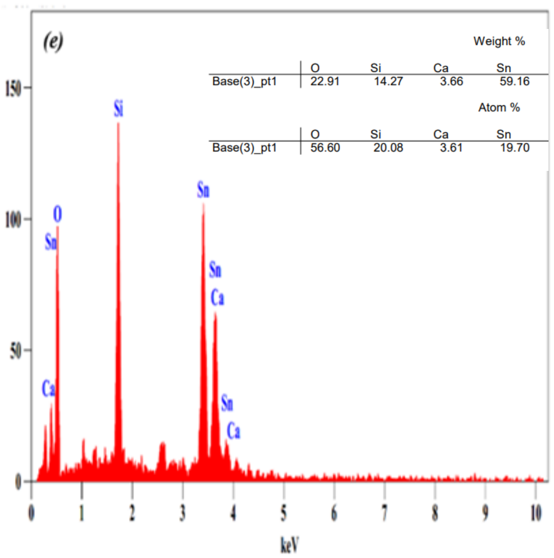

Weight %

	O	Si	Ca	Sn
Base(3)_pt1	22.91	14.27	3.66	59.16

Atom %

	O	Si	Ca	Sn
Base(3)_pt1	56.60	20.08	3.61	19.70

Figure III.5. SnO_2 film micrographs and EDS analysis at various calcium doping levels *(a)* 0 wt %, *(b)* 2 wt %, *(c)* 4wt%, *(d)* 6 wt %, and *(e)* 8 wt %.

III. 2.2. Sr-doped SnO_2

Figure III.6 shows that there is no more difference in the surface morphology of the samples, it is obvious that the three samples have a smooth dense and homogenous surface which confirms the excellent quality of crystallization and their adherence with the substrates [19]. So, a few grains appear at concentration 2 wt % compared to 0 wt % of Sr, while for 4 and 6 wt % the grain are present, but they are very small in size, it almost disappears; in general, the surface morphology of tin dioxide did not improve by the addition of strontium.

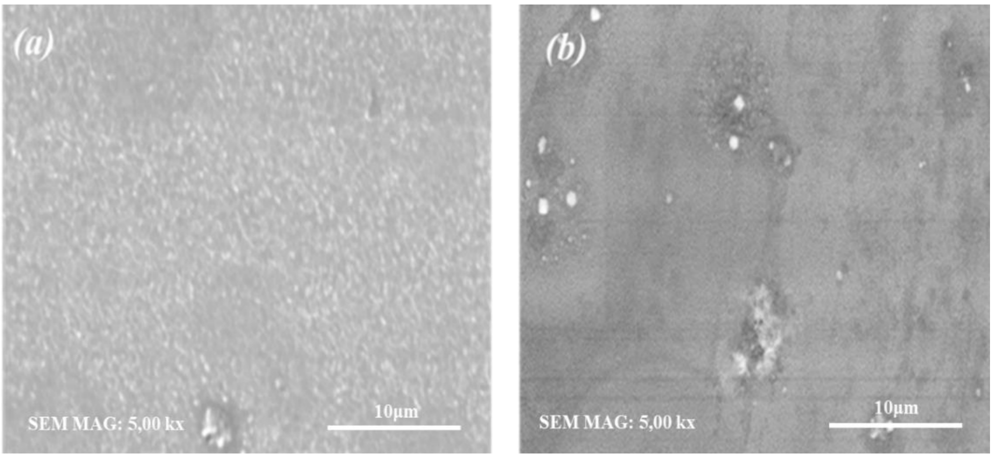

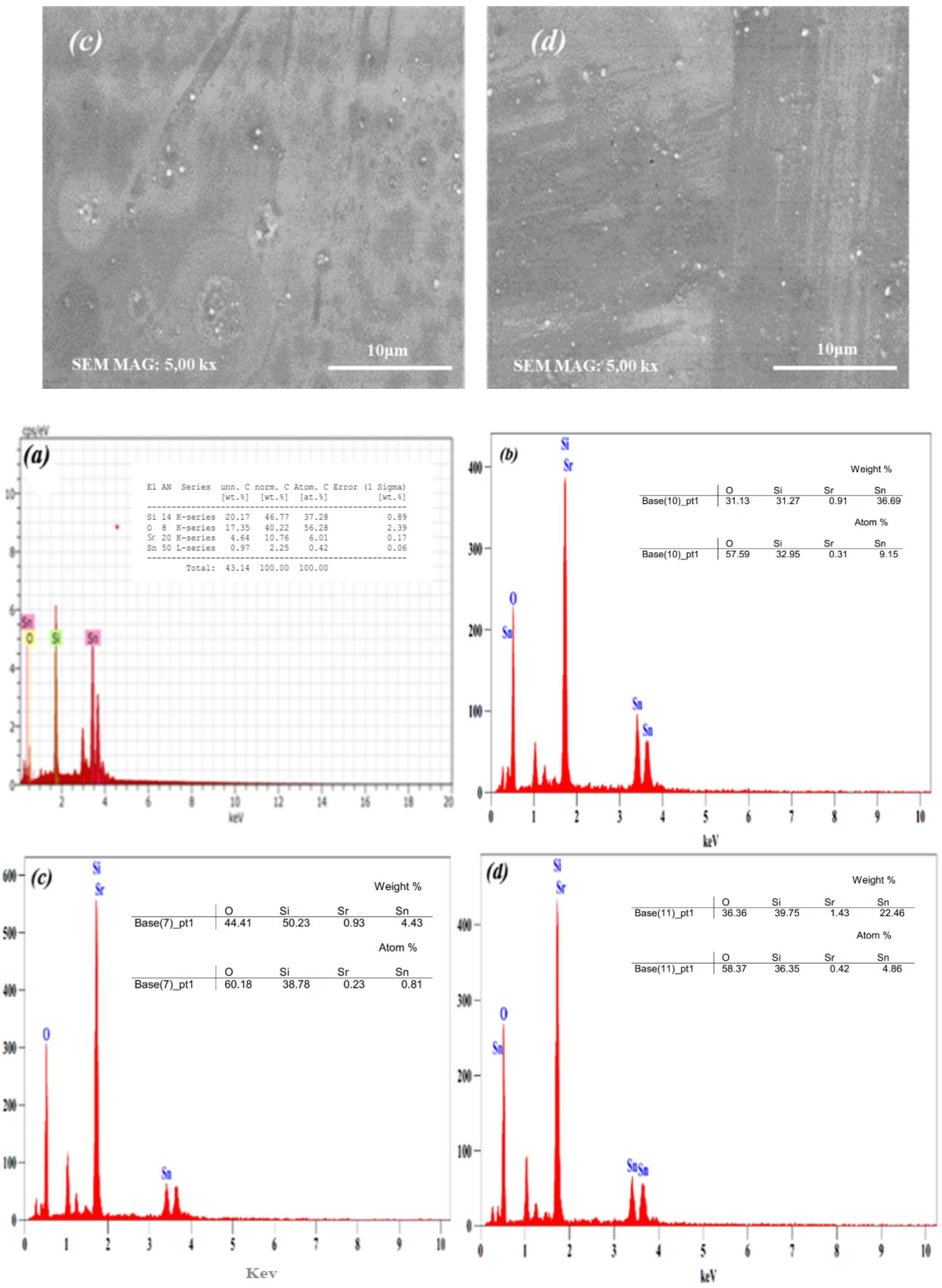

```
El AN  Series   unn. C norm. C Atom. C Error (1 Sigma)
                 [wt.%]  [wt.%]  [at.%]          [wt.%]
-----------------------------------------------------
Si 14 K-series  20.17   46.77   37.28            0.89
O  8  K-series  17.35   40.22   56.28            2.39
Sr 20 K-series   4.64   10.76    6.01            0.17
Sn 50 L-series   0.97    2.25    0.42            0.06
-----------------------------------------------------
        Total:  43.14  100.00  100.00
```

Weight %

	O	Si	Sr	Sn
Base(10)_pt1	31.13	31.27	0.91	36.69

Atom %

	O	Si	Sr	Sn
Base(10)_pt1	57.59	32.95	0.31	9.15

Weight %

	O	Si	Sr	Sn
Base(7)_pt1	44.41	50.23	0.93	4.43

Atom %

	O	Si	Sr	Sn
Base(7)_pt1	60.18	38.78	0.23	0.81

Weight %

	O	Si	Sr	Sn
Base(11)_pt1	36.36	39.75	1.43	22.46

Atom %

	O	Si	Sr	Sn
Base(11)_pt1	58.37	36.35	0.42	4.86

Figure III.6. SnO_2 film micrographs and EDS analysis at various strontium doping levels *(a)* 0 wt %, *(b)* 2 wt %, *(c)* 4wt%, and *(d)* 6 wt %.

III. 2. 3. Ba-doped SnO_2

The scanning electron microscopy (SEM) images of Ba-doped SnO_2 samples with various levels of doping concentrations are shown in Figure III.7 (a) through (e). The micrographs exhibit a smooth, dense, and continuous surface morphology without any voids. The size and shape of the grains on the surface of the Ba-doped SnO_2 samples are somewhat different from those on the surface of the undoped SnO_2 [10].

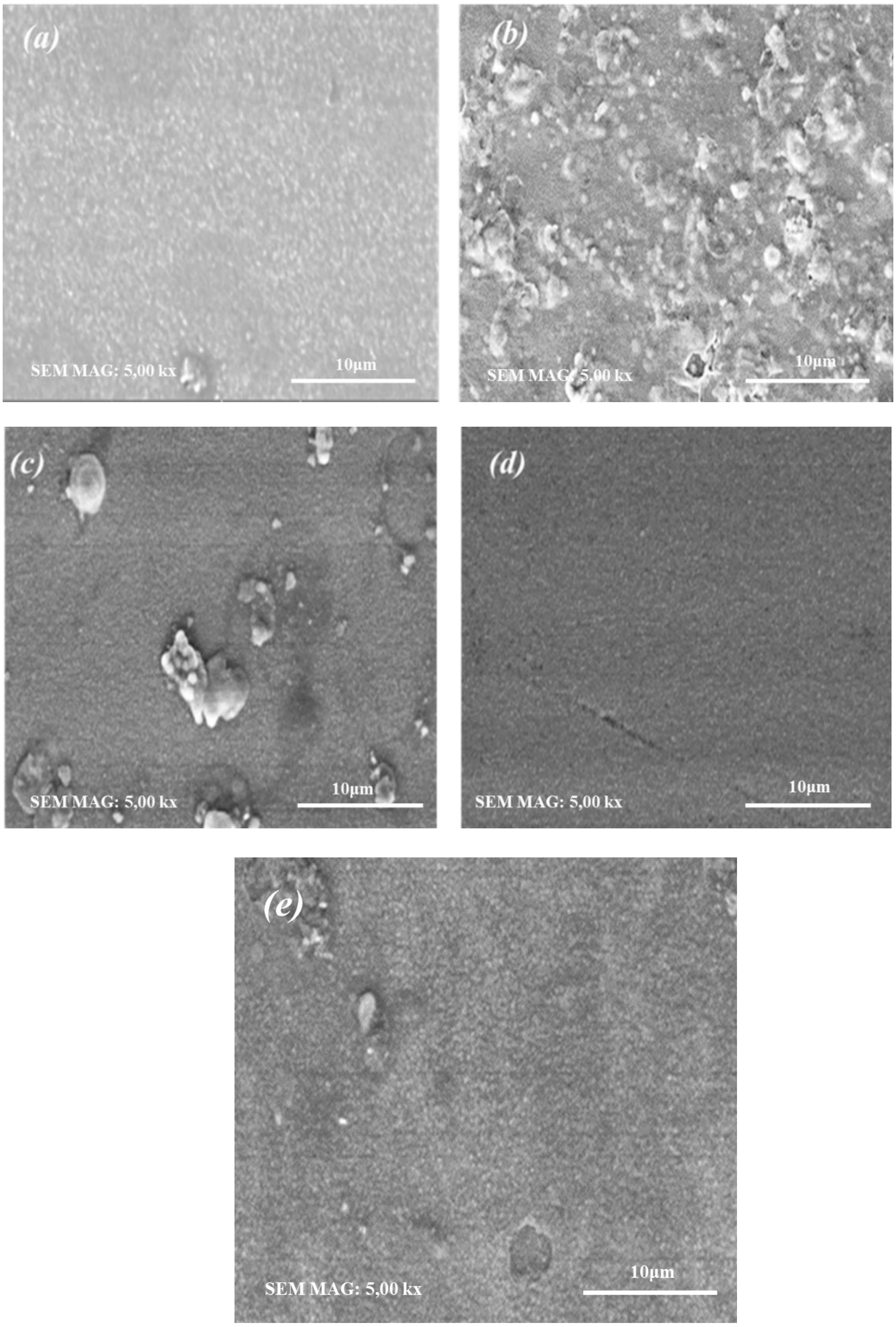

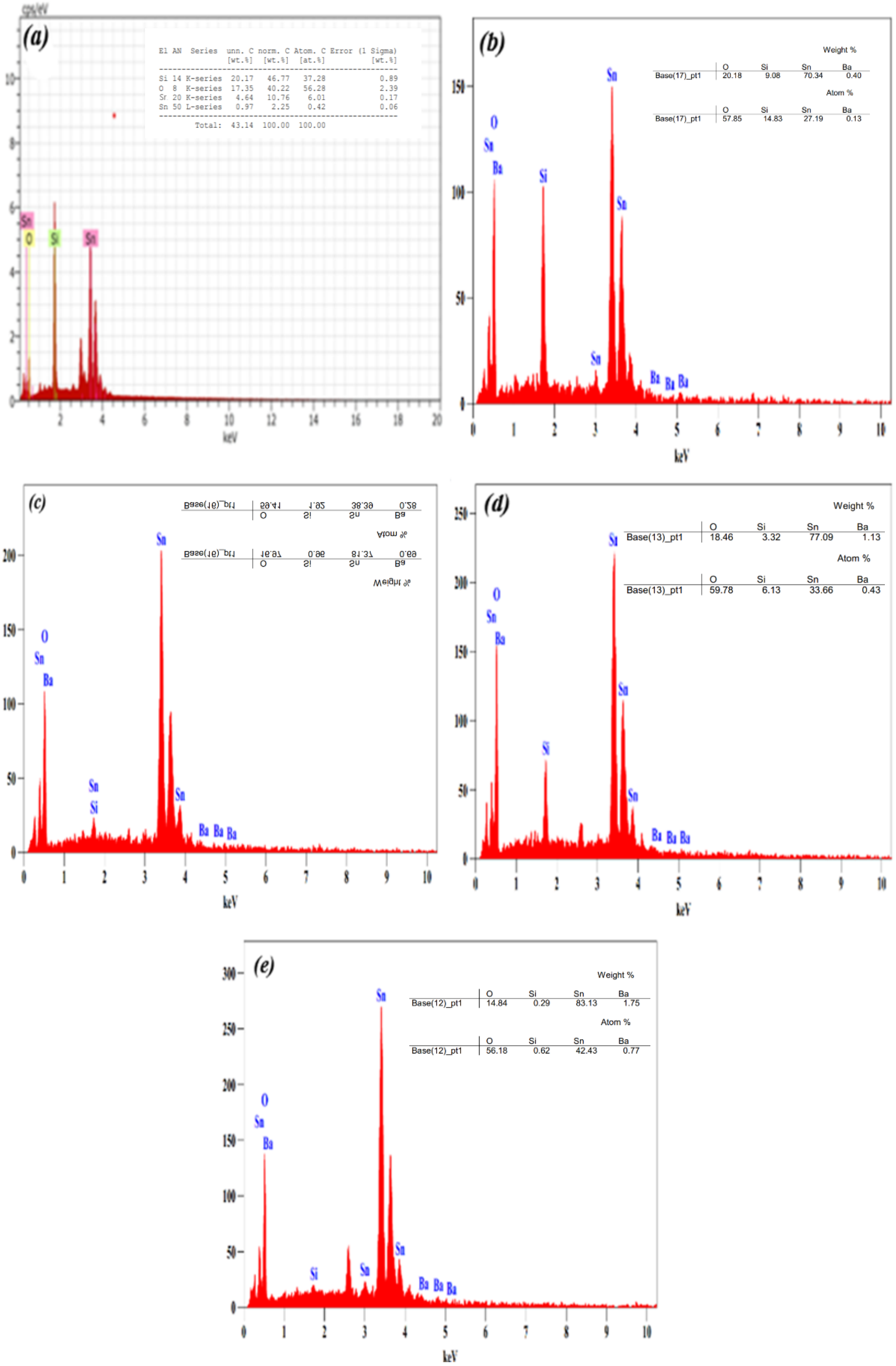

(a)

```
El AN  Series   unn. C norm. C Atom. C Error (1 Sigma)
                [wt.%]  [wt.%]  [at.%]          [wt.%]
------------------------------------------------------
Si 14 K-series  20.17   46.77   37.28             0.89
O   8 K-series  17.35   40.22   56.28             2.39
Sr 20 K-series   4.64   10.76    6.01             0.17
Sn 50 L-series   0.97    2.25    0.42             0.06
------------------------------------------------------
       Total:   43.14  100.00  100.00
```

(b)

Weight %

	O	Si	Sn	Ba
Base(17)_pt1	20.18	9.08	70.34	0.40

Atom %

	O	Si	Sn	Ba
Base(17)_pt1	57.85	14.83	27.19	0.13

(c)

Weight %

	O	Si	Sn	Ba
Base(16)_pt1	16.97	0.96	81.37	0.69

Atom %

	O	Si	Sn	Ba
Base(16)_pt1	59.41	1.92	38.39	0.28

(d)

Weight %

	O	Si	Sn	Ba
Base(13)_pt1	18.46	3.32	77.09	1.13

Atom %

	O	Si	Sn	Ba
Base(13)_pt1	59.78	6.13	33.66	0.43

(e)

Weight %

	O	Si	Sn	Ba
Base(12)_pt1	14.84	0.29	83.13	1.75

Atom %

	O	Si	Sn	Ba
Base(12)_pt1	56.18	0.62	42.43	0.77

Figure III.7. SnO_2 film micrographs and EDS analysis at various barium doping levels *(a)* 0 wt %, *(b)* 2 wt %, *(c)* 4wt%, *(d)* 6 wt %, and *(e)* 8 wt %.

Table III.3: EDS composition analysis of pure and doped SnO_2 in weight ratio.

	Ca-SnO_2	Sr-SnO_2	Ba-SnO_2
2 wt %	0.87	0.91	0.40
4 wt %	1.63	0.93	0.69
6 wt %	1.93	1.43	1.13
8 wt %	3.66	/	1.75

III. 3. Optical properties

III. 3.1. Optical transmittance

Figure III.8 displays the transmittance spectra of pure and Ca, Sr, and Ba-doped SnO_2 thin films at various molar concentrations for each of the three dopant elements, UV-vis spectrophotometer was used in the wavelength region 300 to 1600 nm.

The addition of calcium had a positive effect on the optical properties of tin dioxide, it is evident that the transmittance increases with the increase of calcium content in SnO_2 in the visible region (approximatively at λ=700 nm), this increase can be attributed to the improvement in crystallinity which leads to a decrease in optical scattering and defects as a result, the absorption decreases while the transmittance increases [20], and these confirm the XRD results which is clear in Figure III.4 (the crystallite size increase with the increase of calcium concentration so the grain boundaries decrease which is a type of defects).

For Sr-doped SnO_2 it is clearly shown that the transmittance improved along all the visible regions for all the samples of Sr-doped SnO_2 with different concentrations just for 6 wt % of 'Sr' the transmittance decreased slightly compared to pure SnO_2, we can observe the sample of 2 wt % of 'Sr' has the highest transmittance reached to 97% at 700 nm, while for 8 wt % of 'Sr' the transmittance variation represented as a line maybe because it was poor crystallized.

Finally, for Ba-doped SnO_2 the transmittance decreased with the increase of barium concentration, it reached 38% at 700 nm for 8 wt % of 'Ba', This decrease can be attributed to the presence of dopant atoms through grain boundaries which causes a decrease in the crystallinity growth [21].

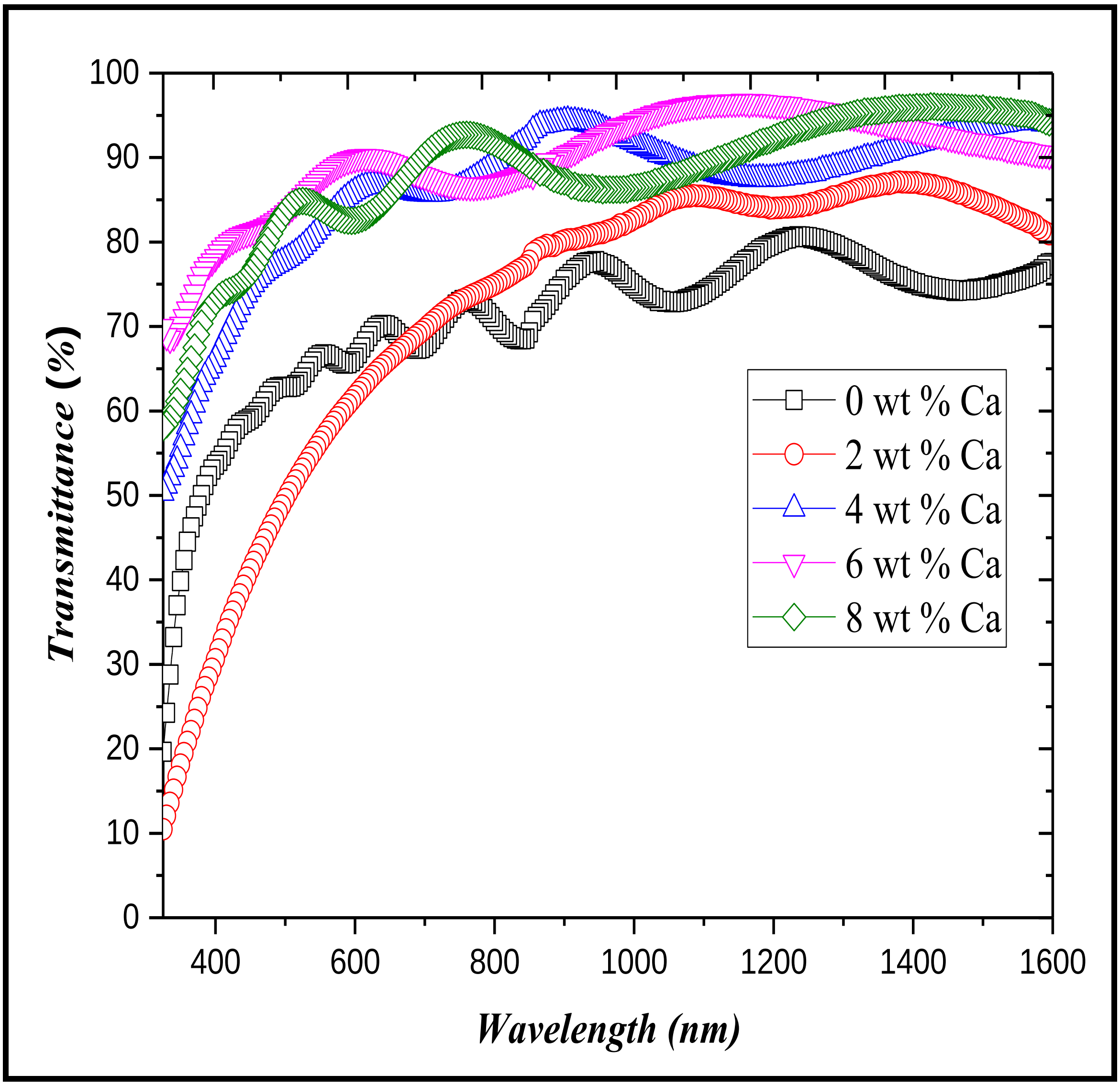
Transmittance (%)
Wavelength (nm)
0
10
20
30
40
50
60
70
80
90
100
400
600
800
1000
1200
1400
1600
0 wt % Ca
2 wt % Ca
4 wt % Ca
6 wt % Ca
8 wt % Ca

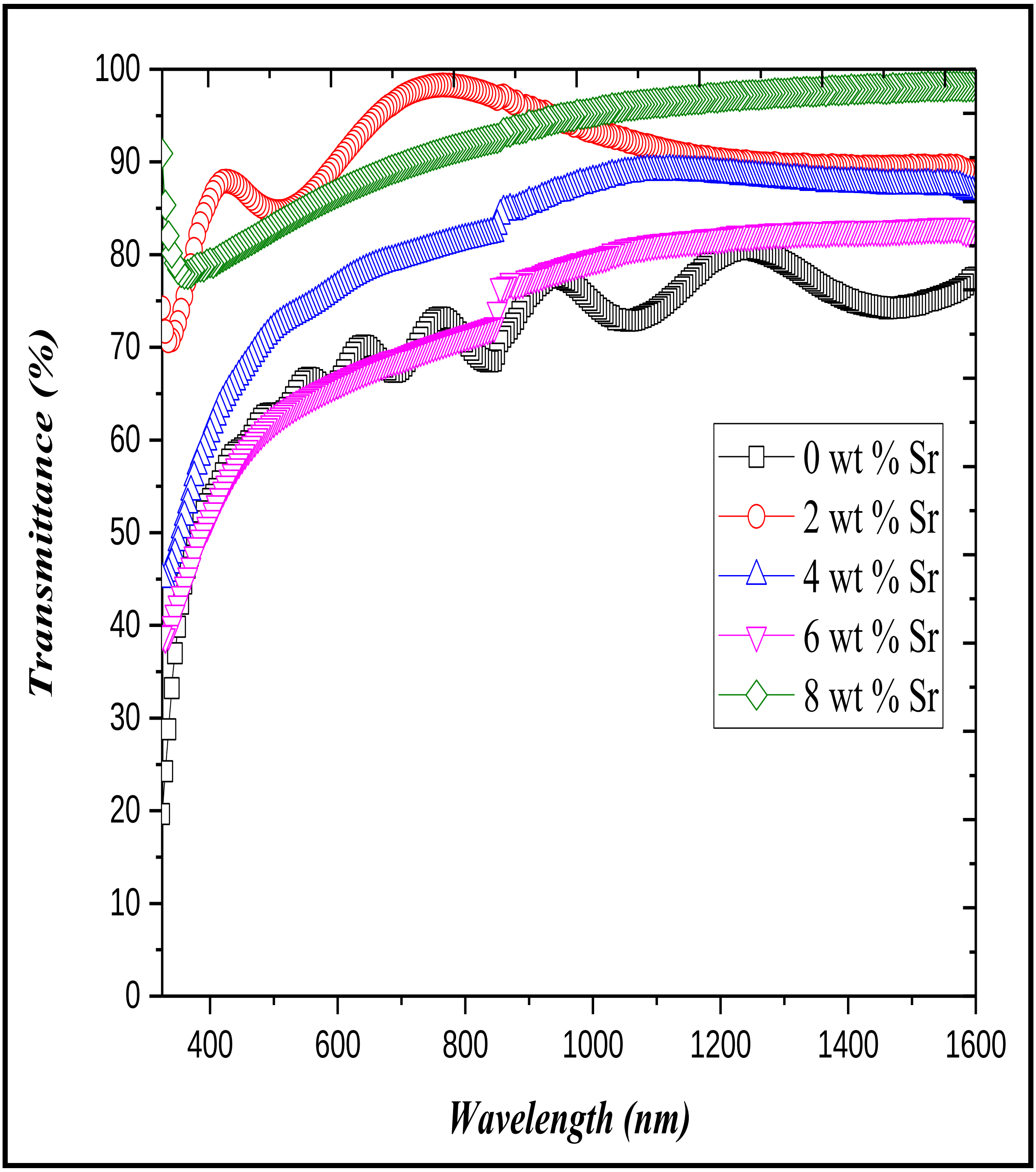
Transmittance (%)
Wavelength (nm)
0
10
20
30
40
50
60
70
80
90
100
400
600
800
1000
1200
1400
1600
0 wt % Sr
2 wt % Sr
4 wt % Sr
6 wt % Sr
8 wt % Sr

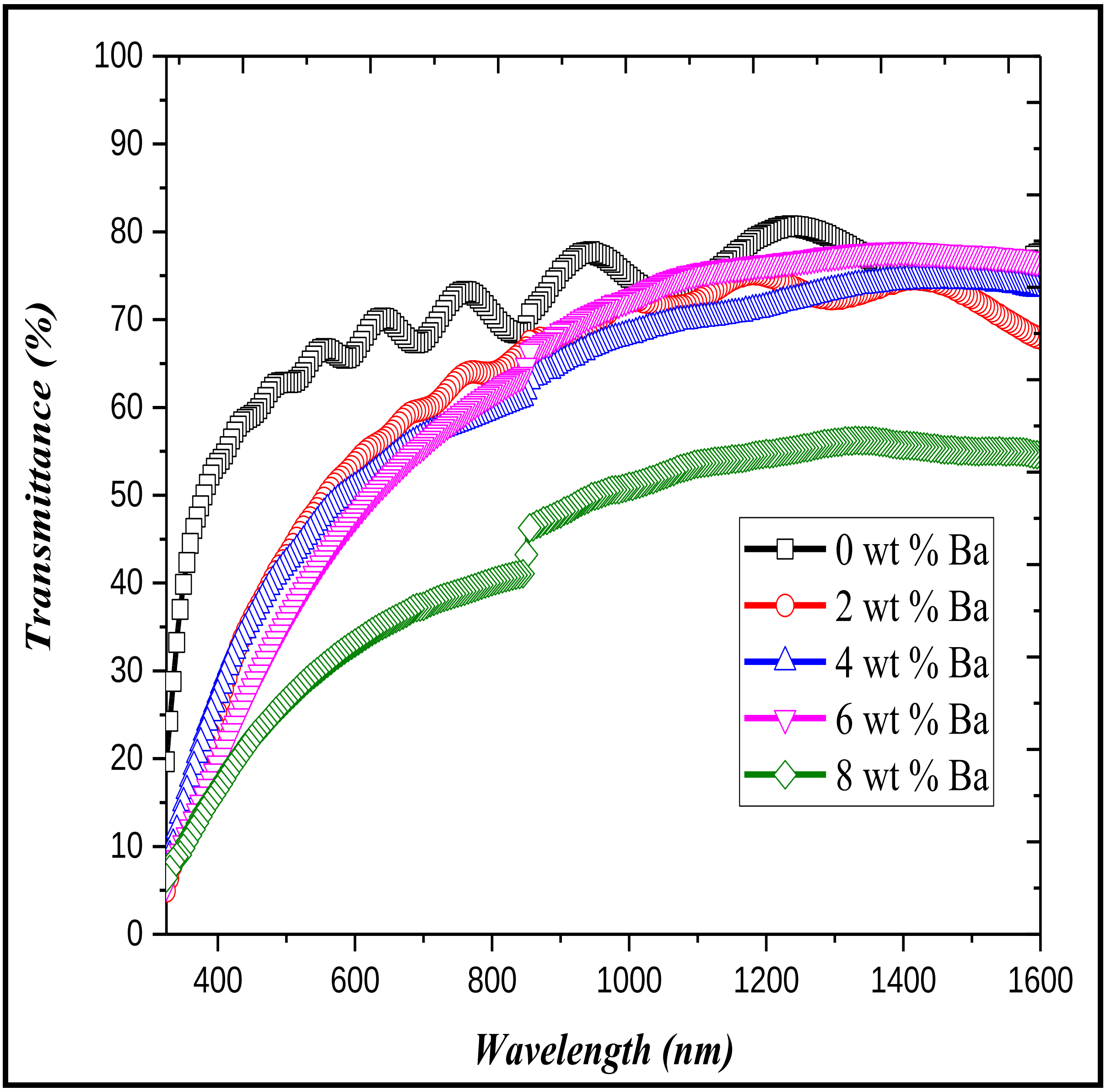

Figure III.8. Optical transmission spectra of the undoped and Ca, Sr, and Ba-doped SnO_2 thin films.

III. 3.2. Band gap (E_g) and Urbach energy (E_u)

We evaluated the optical band gap E_g and Urbach energy E_u of our films from the transmittance spectra applying the methods that were explained in the previous chapter.

The value of E_g was estimated by plotting $(\alpha h \upsilon)^2$ in terms of $(h \upsilon)$ while E_u was calculated from the inverse of the slope of the linear curve between ln (α) and $(h \upsilon)$. Depending Figure III.9 (*a*) we can notice that the band gap value increase in the first time for 2 wt % of Ca doped SnO_2 then it was decrease with the increasing of calcium weight ratio for the other samples. However, Ca-SnO_2 (8wt %) sample has the lowest value of 2.86 eV but Ca-SnO_2 (2 wt %) has the highest E_g which equal to 3.69 eV. Urbach energy which illustrate the disorder in the film is inversely proportional to the band gap energy as it is showed in Table III.4.

For Sr-SnO_2 series, it is observed that the band gap decreases slightly from 3.57 eV for the pure tin dioxide film to 2.94 eV for 2 wt % Sr-SnO_2, then it increases rapidly to 3.88 eV and 3.97 eV for 4 and 6 wt % of Sr respectively. For the disorder (E_u) there is always an inverse proportional to the E_g as its clear in Figure III.9 (*b*).

Figure III.9 (*c*) shows an increase in both the band gap and Urbach energy unusually in the small Ba concentration (2 wt %) the same variance reported in other studies which declare the preparation of ZnO thin films by magnetron sputtering system [22,23], the value of E_g continues to increase until 4 wt % concentration of barium to reach the peak then it decreases to small values but they are always higher than the E_g of pure SnO_2. From 4 wt % of Ba to 8 wt % there is an inverse proportional between E_g and E_u return.

The increase in the band gap in all the curves can be explained by Burstein-Moss effect which is related to the increase in carrier concentration due to dopant atoms which push Fermi level inside the conduction band [19,24], while the decrease is due to the decrease in the crystallite size which leads to an increase in the grain boundaries and deterioration of the crystal structure due to increase in the crystal defects which spreads in form of band tail inside the band gap that leading to its narrowing. Table III.4 Summarizes the changes in the band gap and Urbach energy.

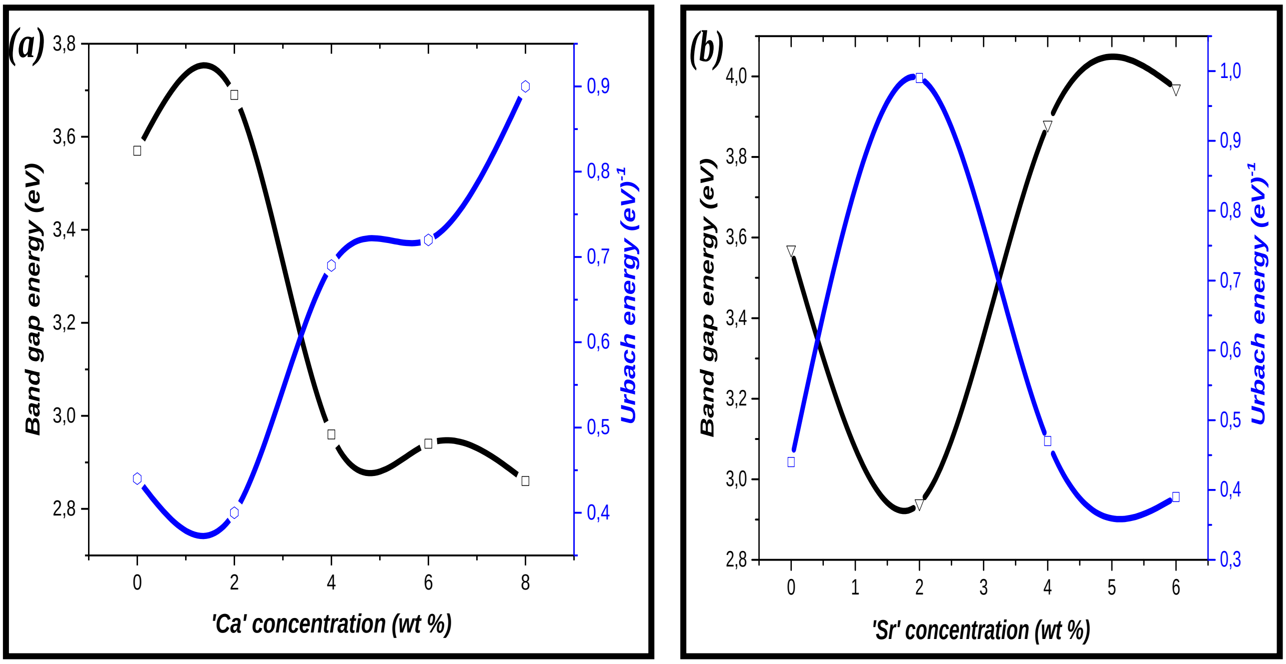

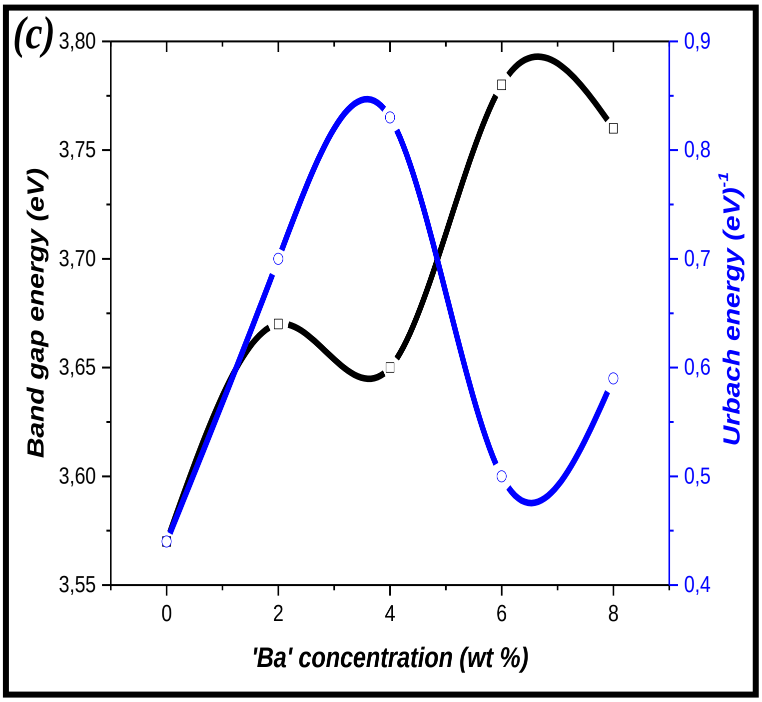

Figure III.9. Band gap energy and Urbach energy variations of: (*a*) Ca-SnO_2, (*b*) Sr-SnO_2, and (*c*) Ba-SnO_2 films.

Table III.4: Band gap energy 'E_g' Urbach energy 'E_u' of pure and doped SnO_2 thin films.

		Ca-SnO_2	**Sr-SnO_2**	**Ba-SnO_2**
0 wt %	***E_g (eV)***	3,57	3,57	3,57
	E_u (eV)$^{-1}$	0,44	0,44	0,44
2 wt %	***E_g (eV)***	3.69	2.94	3.67
	E_u (eV)$^{-1}$	0.40	0.99	0.70
4 wt %	***E_g (eV)***	2.96	3.88	3.65
	E_u (eV)$^{-1}$	0.69	0.47	0.83
6 wt %	***E_g (eV)***	2.94	3.97	3.78
	E_u (eV)$^{-1}$	0.72	0.39	0.50
8 wt %	***E_g (eV)***	2.86	/	3.76
	E_u (eV)$^{-1}$	0.90	/	0.59

III. 3. Electrical properties

The curve of electrical conductivity (σ) and sheet resistance (R_{sh}) as a function of dopants concentration is illustrated in Figure III.10:

For Ca-SnO_2 films the electrical conductivity increases with the increase of Ca concentration to reach the highest value (84.84 $(\Omega.cm)^{-1}$) at 8 wt % of calcium, while the sheet resistance inversely proportional to electrical conductivity, we can explain this increase by increasing crystallite size that led to the decrease in the crystalline defects (grain boundaries) [25], this reduces the possibility of forming traps carriers, the inverse observation was found in other research of In-SnO_2 [21].

The electrical conductivity increases rapidly from 5.79 $(\Omega.cm)^{-1}$ for pure SnO_2 to 27.92 $(\Omega.cm)^{-1}$ for 2 wt % of Sr doped SnO_2, then it was decrease slowly to 22.96 $(\Omega.cm)^{-1}$ for 4 wt % of strontium, the electrical conductivity continues to decrease until it reaches the lowest value, which is 2.41 $(\Omega.cm)^{-1}$ for 6 wt % of Sr, as we note, the electrical properties of this sample deteriorated compared to pure tin dioxide. So, the increase in the conductivity is always demonstrated by the enhancement of the film's crystallisation as it is mentioned in the previous paragraph, while the decreases can the explained by changes at the ionic level in the crystal lattice, whenever the substitution of Sn^{4+} by Sr^{2+} lead to formation of two holes because of due to the difference in electronegativity between the two ions where the strontium ions accepted two electrons from the tin ions which become unable to bind with oxygen then this latter is removed from the crystal lattice to form an oxygen vacancy [13].

For Ba-SnO_2 films the electrical conductivity variations is differentiated, the maximum value was founded at a medium value of Ba doped SnO_2 which was 4 wt % (63.04 $(\Omega.cm)^{-1}$).

As we note, the electrical conductivity always has low values at high concentrations of dopant elements Sr and Ba may be because of the difference between the ionic radii between the tin ion and Sr and Ba ions, since its ionic radii is larger than the ionic radii of Sn^{4+} leads to the formation of many crystallin defects which form the traps carriers, where for the Ca-SnO_2 this note is not correct because of the small difference in the ionic radius.

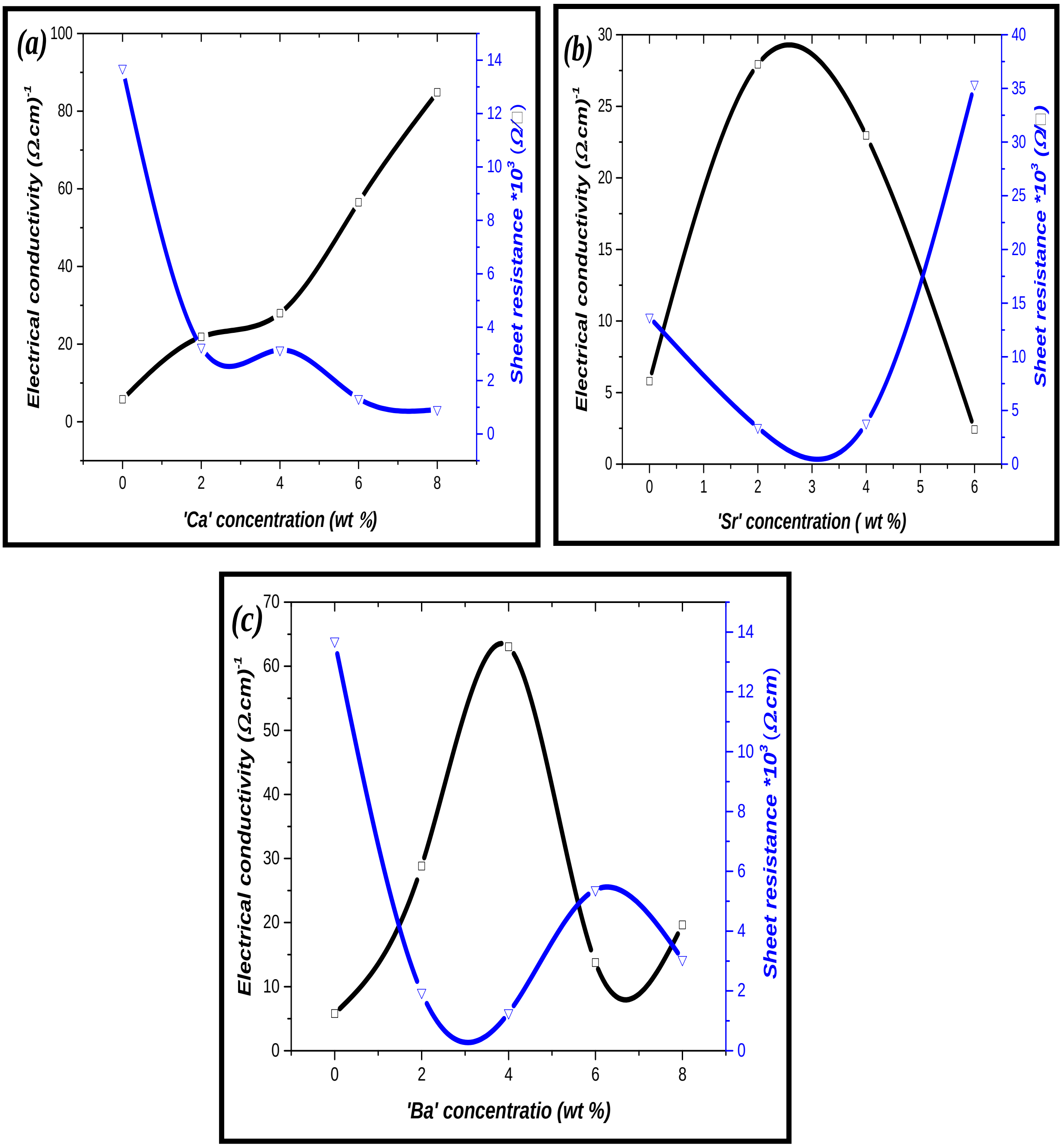

Figure III.10. Electrical conductivity and sheet resistance variations of: (a) Ca-SnO_2, (b) Sr-SnO_2, and (c) Ba-SnO_2 films.

References

[1] C. Khelifi, A. Attaf, H. Saidi, A. Yahia, M. Dahnoun, A. Saadi, Effect of solution flow on the properties of tin dioxide SnO_2 thin films deposited by spray pyrolysis technique, Optik. 127 (2016), 11055–11062, https://doi.org/10.1016/j.ijleo.2016.09.060.

[2] M. A. Islam, J. R. Mou, M. F. Hossain, M. A. H. Shah, M. S. Hossain, Investigation of structural, optical and photoluminescence properties of nanostructured $Ba_xSn_{1-x}O_2$ thin films: An effect of Ba doping, Thin Solid Films. 709 (2020), 138240, https://doi.org/ 10.1016/j.tsf.2020.138240.

[3] R. Ramarajan, M. Kovendhan, K. Thangaraju, D. P. Joseph, R. R. Babu, V. Elumalai, Enhanced optical transparency and electrical conductivity of Ba and Sb co-doped SnO_2 thin films, J. Alloys Compd. 823 (2020),153709,https://doi.org/10.1016/j.jallcom.2020.153709.

[4] S. Peddavarapu, H. S. Akkera, T. R. K. Reddy, G. S. Reddy, N. Kambhala, N. N. K. Reddy, Influence of Ga doping on structural , optical and electrical properties of transparent conducting SnO_2 thin films, Optik. 226 (2021), 165859, https://doi.org/ 10.1016/j.ijleo.2020.165859.

[5] S. Peddavarapu, H. S. Akkera, T. R. K. Reddy, Y. Bitla, V. Ganesh, P. M. Kumar , G. S. Reddy, M. Poloju, Effect of Ti doping on structural , optical and electrical properties of SnO_2 transparent conducting thin films deposited by sol-gel spin coating, Optical Materials. 113 (2021), 110845, https://doi.org/10.1016/j.optmat.2021.110845.

[6] Allag Abdelkrim, S. Rahmane, O. Abdelouahab, N. Abdelmalek, Effect of solution concentration on the structural, optical and electrical properties of SnO_2 thin films prepared by spray pyrolysis, Optik. 127 (2016), 2653-2658, https://doi.org/10.1016/j.ijleo.2015.11.232.

[7] H. Soumia, “ Elaboration des nanostructures de semi-conducteur SnO_2 dopé au Strontium et étude de leurs propriétés structurales,optiques et photocatalytiques”, University of Mentouri Constantine- Algeria, 2018.

[8] C. Khelifi, A. Attaf , H. Saidi, A. Yahia, M. Dahnoun, Investigation of F doped SnO_2 thin films properties deposited via ultrasonic spray technique for several applications, Surfaces and Interfaces. 15 (2019), 244-249, https://doi.org/ 10.1016/j.surfin.2019.04.001.

[9] A. Abdlekrim, “Optimization of elaboration conditions of tin oxide Sn02 thin films by

spray”, University of Biskra- Algeria, 2016.

[10] M. A. Islam, J. R. Mou, M. F. Hossain, M. A. H. Shah, M. A. K. Zilani, M. S. Hossain, Synthesis and characterization of tetragonal and orthorhombic $Sn_{1-x}Ba_xO_2$ nanostructures via the spray pyrolysis method, Optical Materials Express. 10 (2020), 3245-3256, https://doi.org/10.1364/OME.399502.

[11] M. Mazumder, A. Bharati, S. Saha, D. Sen, K.K. Chattopadhyay, Effect of Mg doping on the electrical properties of SnO_2 nanoparticles, Current Applied Physics. 12 (2012), 975-982, https://doi.org/10.1016/j.cap.2011.12.022.

[12] F. Zeribi, A. Attaf, A. Derbali, H. Saidi, L. Benmebrouk, M. S. Aida, M. Dahnoun, R. Nouadji, H. Ezzaouia, Dependence of the Physical Properties of Titanium Dioxide (TiO_2) Thin Films Grown by Sol-Gel (Spin-Coating) Process on Thickness, ECS Journal of Solid State Science and Technology. 11 (2022), 023003, https://doi.org/10.1149/ 2162-8777/ac5168.

[13] K. Chafia, “Tin dioxide SnO_2 thin films deposited by ultrasonic spray technique: Properties and Applications”, University of Biskra- Algeria, 2018.

[14] L. Soussia, T. Garmim, O. Karzazi, A. Rmili, A. El Bachiri,d , A. Louardi, H. Erguig, Effect of (Co, Fe, Ni) doping on structural, optical and electrical properties of sprayed SnO_2 thin film, Surfaces and Interfaces. 19 (2020), 100467, https://doi.org/ 10.1016/j.surfin.2020.100467.

[15] M.S. Bannur, A. Antony, K.I. Maddani, A. Ani, P. Poornesh, A. Rao, K.S. Choudhari, S. D. Kulkarni, Improved nonlinear absorption mechanism of tin oxide thin films: Role of strontium doping, Optical Materials. 94 (2019),294-298, https://doi.org/ 10.1016/j.optmat.2019.06.003.

[16] S. M. Ali, J. Muhammad, S. T. Hussain, S. A. Bakar, M. Ashraf, N-ur-Rehman, Study of microstructural, optical and electrical properties of Mg dopped SnO thin films, J Mater Sci: Mater Electron. 24 (2013), 2432-2437, https://doi.org/10.1007/s10854-013-1114-5.

[17] L. Zhang, W. Zhang, X. Lu, Q. Wang, X. Yang, L. Shi, S. Lun, Preparation and Characterization of $CdIn_2S_4$ Wedgelike Thin Films, Chinese Automation Congress (CAC), e of New Energy, Jinzhou, Liaoning, China, 2013, 789–794, https://doi.org/ 10.1109/CAC.2013.6775841.

[18] S. K. Apte, S. N. Garaje, R. D. Bolade, J. D. Ambekar, M. V. Kulkarni, S. D. Naik, S. W. Gosavi, J. O. Baegc, B. B. Kale, Hierarchical nanostructures of $CdIn_2S_4$ via hydrothermal and microwave methods: efficient solar-light-driven photocatalysts, Journal of Materials Chemistry. 20 (2010), 6095-6102, https://doi.org/ 10.1039/c0jm00538j.

[19] N. Rahima, "Elaboration and characterisation of undoped and doped indium oxide thin layers elaborated by sol gel process for photonic and photovoltaic applications", University of Biskra- Algeria, 2022.

[20] A. Nadjate, F. Hichem, Influence of Fe and Al Dopants on the Optical Properties of Zinc Oxide Thin Films Obtained by Spray Pyrolysis, International Journal of Engineering Research in Africa. 29 (2017), 21-27, https://doi.org/10.4028/www.scientific.net/JERA.29.21.

[21] B. Kheira, "Elaboration and characterization of SnO_2:In thin films deposited by spray pyrolysis technique", University of Biskra- Algeria, 2020.

[22] S. Rahmane, M.A. Djouadi, M.S. Aida, N. Barreau, B. Abdallah, N. H. Zoubir, Power and pressure effects upon magnetron sputtered aluminum doped ZnO films properties, Thin Solid Films. 519 (2010), 5–10, https://doi.org/ 10.1016/j.tsf.2010.06.063.

[23] S. Rahmane, M. A. Djouadi, M. S. Aida, N. Barreau, Oxygen effect in radio frequency magnetron sputtered aluminium doped zinc oxide films, Thin Solid Films. 562 (2014), 70-74, https://doi.org/ 10.1016/j.tsf.2014.03.073.

[24] Z. Zarhri, A. D. Cano, O. Oubram, Y. Ziat, A. Bassam, Optical measurements and Burstein Moss effect in optical properties of Nb-doped Ba Sn O_3 perovskite, Micro and Nanostructures. 166 (2022), 2072,23 https://doi.org/ 10.1016/j.micrna.2022.207223.

[25] R. Saâd, "Elaboration et caracterisation de couches minces par spray pyrolyse et pulverisation magnetron", University of Biskra- Algeria, 2008.

Chapter Ⅳ:

DFT and comparison study of pure and doped SnO_2 thin films

In this chapter, we present the fundamental definitions related to density functional theory (DFT). Additionally, an overview of the approximations used to simplify the solution of the Schrödinger equation will be provided. The Cambridge Serial Total Energy Package (CASTEP) code will also be defined within this chapter. Throughout this chapter, we will present the results and discussions pertaining to the geometry optimization of SnO_2. Furthermore, a comparative analysis of the structural, electronic, and optical properties encompassing volume cell and lattice parameters, density of states, and absorption coefficient, respectively will be conducted for both pure and Ca, Sr, and Ba doped SnO_2, considering 2x2x1 and 1x1x2 supercells.

IV. 1. Density Functional Theory (DFT)

IV. 1.1. DFT definition

The density functional theory (DFT) is a quantum resolution approach that indicates that a system's electronic structure and its energy can be evaluated using its total electron density of composed by N interacting single electrons densities. Logically, when we mention (DFT), we are actually talking about the Schrödinger equation's solution, which is very difficult and impossible to find it analytically for an isolated atom and becomes more complex when approaching the real situation where atoms are bonded to form materials in nature, therefore, several approximations and models were used to reduce this complexity from. The most important are Born-Oppenheimer, Hartree, Hartree-Fock approximations, and Kohn-Sham model.

IV. 1.2. Schrodinger Equation

Schrödinger equation is the fundamental equation created by Erwin Schrödinger in 1925 [1], which is given by:

$$\hat{H} \mid \psi\rangle = E \mid \psi\rangle \qquad \text{(IV.1)}$$

Where $\hat{H}$ is the Hamiltonian operator, ψ is the wave function., and E is the total energy.

For a system of N_n nuclei and N_e electrons is written as follows:

$$H\, \psi_n (\vec{r}_i, \vec{R}_N) = E_n\, \psi_n (\vec{r}_i, \vec{R}_N) \qquad \text{(IV.2)}$$

Where 'n' is the principal quantum number, $\vec{r}_i$ is the position vector of an electron, and $\vec{R}_N$ is the position vector of a nucleus. The Hamiltonian operator is the sum of several operators and is identified by [2]:

$$H = T_e + T_N + V_{eN} + V_{ee} + V_{NN} \qquad \text{(IV.3)}$$

Where T_e and T_N are the kinetic energy operators of electrons and nuclei, respectively

$$T_e = -\sum_{i}^{N_e} \frac{\hbar^2}{2m} \nabla_i^2 \qquad \text{(IV.4)}$$

$$T_N = -\sum_{i}^{N_n} \frac{\hbar^2}{2M} \nabla_i^2 \qquad \text{(IV.5)}$$

With:

- m: the electron mass.
- M: the nuclei mass.
- $\hbar$: the reduced Planck constant.
- ∇: the spatial differentiation operator.

And V_{ee}, V_{eN}, and V_{NN} are operators of electron- electron interaction, electron-nuclei interaction, and nuclei-nuclei interaction respectively, the following equations define each potential separately:

$$V_{ee} = \sum_{i<j} \frac{e^2}{|\vec{r}_i - \vec{r}_j|}, \qquad \text{(IV.6)}$$

With:

- e: the elementary electric charge.
- $\vec{r}_i$ and $\vec{r}_j$: are the vectors position of *i* and *j* electron respectively. For the condition *i<j* to avoid the double interaction between i and *j* electrons.

$$V_{eN} = -\sum_{i,I} \frac{Z_I e^2}{|\vec{r}_i - \vec{R}_I|}, \qquad \text{(IV.7)}$$

With:

- Z_I: the atomic number of the atom corresponding to 'I' nucleus.
- $\vec{r}_i$: the position vector of *i* electron.
- R_I: the position vector of 'I' nuclei.

$$V_{NN} = \sum_{I<J} \frac{Z_I Z_J e^2}{|\vec{R_I} - \vec{R_J}|}, \qquad \text{(IV.8)}$$

With:

- $\vec{R}_I$ and $\vec{R}_J$: are the vectors position of *I* and *J* nuclei respectively. For the condition $I<J$ to avoid the double interaction between *I* and *J* nuclei.
- Z_I and Z_J: the atomic number of *I* and *J* atoms respectively.

IV. 1.3. Born-Oppenheimer approximation

In 1927 the two scientist Max Born and J. Robert Oppenheimer presented Born-Oppenheimer approximation, which supports the separation of nuclear and electronic movements [3], this corresponds to the obvious reason that the atomic nucleus is significantly heavier than an electron (around 1800 to 2000 times) [1], that is why, the electron can be considered moving while the nucleus is fixed, so, the nuclei operator kinetic energy (T_N) can be neglected and also the potential operator of nuclei-nuclei interaction (V_{NN}) being constant, which makes the new total energy in the Schrödinger equation is $E' = E - V_{NN}$.

The Hamiltonian expression of the system is a little simplified as shown below:

$$H = T_e + V_{eN} + V_{ee} \qquad \text{(IV.9)}$$

However, the operator of electron-electron interaction remains a complication when trying to solve the Schrödinger equation analytically, and making it impossible as it is mentioned in the beginning of this chapter, that is why many approximations was used to solve it such as Hartree and Hartree-Fock approximation.

IV. 1.4. Hartree approximation

In order to simplify the operator of electron-electron interaction (V_{ee}) Hartree considered the system of N_e electron in interaction becomes a system in which each independent electron interacts with a field created by sum of the other electrons. From now on, we cannot talk about electron-electron interaction but about interaction between electron '*i*' and electronic distribution $\rho(\vec{r})$ surrounding it. $\rho(\vec{r})$ is determined by the following equation with ($i \neq j$) [4]:

$$\rho(\vec{r}) = \sum_j \phi_j^*(\vec{r})\, \phi_j(\vec{r}) \qquad \text{(IV.10)}$$

So, by adding this approximation, the poly-electronic wave function written as a product of mono-electronic wave functions of the system with Ne electron ($\phi(\vec{r}_i)$, $i = 1, \ldots, N_e$):

$$\psi(\vec{r}_1, \vec{r}_2, \ldots\ldots, \vec{r}_{N_e}) = \prod_i \phi(\vec{r}_i) \qquad \text{(IV.11)}$$

Therefore, the operator of electron-electron interaction V_{ee} replaced by potential Hartree operator V_H which is a classical coulomb potential expressed as a function of the distribution electronic ($\rho(r)$).

$$V_H(\vec{r}) = \int \frac{n(\vec{r})}{|\vec{r}-\vec{r}'|}\, d^3r' \qquad \text{(IV.12)}$$

As a result, the new Hamiltonian writes as follows:

$$H = T_e + V_H + V_{eN} \qquad \text{(IV.13)}$$

However, this approximation does not definitively solve the complexity of solving the Schrödinger equation found in Schrödinger equation, since to that the obtained energy is not calculated in an accurate way because the Pauli exclusion principle was not taken into account, which states that two electrons having parallel spins (⇈ or ⇊) cannot be in the same quantum state, that is why another approximation was developed which is Hartree-Fock approximation.

IV. 1. 5. Hartree-Fock approximation

In 1930 Fock point out the contradiction between Hartree's approximation and Pauli's exclusion principle which considers that electrons have the properties of fermions [5], therefore, a vector with four coordinates was defined ($\vec{\chi}_i$) that combines each electron's spatial coordinates (x_i, y_i, z_i) and its spin (σ_i):

$$\vec{\chi}_i = \begin{pmatrix} x_i \\ y_i \\ z_i \\ \sigma_i \end{pmatrix} \qquad \text{(IV.14)}$$

Also, the global wave function related to the new vector becomes antisymmetric:

$$\psi(\vec{\chi}_1, \vec{\chi}_2, \dots \vec{\chi}_i, \dots, \vec{\chi}_j \dots, \vec{\chi}_{N_e}) = -\,\psi(\vec{\chi}_1, \vec{\chi}_2, \dots \vec{\chi}_i, \dots, \vec{\chi}_j \dots, \vec{\chi}_{N_e}) \qquad \text{(IV.15)}$$

So, after the Hartree-Fock approximation the global wave function can be expressed as a determinant which is named the Slater determinant [6]:

$$\psi(\vec{\chi}_1, \vec{\chi}_2, \dots, \vec{\chi}_{N_e}) = \frac{1}{\sqrt{N_e!}} \begin{bmatrix} \psi_1(\vec{\chi}_1) & \cdots & \psi_{N_e}(\vec{\chi}_1) \\ \vdots & \ddots & \vdots \\ \psi_1(\vec{\chi}_{N_e}) & \cdots & \psi_{N_e}(\vec{\chi}_{N_e}) \end{bmatrix} \qquad \text{(IV.16)}$$

Where the mono-electronic wave functions ($\psi_i(\vec{\chi}_i)$ are products of functions spin-orbital orthonormal. This approximation takes into consideration only the parallel spins electrons (exchange interactions), and the Schrödinger equation's solutions obtained are not unique therefore, it is not possible to obtain the fundamental state (ground energy), that is why the use of other approximations is very important which take into account the non-parallel spin electrons (correlation interactions).

IV. 1. 6. Kohn-Sham equation

The Kohn-Sham system (1965) [7] transforms a system of N_e electrons interacting to a system of N_e electrons independent under the influence of potential V_{eff} (effective potential).

$$V_{eff}(\vec{r}) = V_{ext}(\vec{r}) + V_H(\vec{r}) + V_{ncl}(\vec{r}) \qquad \text{(IV.17)}$$

Where:

V_{ext}: exterior potential.

V_H: Hartree potential.

V_{ncl}: the potential for non-classical electronic interactions.

Also, Kohn-Sham made a note of the mono-electronic equations for each *i* electron written as follows [8]:

$$\left[-\frac{\hbar^2}{2m}\vec{\nabla}_i^2 + V_{eff}(\vec{r})\right]\phi_i(\vec{r}) = E_i\phi_i(\vec{r}) \qquad (IV.18)$$

The purpose is always to find the total energy of the fundamental state E(ρ) which given by the following equation [9]:

$$E_{KS}(\rho) = T_S[\rho] + E_H[\rho] + E_{xc}[\rho] + \int v_{eff}(\vec{r})\,\rho(\vec{r})d\vec{r} \qquad \text{(IV. 19)}$$

Where:

$T_S[\rho]$: Kinetic energy of N_e independent electrons.

$E_H[\rho]$: Hartree energy.

$E_{xc}[\rho]$: exchange-correlation energy between the electrons.

So the complexity to find $E_{KS}[\rho]$ lies in the last part of the equation ($E_{xc}[\rho]$), since, according to what we mentioned previously, in Hartree-Fock approximation we can find just the electronic exchange energy ($E_x[\rho]$) which is related to electrons with parallel spin, while for the correlation energy related to the non-parallel spin electrons, the complexity still exists and the possibility of finding the total energy it is still difficult, so other approximations were used to solve this problem, from most important of which is: the local density approximation (LDA) and the generalized gradient approximations (GGA).

IV. 1.7. Local density approximation (LDA)

The LDA is a very simple approximation to estimate the exchange-correlation energy where is considered the system of N_e as a homogeneous (uniform) electron gas [1, 9, 10].$E_{xc}^{LDA}[\rho]$ is given by the following expression:

$$E_{xc}^{LDA}[\rho]=\int \rho(r)\, E_{xc}\,[\rho]\, dr \qquad (IV.20)$$

Where E_{xc} [ρ] [2] is the exchange correlation energy of the uniform gas with constant density. The local density approximation leads to a large estimate of the forces that make the atoms more attracted o each other than necessary, that is why the error relative value of the lattice parameters is big ranging between 7 % to 10 %, that is why the LDA has been improved to another approximation which is the generalized gradient approximation (GGA).

IV. 1. 8. Generalized gradient approximation (GGA)

The GGA is an enhancement to the local density approximation, that is why the exchange and correlation energy was calculated using the electron density and its gradient [11-13], $E_{xc}^{GGA}[\rho]$ can be written as follow:

$$E_{xc}^{GGA}[\rho_\uparrow,\rho_\downarrow] = \int f(\rho_\uparrow(\vec{r}),\nabla\rho_\uparrow(\vec{r}),\rho_\downarrow(\vec{r}),\nabla\rho_\downarrow(\vec{r}))d^3r \qquad (IV.21)$$

IV. 2. CASTEP calculation code

Cambridge Serial Total Energy Package code was used to do all the calculations presented in this chapter. CASTEP is a simulation program based on quantum mechanics designed specifically for studying solid states materials, it uses the DFT to solve the Schrödinger equation and employs the pseudopotentials to extract crystalline, optical and surface materials properties without necessitating any experimental input; among these materials semiconductors, ceramics, and metals...etc [14, 15].

So, the CASTEP has just two input files which are: <name>. cell, and <name>. param. The first file contains a detail about the cell of the material to be studied like the atomic position, and the angles (α, β, and γ) …etc; while the most important detail in the second file is the task which determines the calculations to be performed (Geometry optimisation, Band Structure…. etc) [16]. Also, the pseudopotential type used for estimating exchange-correlation energy is essential in this file, where the PBE (Perdew Burke Ernzerhof) was employed in this chapter. Also, the pseudopotential type used for estimating exchange-correlation energy is essential in this file, where the PBE (Perdew Burke Ernzerhof) was employed in this chapter.

IV. 3. Results and discussions

IV. 3.1. Geometry optimisation of SnO_2 (1x1x1 cell)

- **Cut-off energy optimisation**

Ihe Kinetic energy cut-off is the energy that is being optimized, where only the plane waves that have an energy less than or equal to the cut-off energy are taken into account. The plane waves are expressed by the following equation [17]:

$$\psi_K(r)=\sum_G C_{K,G}\, e^{i\,(K+G)*r} \qquad \text{(IV.22)}$$

This plane wave can be represented by a grid in the k-plane, the large number of these grid increases the calculation accuracy, but it takes a long time, to avoid this from happening, the following condition must be satisfied [8]:

$$\frac{\hbar^2|K+G|^2}{2m} \leq E_{cut} \qquad \text{(IV.23)}$$

In this study the cut-off energy varied in the range of 100 eV to 1000 eV. Figure IV.1 represent the total energy variations in terms of cut-off energy, where the optimized cut-off energy was 800 eV.

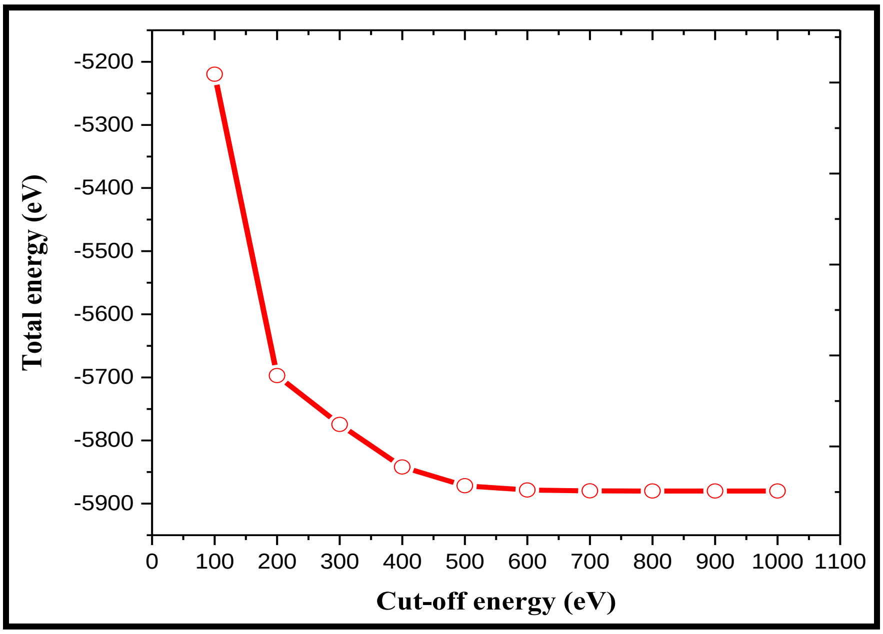

Figure IV.1. Total energy convergence in terms of cut-off energy.

- **K-points optimisation**

The k-points are the division of the reciprocal lattice's primitive cell which is known by the first Brillouin zone (1BZ), this deviation is done in the three directions of reciprocal space which are k_x, k_y, and k_z, where the goal of this is to make sure that the wave function's changes near to k-point are slow to be able to extract accurate information. And always the choice of k-points number has a very important role in the optimization, so a few points chosen give fast total energy convergence [5,8].

In our study we knew that the SnO_2 has a tetragonal rutile structure where *a=b (4.75 A°)>c (3.18A°)* (Figure IV.2 displays tin oxide "cell 1x1x1"), that is why it should always be $k_x = k_y < k_z$. Figure IV.3 shows the variations of total energy as a function of k-points, where (8 8 10) was used as an optimal deviation.

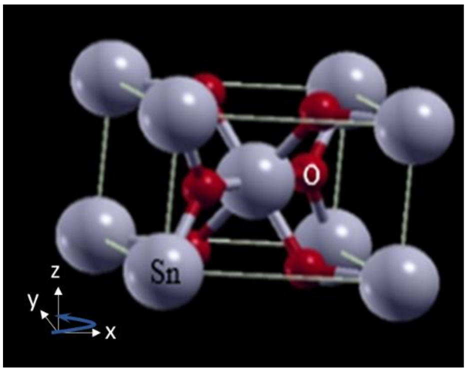

Figure IV.2. Schematic representation of the SnO_2 (1x1x1 cell) using CASTEP code.

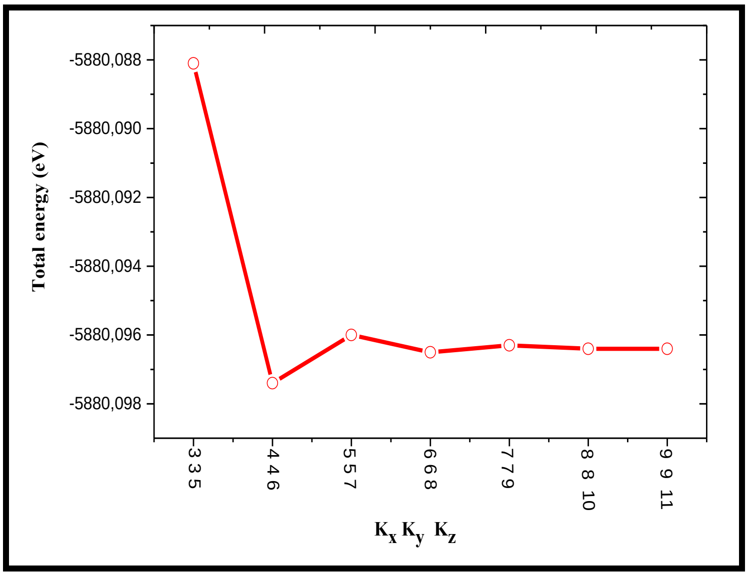

Figure IV.3. Total energy convergence in terms of k-points.

IV. 3.2. Structural optimisation of pure and M-doped SnO_2 (2x2x1 and 1x1x2 supercells)

In order to shows the effect of the incorporation of a metal M (which could be Ca, Sr, or Ba) dopants on structural properties of SnO_2 we introduced them as impurities with low atomic ratio equal to 4.16 at % (2x2x1 supercell) and hight atomic ratio of 8.33 at % (1x1x2 supercell), where in the two types of supercells the tin atom of (0; 0;0) position was replaced by 'M' atom.

- **Lattice parameters and volume cell (2x2x1 supercell)**

A representation of pure and M-doped SnO_2 was configured in Figure IV.4. for 2x2x1 supercell.

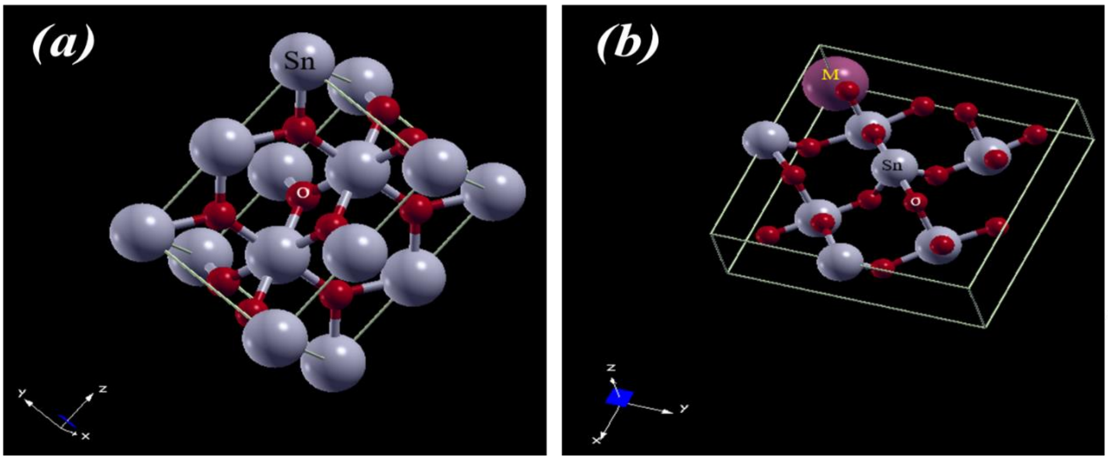

Figure IV.4. Configuration of 2x2x1 supercell for: *(a)* pure SnO_2, and *(b)* M-doped SnO_2.

Table IV.1 shows a crystal structure geometry optimization of pure and M-doped SnO_2, we notice that it has the same tetragonal rutiles structure for which the only effect of the substituted atoms results an expansion in the lattice parameters and volume cell, where the expansion ratio rises from 6.88 % to 9.80 % and 12.03 % as the dopant metal ionic radius increases from 1.12 A° to 1.32 A° and 1.35 A° respectively. One can say that this expansion is surely due to the large ionic radii of dopant elements compared to 'Sn'. Similar results were found by the researchers Petros-Panagis Filippatos et al. [18] due to the chosen halogens as a dopant for tin dioxide by replacing the oxygen atoms which has a small atomic radius compared to halogens.

Table IV.1: Optimization of lattice parameters, and volume cell for pure and M-doped SnO_2 (2x2x1 supercell).

	a (°A)	*c (°A)*	*v (°A)^3*
Pure SnO_2	4.517	3.014	61.495
Ca-SnO_2	4.659	3.028	65.726
Sr-SnO_2	4.716	3.036	67.522
Ba-SnO_2	4.752	3.051	68.896

- **Lattice parameters and volume cell (1x1x2 super cell)**

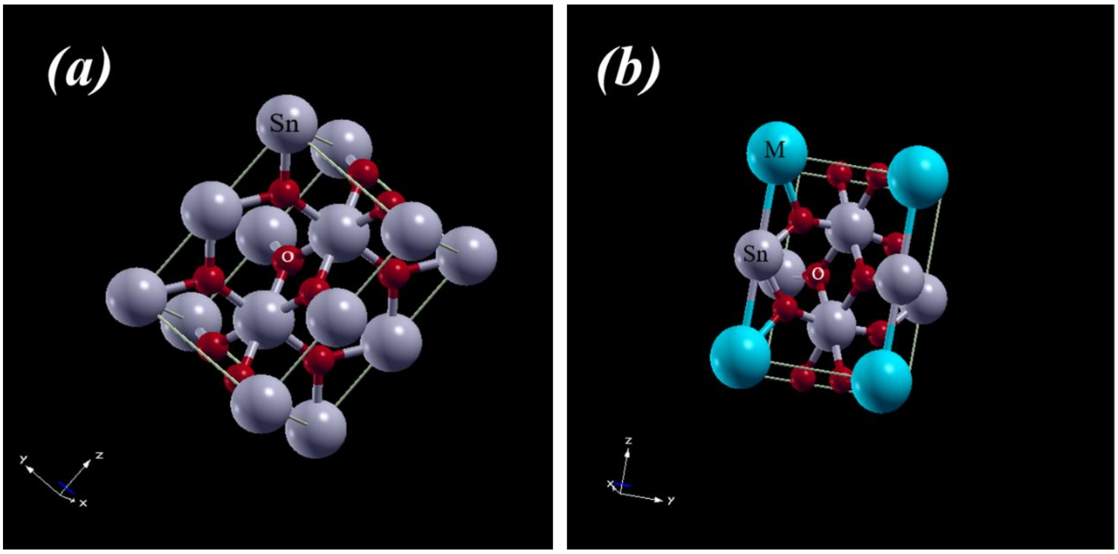

Figure IV.5. Configuration of 1x1x2 supercell for: *(a)* pure SnO_2, and *(b)* M-doped SnO_2.

For the 1x1x2 supercell which represents an atomic percentage doping of 8.33 at %, the results were presented in Table IV.2 where it is clearly shown that all of the lattice parameters and volume cell were increased in line with increasing of ionic radii of 'M' dopants except for the *'a'* parameter of the of Ba-SnO_2 compound. We notice that it was decreased compared to the other two dopants while it was expected that it would increase. Nevertheless, it remains larger than its value for the pure SnO_2. This sudden change could be due to the high concentration and the fact that the barium atom is much larger compared to the host atom (which is the 'Sn' atom), therefore it is probable there will be many crystalline defects such as misplaced positioning of the atoms inside the crystal cell which may lead to a decrease or increase in lattice parameters in one of the directions. Our results are in agreement with the theoretical study of Apostolov et al. [19] who obtained a decrease in the lattice parameters of CeO_2 doped with a high concentration of 'Y' although itirium ion radius although itirium ion radius is greater than of the cesium ion.

Table IV.2: Optimization of lattice parameters, and volume cell for pure and M-doped SnO_2 (1x1x2 supercell).

	a (A°)	***c (A°)***	***v (A°)³***
Pure SnO_2	4.524	3.007	61.542
Ca-SnO_2	4.668	3.182	69.336
Sr-SnO_2	4.672	3.295	71.921
Ba-SnO_2	4.581	3.635	76.282

IV. 3.3. Band structure of pure and M-doped SnO_2 (2x2x1 and 1x1x2 supercells)

- **Definition of band structure**

Band structure, or electronic band structure is the contribution of electrons in the electrical and optical properties of a material. To explain the formation of a gap we should talk firstly about the electrons of a single atom which contains a discrete energies level and is partially filled by electrons, when the crystal is formed, the atoms become very close together which leads to interchangeable interaction between them, that leads to the formation of many energy levels which appears in the form of the band structure, the most important property that can be extracted from band structure curves is the band gap value which is the energy difference between the top of the valence band and the bottom of the conduction band, the importance of this property lies in its width because it is strongly related to the wavelength absorbed in photocatalytic application [20].

- **Band structure of 2x2x1 supercell**

Figure IV.6 (*a, b, c, and d*) illustrates the calculated band structures of pure and M-doped SnO_2 for 2x2x1 supercell which represents 4.16 % doping atomic ratio.

All the studied samples have a direct band gap because the maximum of the valence band and the minimum of the conduction band are located at the same point 'G' which is located in the first Brillouin zone (1BZ), so the films studied were a semi-conductor.

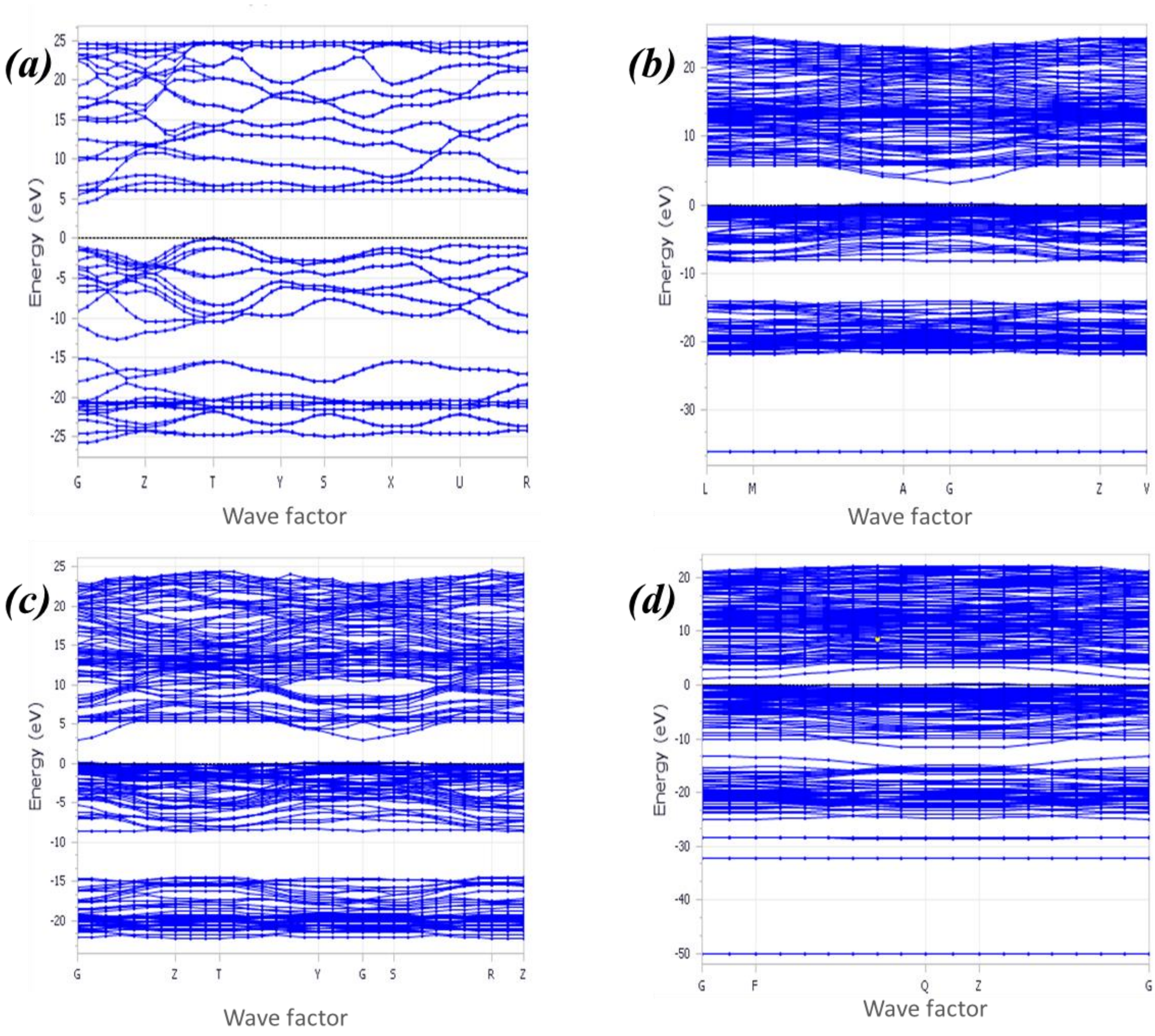

Figure IV.6. Band structure of pure and M-doped SnO_2 for 2x2x1 supercell.

All the band gap values represented in Table IV.3, pure SnO_2 had the value of 4.36 eV, it is worth taking into account that our results are in good agreement with the experimental researches [21, 22], and also with the other DFT studies [23]; a narrowing of the band gap was observed when adding dopant elements

- **Band structure of 1x1x2 supercell**

Figure IV.7 (*a, b, c, and d*) displays band structures of pure and Ca, Sr, Ba doped SnO_2 respectively at 8.33 at %, it is seen that the minimum of the conduction band and the maximum of the valence band are always at the same point in the first Brillouin zone (G), also all the studied samples have a band gap value medium which demonstrates that our study it is about semiconductors with a direct band gap. Pure SnO_2 had the value of 3.25 eV which is closely compatible with the theoretical and experimental study that was done [22, 23], the E_g values begin to decrease until they reach 0.11 eV for Ba-SnO_2, as can be seen, there is a big difference between this value and the experimental values which is due to the use of GGA-PBE approximation [24].

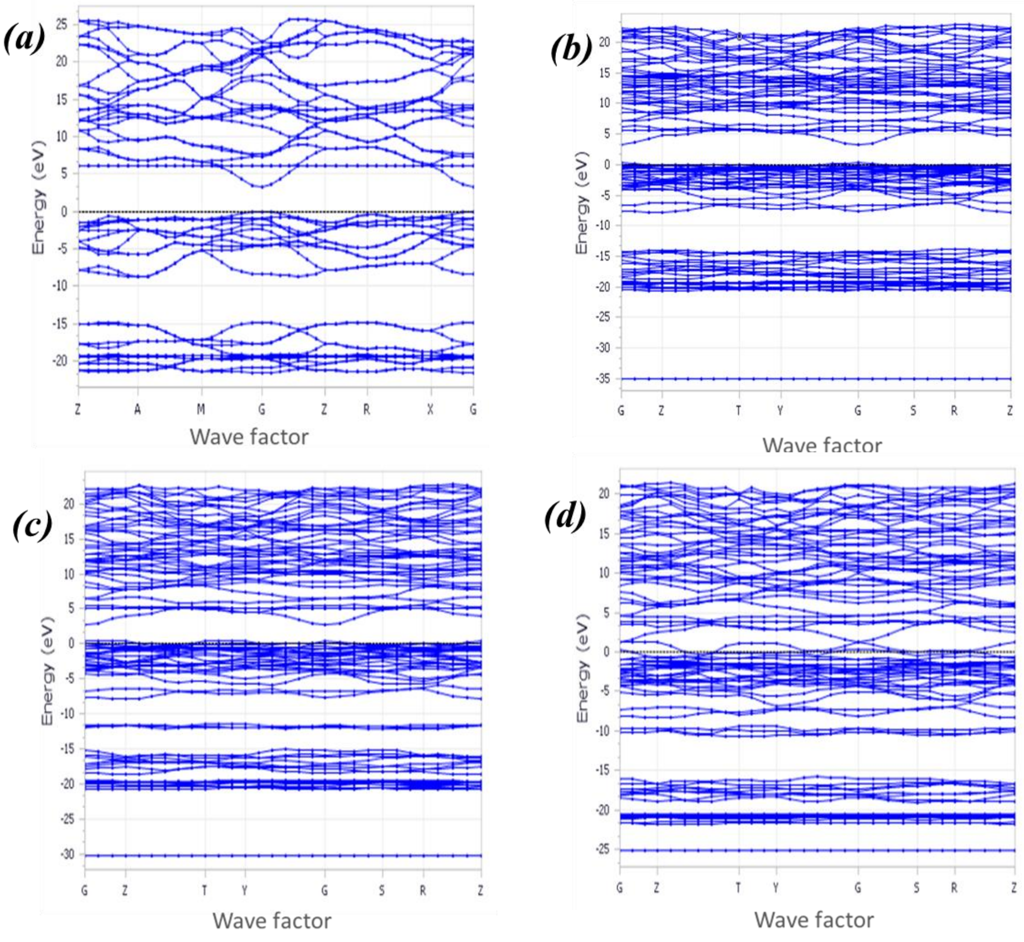

Figure IV.7. Band structure of pure and M-doped SnO_2 for 1x1x2 supercell.

Table IV.3: Band gap values of pure and M-doped SnO_2 for 2x2x1 and 1x1x2 supercells.

	Band gap values (eV)	
	2x2x1 super cell	**1x1x2 super cell**
Pure SnO_2	4.36	3.25
Ca-SnO_2	2.99	3.18
Sr-SnO_2	2.90	2.41
Ba-SnO_2	1.18	0.11

IV. 3.4. Optical properties of pure and M-doped SnO_2 (2x2x1 and 1x1x2 supercells)

- **Definition of absorption coefficient**

It is known as the fundamental absorption edge which is the threshold transitions between valence band maximum and conduction band minimum for a direct band gap as it is mentioned in the previous paragraphs [25], absorption coefficient α(ω) can be calculated using the following formula [5]:

$$\alpha(\omega) = \sqrt{2}\,\omega\,[(\varepsilon_1^2(\omega) + \varepsilon_2^2\ (\omega))^{\frac{1}{2}} - \varepsilon_1(\omega)]^{\frac{1}{2}} \qquad \text{(IV.24)}$$

- **Absorption coefficient of 2x2x1 supercell**

Figure IV.8 illustrate that the absorption edge values biggens nearly from 5.5 eV for pure SnO_2 and changed to 3.92, 3.11, and 2 eV for M-doped SnO_2 are at the same direction change with the band gap value measured from the band structures (Table IV.3), which, mean the absorption edge decreases for M-SnO_2 while the pristine SnO_2 had the highest value; to be more precise, there is an increases absorption of UV light. While, visible light had approximatively zero absorption (ranging of 3 eV - 1.5 eV), this lines with experimental results that is shows always a high transparency for the visible light according to the transmittance spectra.

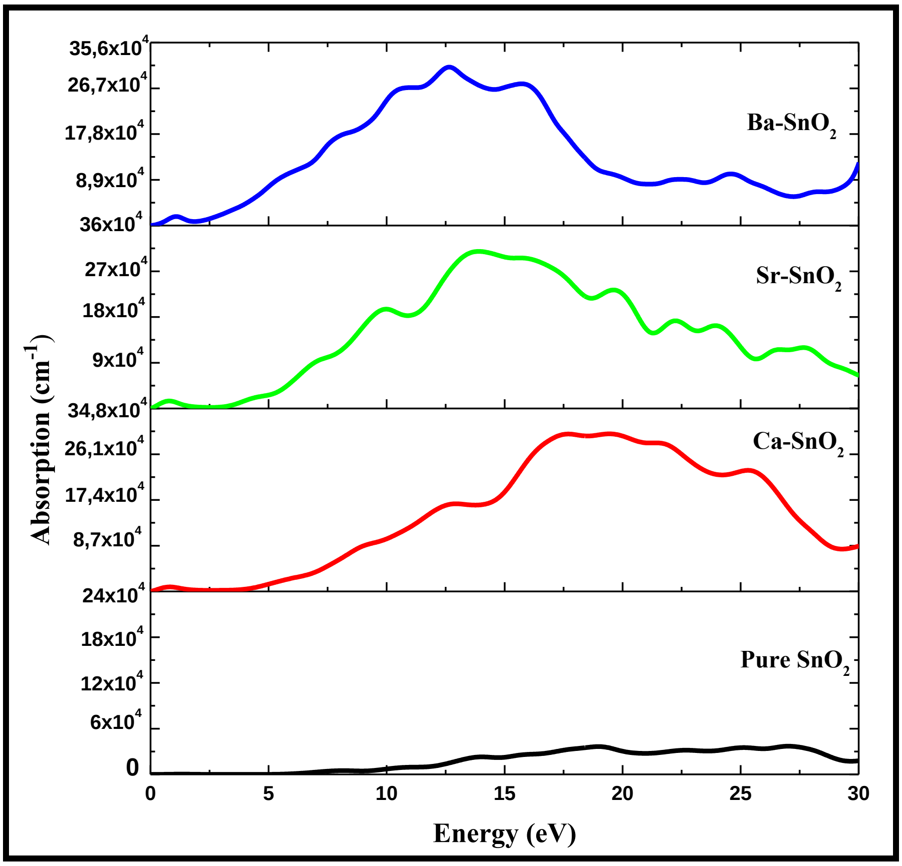

Figure IV.8. Variations of absorption coefficient for pure and doped SnO_2 (2x2x1) supercell

- **Absorption coefficient of 1x1x2 supercell**

Figure IV.9 clarifies the absorption coefficient variations of pure and M-doped SnO_2 for 1x1x2 supercell, it is shown that the absorption edge variation is in line with the band gap variation as it is seen clearly from Table IV.3, which means that it has decreased and directed towards the visible range, also it is seen that its intensity increases for M-doped SnO_2 compared to pure SnO_2, so according to the obtained results, the using of doping of alkaline earth elements as dopants for tin dioxide improved the absorption, which makes these prepared samples usable in the photocatalyst application.

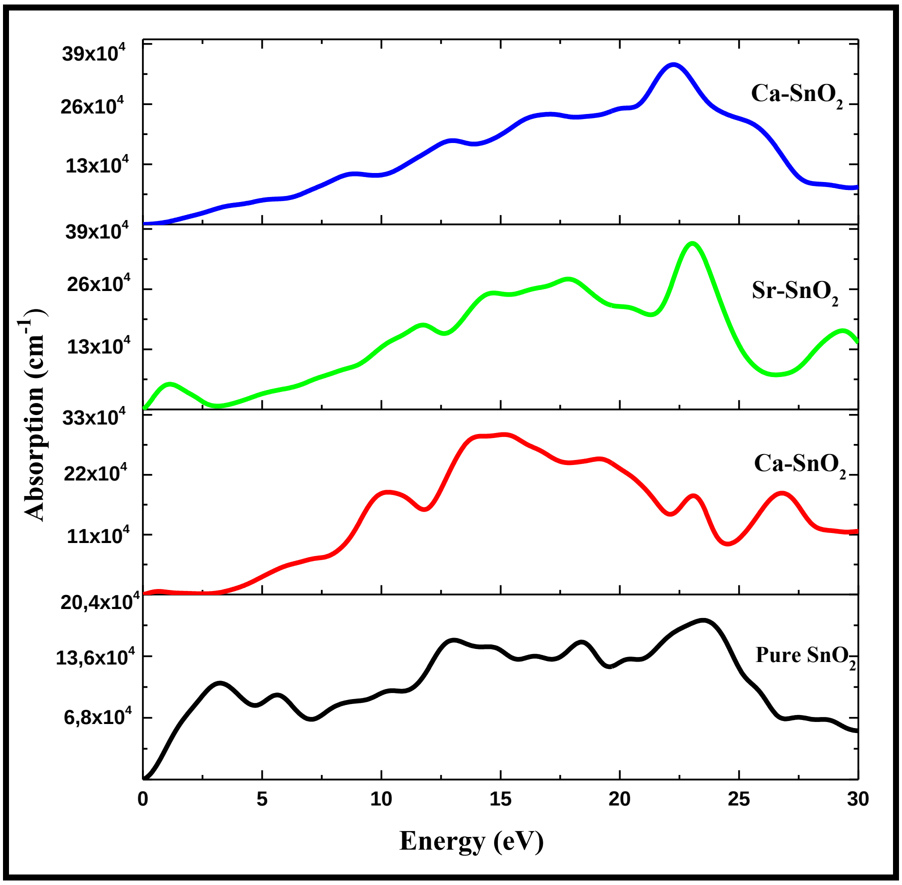

Figure IV.9. Variations of absorption coefficient for pure and doped SnO_2 (1x1x2) supercell

References

[1] H. Ouali, “des couches d’oxydes de cuivre Cu_xO pour une application capteurs de gaz”, University of Tunis Elmanar- Tunisia, 2015.

[2] O. Franck, “A closer look at wave-function/density-functional hybrid methods,” Pierre and Marie Curie University - Paris VI, 2017.

[3] D. C. Thompson, J. I. Rodriguez, An introduction to quantum chemistry, in: J. I. Rodríguez, F. Cortés-Guzmán and J. S.M. Anderson (Eds), Advances in Quantum Chemical Topology Beyond QTAIM, Elsevier Inc, 2023, pp. 21-36.

[4] P. K. Misra, Electron–Electron Interaction, in: P. K. Misra (Eds), Physics of Condensed Matter, Elsevier Inc, 2012, pp. 199-242.

[5] S. Saada, “Etude ab-initio des propriétés physiques des composés binaires et ternaires à base de Scandium”,University of Biskra- Algeria, 2020.

[6] V. Bach, S. Breteaux, S. Petrat, P. Pickl, T. Tzaneteas, Kinetic energy estimates for the accuracy of the time-dependent Hartree–Fock approximation with Coulomb interaction, J. Math. Pures Appl. 105 (2016), 1–30, https://doi.org/10.1016/j.matpur.2015.09.003.

[7] T. Hu, “Non-covalent functionalization of carbon nano-structures: A DFT study”, University of Toulouse-Paris, 2013.

[8] D. S. Sholl, J. A. Steckel, Nuts and Bolts of DFT Calculations,in: D. S. Sholl, J. A. Steckel (Eds), Density Functional Theory: A Practical Introduction, John Wiley & Sons, Inc, 2009, pp. 49-81.

[9] I. Hsin, “A study using density functional theory (DFT) of structural, electronic, and magnetic properties of superconductors are based on iron”, University of Ouargla-Algeria, 2017.

[10] F. S. Brigiano, “Reactivity at aqueous interfaces by DFT-MD simulations”, University of Saclay-Paris, 2020.

[11] A. G. Gebresilassie, “Atomic scale simulations in zirconia : Effect of yttria doping and environment on stability of phases”, University of Lyon-Paris, 2017.

[12] S. Kervazo, “ Computational Actinide Chemistry: Structure, Bonding and Thermodynamics”, University of Lille-Paris, 2018.

[13] M. Hofmann, H. F. Schaefer, Computational Chemistry, Computing in Science and Engineering. 5 (2003), 487–506, https://doi.org/10. 10.1109/MCISE.2003.1208636.

[14] Materials studio Datasheet CASTEP, How Does CASTEP work, 2001.

[15] BIOVIA Material Studio, Castep Guide, 2024.

[16] S. Clark, Introduction to the CASTEP code, University of Durham.

[17] P. Pitriana, T. D. K. Wungu, H. Herman, R. Hidayat, The computation parameters optimizations for electronic structure calculation of $LiPbI_3$ perovskite by the density functional theory method, IOP Conference Series: Materials Science and Engineering. 434 (2018), 1–5, https://doi.org/ 10.1088/1757-899X/434/1/012026.

[18] P.P. Filippatos, N. Kelaidis, A. Chroneos, M. Vasilopoulou, D. Davazoglou, Defect Processes in Halogen Doped SnO_2, Applied Sciences. 11 (2021), 1–14, https://doi.org/10.3390/app11020551.

[19] A. T. Apostolov, I. N. Apostolova, J. M. Wesselinowa, Magnetic Properties of Rare Earth Doped SnO_2, TiO_2 and CeO_2 Nanoparticles, Physica Status Solidi (B) Basic Research. 255 (2018), 1–6, https://doi.org/ 10.1002/pssb.201800179

[20] W. Xia, L. A. R. Pestana, Electronic structure and density functional theory, in: W. Xia, L. A. R. Pestana (Eds), Fundamentals of Multiscale Modeling of Structural Materials, Elsevier Inc, 2023, pp. 3-35.

[21] M. A. Abdulsattar, S. S. Batros, A. J. Addie, Indium doped SnO_2 nanostructures preparation and properties supported by DFT study, Superlattices and Microstructures. 100 (2016), 342–349, https://doi.org/ 10.1016/j.spmi.2016.09.042.

[22] M. Karmaoui, A. B. Jorge, P. F. McMillan, A. E. Aliev, R. C. Pullar, J. A. Labrincha, D. M. Tobaldi, One-Step Synthesis, Structure, and Band Gap Properties of SnO_2 Nanoparticles Made by a Low Temperature Nonaqueous Sol−Gel Technique, ACS Omega. 3 (2018), 13227–13238, https://doi.org/ 10.1021/acsomega.8b02122.

[23] M. Boujnah, H. Ennaceri, K.Belasfar, A. El Kenz, A. Benyoussef, M. Loulidi, New Transparent Conducting Oxide based on Doped SnO_2 for Solar Cells, International Renewable and Sustainable Energy Conference (IRSEC), Marrackech, Morocco, 2016, 2–6, https://doi.org/ 10.1109/IRSEC.2016.7983960.

[24] N. Beloufa, Y. Chechab, S. Louhibi-Fasla, A. Chahed, S. Bekheira, H. Rekab-Djabri, S.

Daoud, FIRST-PRINCIPLES CALCULATIONS OF THE STRUCTURAL, ELECTRONIC AND OPTICAL PROPERTIES OF YTTRIUM-DOPED SnO_2, Annals of West University of Timisoara - Physics. 63 (2021), 40–56, https://doi.org/ 10.2478/awutp-2021-0004.

[25] Z. Y. Jiao, S. H. Ma, J. F. Yang, A comparison of the electronic and optical properties of zinc-blende, rock salt and wurtzite AlN: A DFT study, Solid State Sciences. 13 (2011), 331–336, https://doi.org/ 10.1016/j.solidstatesciences.2010.11.030

Chapter V:

Methylene blue dye photodegradation using pure and doped SnO_2 thin films

In this chapter the prepared tin dioxide thin films were used in the photocatalysis application where an overview of which was given at the end of the first chapter. The methylene blue (BM) was selected as a dye to test its degradation under the sun light for 4 hours, the change in the UV–vis spectra of BM during photodegradation over pure and Ca, Sr, and Ba-doped SnO_2 thin films at low (2 wt%) and high (8 wt%) weight ratio of dopant also were investigated, then the photocatalytic efficiency rate was calculated and plotted.

V. 1. Materials and methods

The methylene blue (MB) dye was chosen as a model of wastewater contaminants in this study. The photocatalytic degradation of MB solutions was examined using both pure and doped SnO2 thin films under solar irradiation. The photocatalyst samples were dipped in 50 ml of MB solution (5 ppm in 1 L of distilled water), before the reaction, the photocatalyst was kept in the MB solution in the dark for 30 minutes to reach adsorption equilibrium, Subsequent irradiation experiments were conducted over a four-hour period, with the MB solution stirred at a moderate speed throughout the process.

V. 2. Results and discussion

V. 2. 1. Absorbance variations and dye photodegradation of methylene blue dye under solar irradiation

First of all, the UV–vis spectra of methylene blue (BM) during photodegradation is presented in Figure V.1 it can be seen clearly that the absorbance decreases with the increasing of time for all the samples.

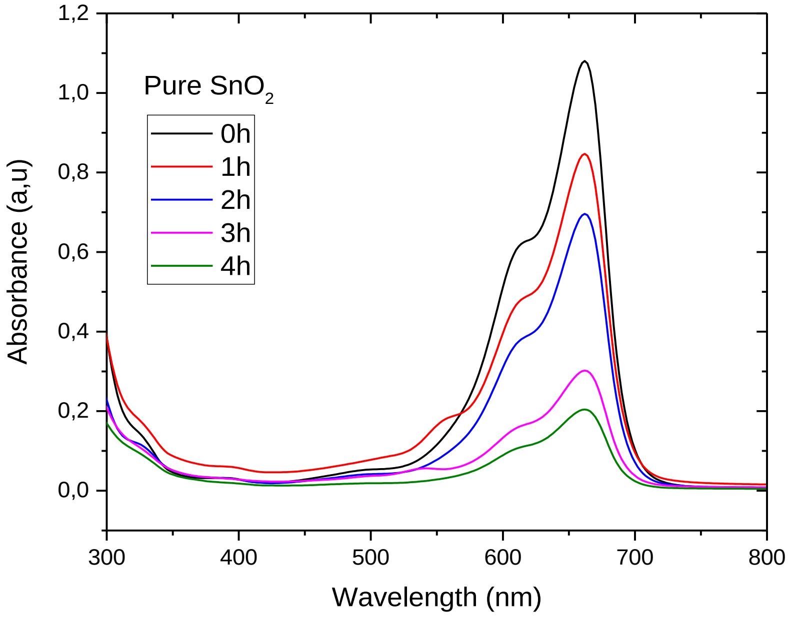

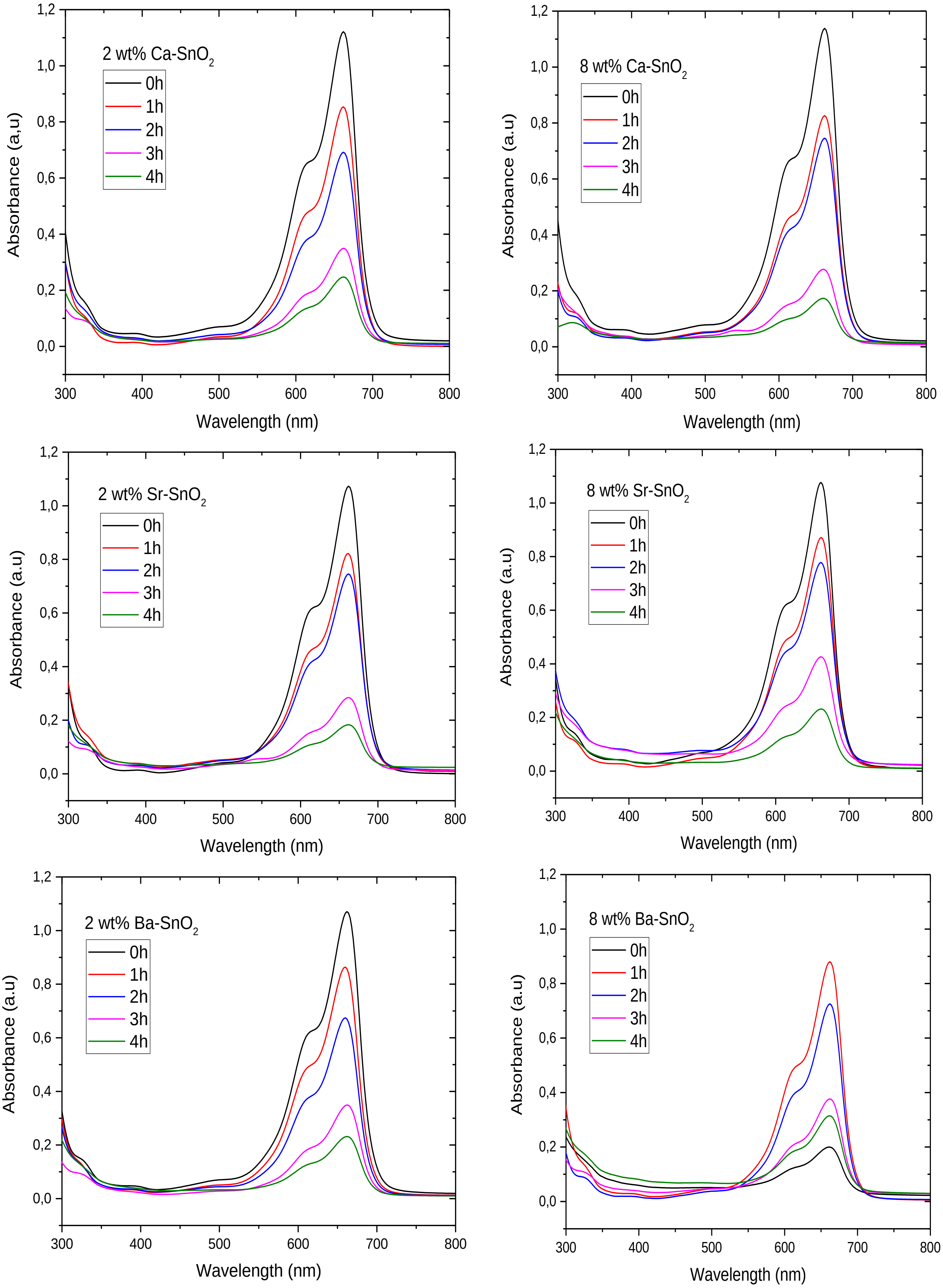

Figure V.1. Variation of UV–vis spectra of MB during photodegradation over pure and doped SnO2 thin films.

V. 2. 2. Methylene blue dye absorbance rate (photocatalytic efficiency)

The photocatalytic performance of pure and doped SnO_2 thin films was evaluated by examining the photodegradation of MB in a water-based solution under natural light. The BM absorbance rate at catalyst surfaces (SnO_2 films) was measured applying the following equation [1, 2]:

$$\%\, of\ degradation = ((A_0 - A_t)/A_0) \times 100 \qquad (V.1)$$

Or: $$\%\, of\ degradatio = ((C_0 - C_T)/C_0) \times 100 \qquad (V.2)$$

Where A_0 and A_t are the absorbance of methylene blue (λ= 661nm) at t=0 and t respectively, and C_0 and C_t are the concentrations of Methylene blue dye at t = 0 and t respectively, The two equations are related to each other through Beer-Lambert's law [3]:

$$A = \varepsilon \times L \times C \qquad (V.3)$$

Where L is length of solution the light passes through (1 cm), ε is a constant (3.76 L. mol^{-1}. Cm^{-1})

From Figure V.2 it can be seen that the just the two samples 8 wt% Ca-doped SnO_2 and 2 wt % Sr-doped SnO_2 improved the photocatalytic efficiency from (~82%) for pure SnO_2 to (~88%) and (~84%) respectively, in contrast to the rest of the samples, which results a low photocatalytic efficiency compared to pure tin dioxide film, where the lowest one is for 8 wt% Sr-doped SnO_2 film (~70%) may be because it is was poor crystallized. These results are due to changes in the value of the band gap, which is considered the most important factor affecting the photocatalytic application [4], as it is very clear in Table V.1 the lower the value of the band gap leads to an increase in the photocatalytic efficiency, this is certainly due to the fact that the narrow band gap requires the absorption of less photon energy, which helps in the quick generation of pairs represented by electrons and holes, which are considered the basis of the photocatalytic process represented by the two most important stages, which are the oxidation of hydroxide, which takes place in the valence band which is done through holes [5], and the reduction of oxygen that it takes place in the conduction which is done through electrons [6].

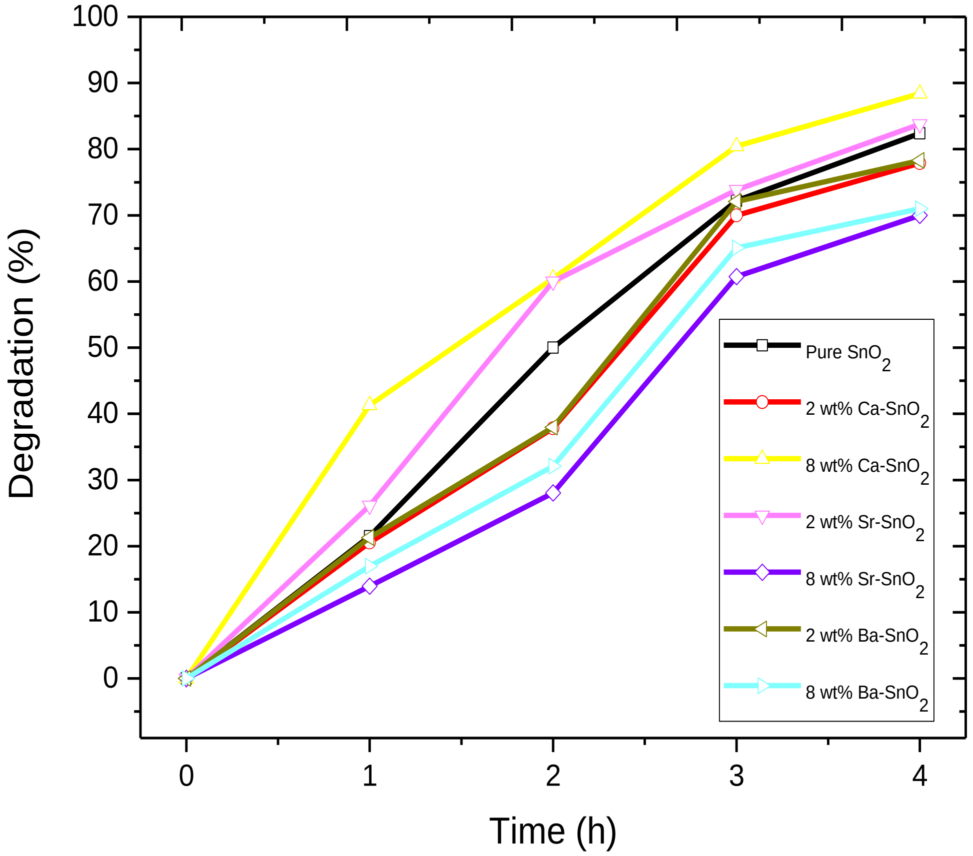

Figure V.2. Plot of photocatalytic efficiency versus the degradation time.

Table V.1: Band gap and degradation rate variations of pure and doped SnO_2 thin films.

Sample	Band gap value (eV)	Rate of degradation (%)
Pure SnO_2	3.57	82.40
2 wt% Ca-SnO_2	3.69	77.90
8 wt% Ca-SnO_2	2.86	88.40
2 wt% Sr-SnO_2	2.94	83.78
8 wt% Sr-SnO_2	/	70.02
2 wt% Ba-SnO_2	3.67	78.30
8 wt% Ba-SnO_2	3.76	71.02

References

[1] M. Althamthami, E. G. Temam, H. Ben Temam, G. G. Hasan, N. Malfi, Influence of hole-scavenger and different withdrawn speeds on photocatalytic activity of Co_3O_4 thin films under sunlight irradiation, Ceramics International. 48 (2022), 31570–31578, https://doi.org/10.1016/j.ceramint.2022.07.078.

[2] M. Khatun, P. Mitra, S. Mukherjee, Effect of band gap and particle size on photocatalytic degradation of $NiSnO_3$ nanopowder for some conventional organic dyes, Hybrid Advances. 4 (2023), 100079, https://doi.org/10.1016/j.hybadv.2023.100079.

[3] G. D. Baura, Pulse Oximeters, in: G. D. Baura (Eds), Medical Device Technologies, Elsevier Inc, 2012, pp. 237-255.

[4] E. G. Temam a, F. Djani, S. Rahmane, H. Ben Temam, B. Gasmi, Photocatalytic activity of Al/Ni doped TiO_2 films synthesized by sol-gel method: Dependence on thickness and crystal growth of photocatalysts, Surfaces and Interfaces. 31 (2022), 102077, https://doi.org/10.1016/j.surfin.2022.102077.

[5] S. H. Guana, K. F. Zhao, Q. Tong, Q.X. Rao, L. Cheng , W. Song , Q. C. Zhang, X. Li Wang, W. G. Song, A review of photocatalytic materials application on nonylphenol degradation, Environmental Challenges. 4 (2021), 100172, https://doi.org/10.1016/j.envc.2021.100172.

[6] Y. Tulebekov, Z. Orazov, B. Satybaldiyev, D. D. Snow, R. Schneider, B. Uralbekov, Reaction Steps in Heterogeneous Photocatalytic Oxidation of Toluene in Gas Phase-A Review, Molecules. 28 (2023), 6451, https://doi.org/10.3390/molecules28186451.

General conclusion and future perspectives

General conclusion

The main objective of our work is to produce high-performance thin films of a transparent conductor oxide based on pure and Ca, Sr, and Ba-doped tin dioxide, the difference in physical properties of these samples had been also investigated, then a theorical study was done using density functional theory (DFT) and compared with experimental study. Then in the final of this work a small part was added which is a photocatalytic application.

To prepare our samples we used the spray pyrolysis technique type pneumatic which is simple and low cost, more suitable for the preparation of thin film oxides, and produced homogeneous deposited films.

The different devices that it used for the characterisation was: XRD, SEM & EDS (EDX), UV-vis spectrophotometer, and four-point probe, to determine Structural, morphological, optical, and electrical properties respectively. Also, Cambridge Serial Total Energy Package (CASTEP) was used for the DFT theorical study.

In the experimental section, a comparative analysis was carried out on the prepared samples. The XRD analysis revealed that the (110) peak was notably prominent compared to the other peaks, indicating its preference as the orientation for crystal growth. Upon introducing dopant elements, the SnO_2 cell expanded, as corroborated by volume cell calculations, consistently exhibiting values higher than those of pure SnO_2 thin films. The crystallite size *(D)* exhibited a correlation with the variation in (110) peak intensity and texture coefficient *(TC)* values, aligning with the dislocation density *(δ)* and microstrain *(ε)* exhibited an inverse relationship with it. SEM analysis illustrated distinct surface morphologies, with the emergence of various shapes confirming the successful incorporation of dopant elements into the SnO_2 cell. Ca-SnO_2 exhibited superior optical properties compared to Sr-SnO_2 and Ba-SnO_2 it was observed that Ca-SnO_2 displayed high optical transmittance in the visible range, reaching approximately 90%. Notably, it was the only series where waves in the transmittance curve appeared, indicating the homogeneity of the samples, Furthermore, Ca-SnO_2 exhibited lower values of band gap in comparison to pure SnO_2. Using a 4-point probe, the electrical conductivity of the prepared samples was calculated. It was observed that, specifically for Ca-SnO_2 films, the conductivity increased with the rise in Ca content in the tin dioxide lattice. In contrast, for Sr-SnO_2 and Ba-SnO_2, conductivity was enhanced only for medium concentrations of Sr and Ba, respectively, then the conductivity decreased again.

In the theoretical section, a geometry optimization, including cut-off energy and k-points optimization for a 1x1x1 cell, was performed. The optimal values obtained were (E cut = 800 eV) and (kx= 8, ky= 8, kz= 10). A structural study and comparison were conducted between 2x2x1 and

1x1x2 supercells, representing low (4.16 at %) and high (8.33 at %) atomic ratios of M-doped SnO_2 (where M represents Ca, Sr, or Ba). The analysis revealed that the lattice of SnO_2 expanded with the increasing ionic radii of different dopant elements. This expansion was evident from the volume cell values, which also increased as the atomic ratio increased. In other words, the volume cell of the 1x1x2 supercell was higher than that of the 2x2x1 supercell for all three samples of M-doped SnO_2. According band structures curves the band gap was decreased with increasing of ionic radii. For the optical properties the absorption coefficient's intensity increased with adding dopants compared to pristine SnO_2, the absorption edge variation was in line with band gap variations.

After conducting both experimental and theoretical studies, it can be concluded that among these three dopants, calcium, which has the lowest ionic radius compared to strontium and barium, has proven to be the most effective dopant in enhancing various physical properties of tin dioxide which leads to the possibility of using it in many applications.

For the last part in this work which include the photocatalytic application it was found that the efficiency was high with using of pure SnO_2 thin film and it was enhanced with decreasing of the band gap values.

There is some of future perspectives will be studied in the near future which are indicated:

- ✓ Elaboration of pure and Ca, Sr, and Ba-doped SnO_2 by other technique which is physical vapor deposition (PVD), and the prepared samples will be used in the photocatalytic application, where the results will be compared with the experimental findings obtained in this study.
- ✓ Using of other characterization devices that were not used in this work to characterize the prepared samples.
- ✓ Using of others density functional theory (DFT) code to study the doping effect of alkaline earth elements on tin dioxide thin films and compare the results obtained with those found during the same study using the CASTEP code.

Abstract

In this work, an investigation of different physical properties was carried out on pure and Ca, Sr, and Ba-doped SnO_2 thin films. The investigation employed an experimental approach utilizing a low-cost method, namely the pneumatic spray pyrolysis technique. Additionally, a theoretical study was undertaken using density functional theory, finally a photocatalytic application was done.

The experimental study was done by preparing a starting solution with a concentration of 0.5 mol/l using $SnCl_2$, 2 H_2O as a precursor to prepare pure SnO_2 films, then $CaCl_2$, 2 H_2O; $SrCl_2$, $6H_2O$, and $BaCl_2$, 2 H_2O were added to prepare Ca, Sr, and Ba-doped SnO_2, respectively. All the samples were deposited into glass substrates heated to 450 °C, and characterized using the following four apparatuses: XRD, SEM & EDS (EDX), UV-vis spectrophotometer, and four-point probe. XRD analysis illustrated that all the films had a tetragonal rutile structure and a polycrystalline nature with a preferred growth orientation along <110> direction, SEM images showed an emergence of different chapes at the surface of the sample due to the incorporation of dopant elements into SnO_2 lattice, which was confirmed by EDS (EDX) composition analysis. The optical transmittance increased for Ca-SnO_2 and Sr-SnO_2, whereas it decreased for Ba-SnO_2 compared to pure SnO_2 films, the band gap generally decreases just for Ca-SnO_2. The electrical conductivity was increased with increasing of dopant concentrations just for Ca-SnO_2, while for Sr, and Ba-doped SnO_2, it was increased at medium concentrations then it was decreased again.

The theoretical study was done using the Cambridge Serial Total Energy Package (CASTEP) code. The study included a comparison between high (8.33 at%) and low (4.16 at%) atomic ratio concentrations of dopants. From the structural study, it was found that SnO_2 cell was expanded by adding M dopants (M = Ca, Sr, or Ba). After the comparison of band structures, it was showed that the band gap values decreased by adding dopant elements compared to pure SnO_2. For the optical properties, the absorption coefficient was calculated and showed that its intensity increased by adding dopant elements to pure SnO_2, and it is always high in the UV range.

In the last part a photodegradation of the methylene blue dye was done using pure and Ca, Sr, and Ba-doped SnO_2 thin films but just for low (2 wt%) and high (8 wt%) dopant concentration, to find that the degradation rate (efficiency) enhanced just when 8 wt% ca-doped SnO_2 and 2 wt% Sr-doped SnO_2 samples used while when the using of the other samples the efficiency deteriorated.

Keywords: SnO_2 thin films, alkali earth elements, pneumatic spray pyrolysis technique, structural and morphological properties, optical and electrical properties, DFT study, degradation rate.

Résumé

Dans ce travail, une étude de différentes propriétés physiques a été réalisée sur des couches minces de SnO_2 purs et dopés au Ca, Sr et Ba. L'enquête a utilisé une approche expérimentale utilisant une méthode peu coûteuse, à savoir la technique de pyrolyse par pulvérisation pneumatique. De plus, une étude théorique a été entreprise en utilisant la théorie fonctionnelle de la densité, et a la fin une application photocatalytique a été réalisée.

L'étude expérimentale a été réalisée en préparant une solution de départ à une concentration de 0,5 mol/l en utilisant $SnCl_2$, 2 H_2O comme précurseur pour préparer des films de SnO_2 pur, puis $CaCl_2$, 2 H_2O ; $SrCl_2$, $6H_2O$ et $BaCl_2$, 2 H_2O ont été ajoutés pour préparer du SnO_2 dopé au Ca, Sr et Ba, respectivement. Tous les échantillons ont été déposés sur des substrats de verre chauffés à 450 °C et caractérisés à l'aide des quatre appareils suivants : DRX, MEB et EDS (EDX), spectrophotomètre UV-vis et les quatre points. L'analyse DRX a montré que tous les couches avaient une structure rutile tétragonale et une nature polycristalline avec une orientation de croissance préférée dans la direction <110>. Les images MEB ont montré l'émergence de différentes formes à la surface de l'échantillon en raison de l'incorporation d'éléments dopants dans SnO_2 réseau, ce qui a été confirmé par l'analyse de la composition EDS (EDX). La transmission optique a augmenté pour le Ca-SnO_2 et le Sr-SnO_2, alors qu'elle a diminué pour le Ba-SnO_2 par rapport aux films de SnO2 pur, la bande interdite diminue généralement uniquement pour le Ca-SnO_2. La conductivité électrique a augmenté avec l'augmentation des concentrations de dopant uniquement pour le Ca-SnO_2, tandis que pour le Sr et le SnO_2 dopé au Ba, elle a augmenté à des concentrations moyennes, puis a diminué à nouveau.

L'étude théorique a été réalisée à l'aide du code Cambridge Serial Total Energy Package (CASTEP). L'étude comprenait une comparaison entre des concentrations de rapport atomique élevées (8,33 at %) et faibles (4,16 at %) de dopants. L'étude structurelle a montré que la cellule SnO_2 était développée en ajoutant des dopants M (M = Ca, Sr ou Ba). Après la comparaison des structures de bandes, il a été montré que les valeurs de bande interdite diminuaient en ajoutant des éléments dopants par rapport au SnO_2 pur. Pour les propriétés optiques, le coefficient d'absorption a été calculé et a montré que son intensité augmentait en ajoutant des éléments dopants au SnO_2 pur, et qu'il était toujours élevé dans la gamme UV.

Dans la dernière partie, une photodégradation du colorant bleu de méthylène a été réalisée en utilisant des couches minces de SnO_2 purs et dopés au Ca, Sr et Ba, mais uniquement pour une concentration de dopant faible (2 wt%) et élevée (8 wt%), pour constater que le taux de dégradation (efficacité) s'est amélioré juste lorsque des échantillons de SnO_2 dopés au ca à 8 wt% Ca-SnO_2 et à 2 wt% Sr-SnO_2 ont été utilisés, tandis que lors de l'utilisation d'autres échantillons, l'efficacité s'est détériorée.

Mots clés: couches minces de SnO_2, éléments alcalino-terreux, technique de pyrolyse par pulvérisation pneumatique, propriétés structurales et morphologiques, propriétés optiques et électriques, étude DFT, taux de dégradation.

الملخص

في هذا العمل تمت دراسة مختلف الخصائص الفيزيائية لأكسيد القصدير النقي والمطعم بالكالسيوم، السترونتيوم، والباريوم، حيث تم استخدام طريقة سهلة وغير مكلفة تعرف بطريقة الرش الهوائي. كذلك تم القيام بدراسة نظرية لنفس العينات باستخدام نظرية الكثافة الوظيفية، و في الأخير تم القيام بتطبيق التحفيز الضوئي.

بالنسبة للجزء التجريبي فقد تم تحضير محلول اولي بتركيز 0.5 مول/ لتر باستعمال مادة كلوريد القصدير الثنائي ($SnCl_2$, $2H_2O$) لتحضير الطبقات الرقيقة لثاني أكسيد القصدير النقي ثم تمت إضافة كلوريدات أخرى و هي كلوريد الكالسيوم، كلوريد السترونتيوم، و كلوريد الباريوم لتحضير شرائح القصدير المطعم بالكالسيوم، السترونتيوم، و الباريوم على التوالي ، تم ترسيب جميع العينات على مسند زجاجي 450 °C كما تم توصيفها باستخدام الأجهزة الموالية : انعراج الاشعة السينية (XRD)، مطيافية الاشعة فوق البنفسجية و المرئية(UV-vis spectrophotometer)، المجهر الالكتروني الماسح (SEM)، و تقنية الأربع مسابير(4-point probe). من خلال XRD تبين ان جميع العينات لها بنية رباعي الزوايا وأنها متعددة البلورات بالإضافة الى اتجاه تفضيلي للنمو وهو < 110 >، صور المجهر الالكتروني الماسح نمو اشكال مختلفة على سطح العينات وهذا يدل على دخول عناصر التطعيم داخل شبكة ثاني أكسيد القصدير وهذا ما تم اثباته من خلال التحليل العنصري لتشتت الاشعة السينية (EDX). النفاذية الضوئية تزايدت عموما فقط بالنسبة لعينات الكالسيوم السترونتيوم المطعم لأكسيد القصدير بينما حدث العكس بالنسبة للباريوم المطعم لأكسيد القصدير، وقيمة النطاق الممنوع تناقصت فقط بالنسبة للكالسيوم المطعم لثاني أكسيد القصدير. الناقلية الكهربائية تزيدت مع تزايد تركيز الكالسيوم بينما بالنسبة للسترونتيوم والباريوم المطعم لأكسيد القصدير فان الناقلية تزداد فقط بالنسبة لتراكيز متوسطة من السترونتيوم والباريوم بينما تتناقص من جديد عند تراكيز عالية.

بالنسبة للدراسة النظرية تمت باستخدام رمز حزمة الطاقة الإجمالية التسلسلية من كامبريدج ((CASTEP. كانت الدراسة عن طريق مقارنة بين تراكيز ذرية عالية (8.33 at %) ومنخفضة (4.16 at %) من مواد التطعيم، الدراسة البنيوية أوضحت ان خلية ثاني أكسيد القصدير تمددت بإضافة المواد المطعمة يشار لها ب M حيث (M ممكن ان تكونCa اوSr اوBa). ايضا بعد مقارنة هياكل النطاقات، تبين أن قيم فجوة النطاق انخفضت بإضافة عناصر التطعيم مقارنة بـ SnO_2 النقي. وأخيرا بالنسبة للخصائص البصرية، تم حساب معامل الامتصاص وتبين أن شدته تزداد بإضافة العناصر المطعمة إلى SnO_2 النقي، وهو دائما ذو قيمة عالية في مجال الاشعة فوق البنفسجية.

والجزء الأخير كان عبارة عن التحلل الضوئي بواسطة ضوء الشمس للصبغة المتمثلة في ازرق الميثيل حيث تم خلال هذه العملية استخدام الشرائح الرقيقة المصنوعة من ثاني أكسيد القصدير النقي و المطعم بالعناصر الثلاثة المتمثلة في الكالسيوم و السترونتيوم و الباريوم لكن فقط ذات التراكيز الوزنية المنخفضة (2 بالمئة) و العالية (8 بالمئة) من التطعيم ، حيث ان فقط

العينتان المتمثلتان في 8 بالمئة و 2 بالمئة نسبة وزنية من الكالسيوم و السترونتيوم المطعم لثاني أكسيد القصدير على التوالي هما اللذان حسنا مردود عملية التحفيز الضوئي اما باستخدام باقي العينات فالمردود تدهور.

الكلمات المفتاحية: شرائح رقيقة ل SnO_2 ، العناصر القلوية الأرضية، تقنية الرش الهوائي، الخصائص البنيوية و المورفولوجية، الخصائص الضوئية و الكهربائية، دراسة دالة الكثافة الوظيفية، معدل التحلل الضوئي.